Crystallization in systems of hard polyhedra

by

Richmond S. Newman

A dissertation submitted in partial fulfillment
of the requirements for the degree of
Doctor of Philosophy
(Chemical Engineering)
in the University of Michigan
2016

Doctoral Committee:

Professor Sharon C. Glotzer, Chair
Professor John Kieffer
Professor Michael J. Solomon
Professor Robert M. Ziff

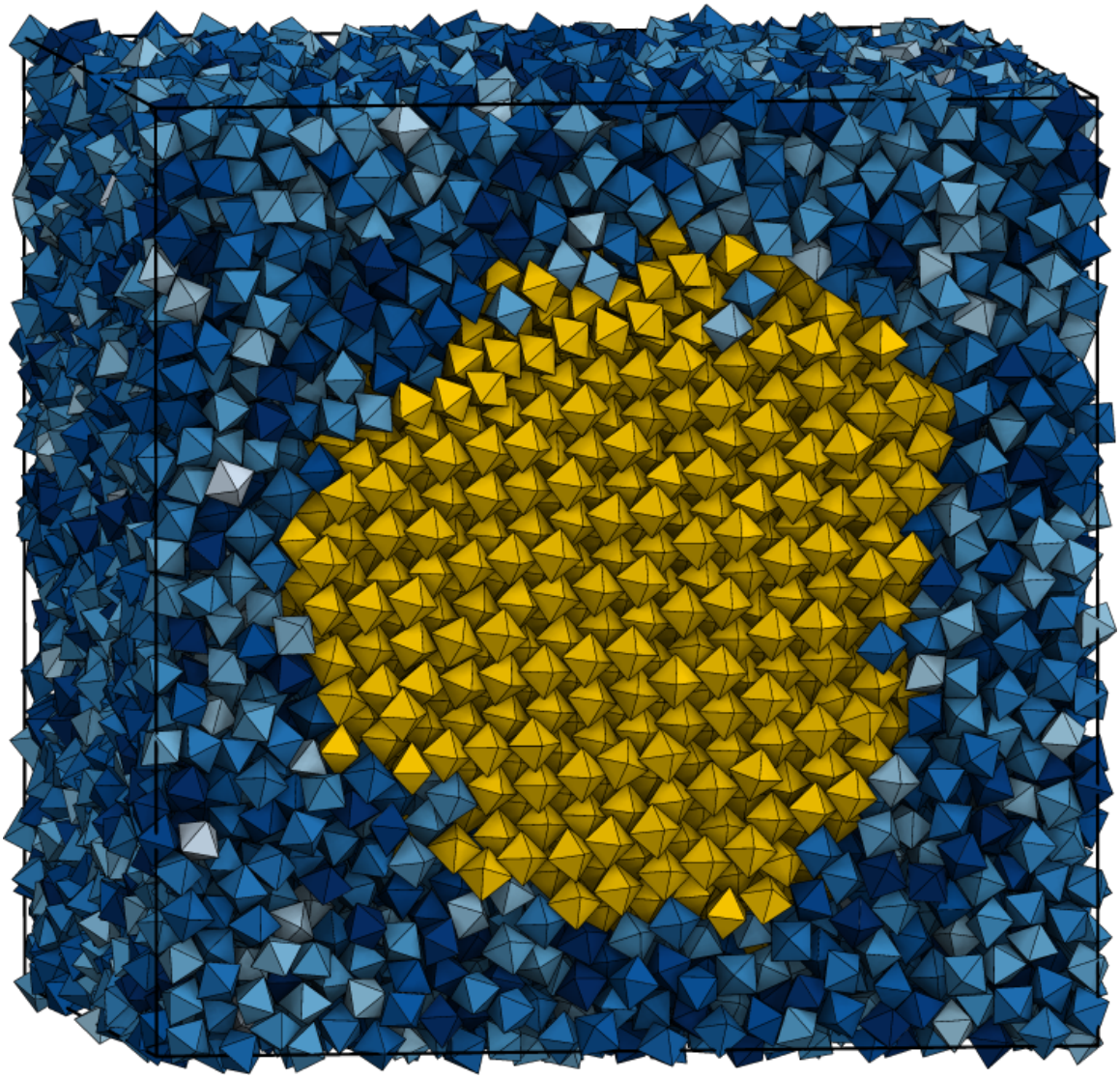

©Richmond S. Newman

2016

To my late mother, Rungtiva. You are dearly missed, and I am saddened that we could not see this through together. I may only hope to strive for a fraction of your cheerful and positive outlook on life.

Acknowledgments

I would like to first thank my advisor Sharon Glotzer for taking me as a student, and providing the research support and environment allowing me to undertake this work. The team she has constructed here is amazing and I could not have asked for a better work environment. As to particularly esteemed colleagues I have worked with, I would first like to thank Eric Jankowski, for teaching me the basics of molecular simulation and helping me get my early simulations running. I have been fortunate to have worked on two projects with Michael Engel, his patient oversight and discussions of the science helped expand my abilities to undertake scientific endeavors. I would like to thank Joshua Anderson for building the excellent simulation software for molecular dynamics HOOMD, and bringing software development practices to our research group. I will thank Josh Anderson again, and Eric Irrgang for implementing HPMC, a high performance Monte Carlo simulation code that I used extensively in this work. Greg van Anders has always been insightful to discuss any project with, as have Ryan Marson, Eric Harper, and Xiyu Du. Working and discussing science with Samanthule Nola helped us both (I hope) to better understand and study the nucleation processes in these hard particle systems. Further thanks to Julia Dshemuchadse for helping write and present science more clearly, Karen Coulter whose management keeps the lab running smoothly, and to my experimental collaborators Xingchen Ye and Jianxiao Gong who I had the pleasure to work with. To the rest of my colleagues in the Glotzer group, I know working with all of you has made me a better researcher. I apologize for not mentioning each and every one of you. And to my old friends Jacob Wolf and Stephen Barr for pushing me down the path to graduate school.

TABLE OF CONTENTS

Dedication . . . . . **ii**

Acknowledgments . . . . . **iii**

List of Figures . . . . . **vi**

Abstract . . . . . **xi**

Chapter

1 Introduction **1**

1.1 Introduction 1

2 Methods **5**

2.1 Hard Particle Models 5
2.2 Statistical Mechanics and Thermodynamics 6
2.2.1 Canonical Ensemble 6
2.3 Monte Carlo Simulation Method 8
2.4 Order Parameters 10
2.4.1 Local Bond Order Parameters 11
2.4.2 Solid-Liquid Order Parameters for Nuclei Detection 12
2.5 Umbrella Sampling 13
2.6 Thermodynamic Integration 16
2.7 Interfacial Pinning 17
2.8 Potentials of Mean Force and Torque 17

3 Self Assembly of Lithium Yttrium Fluoride Bipyramids **18**

3.1 Experimental Assemblies Synopsis 18
3.2 Bipyramid Simulation Methods 20
3.3 Bipyramid Simulation Results 22
3.4 Concluding Remarks - Bipyramids 28

4 Shape-Dependent Ordering of Gold Nanocrystals into Large-Scale Superlattices **29**

4.1 Synthesis and Assembly Experiments 29
4.2 Superlattice Quality and Crystallographic Order 31
4.3 Nucleation and Growth of Superlattices in Monte Carlo Simulation . . . 34
4.4 Factors Affecting Superlattice Quality 39

4.5 Concluding Remarks . . . 43

5 Nucleation Comparison of Rhombic Dodecahedra and Spheres . . . 45

5.1 Simulation Details . . . 46
5.2 Results . . . 47
5.3 Concluding Remarks . . . 51

6 Investigating the Role of Polyhedral Faceting on the Nucleation of Face-centered Cubic Crystals from Fluids of Hard Polyhedra . . . 54

6.1 Simulation Details . . . 56
6.2 Results . . . 56
6.3 Concluding Remarks . . . 62

7 Conclusions and Future Outlook . . . 65

7.1 Summary . . . 65
7.2 Future Outlook . . . 66

Appendices . . . 68

Bibliography . . . 70

LIST OF FIGURES

2.1 *Solid-Liquid order parameter identifying a quasicrystal.* Quasicrystalline particles are colored yellow. Fluid particles are displayed as small grey dots and only a thin slice of the dense simulation box is shown to make it easier to see the structure. Parameters were set to $l = 10$, $q_c = 5.2$, $s_c = 20$. For computing q_{lm} (equation 2.24) and solid particle clustering a radius of up to 2.1 was used to define neighboring particles. For computing $q_l(i, j)$ in equation 2.25 particles within a shell between r_{min} and $r_{max} = 3$ were used. These convoluted parameters were found by brute force training on files of known disordered and ordered states. This image was produced by Michael Engel. 14

3.1 *Selected SEM images of assemblies.* Assemblies of $LiYF_4$ nanobipyramids by our collaborators. (a) Alternating motif, (b) parallel motif, (c) rare parallel motif (d) body-centered tetragonal bulk structure from tip-truncated bipyramids. Scale bars are (a−c) 100nm, (d) 50nm. Reproduced from our work [51]. . . . 19

3.2 *Truncated bipyramids*. Images of bipyramids with aspect ratio $A = 2$, ranging from untruncated $t = 0.0$ (left) to a truncation of $t = 0.20$ (right) in intervals of $\delta t = 0.4$. 21

3.3 *Bipyramid aspect ratios*. (a) Local parallel order parameter for various aspect ratio of bipyramids. Labeled locations correspond to (b), (c), and (d). (b) Octahedra at $\rho = 0.32$ and $A = 1.0$ assembled into a triangular lattice. Particles are colored by their orientation in the xy-plane, with orientation given by the $\pm A$ vertex with a positive z-component. (c) Bipyramids at $\rho = 0.32$ and $A = 1.6$ form a parallel-aligned motif. (d) Bipyramids at $\rho = 0.32$ and $A = 2.8$. Figure from our collaboration[51]. 23

3.4 *Bipyramid Truncations*. (a) Local directional order phase diagram for the aspect ratio $A = 2$ edge truncated bipyramids illustrated in Figure 3.2. Locations labeled on this subfigure correspond to the statepoints shown in (c),(d), and (e). (b) Global axial order parameter for the same system. (c) Parallel ordered phase assembly, (d) Antiparallel ordered phase assembly, (e) Rolled-parallel ordered phase assembly. From our publication[51]. 25

3.5 *Face-attractive bipyramids*. (a) Local directional order phase diagram for the aspect ratio $A = 2$ bipyramids, with face-centered attractive patches (Details in section 3.2). Locations marked on this subfigure correspond to the simulations shown in (c) and (d). (b) Global axial order parameter for the same system. (c) Poor quality mixed parallel and antiparallel phase occurs when the interactions are weak at $\epsilon/k_bT = 1$. (d) Stronger face centered attractive patches at $\epsilon = 3/k_bT$ lead to the formation of highly ordered antiparallel phases. From our collaboration[51]. 26

3.6 *Tip-truncated bipyramids*. (a,b) SEM images of tip-truncated bipyramids forming a body-centered tetragonal structure. (c,d) Simulations of similarly-shaped hard particles readily crystallize into the same bulk structure. From our work[51]. 27

4.1 *Large-scale SEM images of superlattices using gold nanocrystals.* The nanocrystal shapes are (a) large (lRD), (b) medium (mRD), (c) small (sRD) rhombic dodecahedra, (d) octahedra, (e) cubes, and (f) spheres. The view is chosen perpendicular to the bottom of the superlattice surface, which was in contact with the glass cuvette before peeled off. The particle shape and a fast Fourier transform of the SEM image are shown as insets. As confirmed by sharp spots in the diffraction images, all superlattice films with the exception of that formed from spheres are single domains across SEM images. Figure reproduced from publication[52]. 32

4.2 *Large-scale SEM of rhombic dodecahedra.* (a) Low-magnification SEM image of a millimeter-scale sRD sample. (b-g) Six higher-magnified images taken at various points along the sample. The fast Fourier transform patterns over different regions have identical orientation suggesting the entire sample is single-crystalline. Figure reproduced from publication[52]. 33

4.3 *Minkowski lattice.* The Minkowski lattice is the densest known packing of octahedra. (a) A $4 \times 4 \times 4$ Minkowski crystal. (b-d) A single octahedron surrounded by its first coordination shell of adjacent octahedra observed under three different projections. Figure reproduced from publication[52]. 35

4.4 *SEM analysis of gold superlattices.* Analysis of nanocrystal superlattices in (a-k) real space using SEM and (l-u) reciprocal space using SAXS. (a-d) Rhombic dodecahedra form a face-centered cubic superlattice visible along different projection directions. (e-h) Octahedra are found predominantly in two crystallographically distinct superlattices: simple hexagonal (e-g) and monoclinic (e, h). Cubes, (i, j), assemble into a simple cubic lattice. (k) A macroscopic view shows a complete superlattice film. (l-p) Two-dimensional and (q-u) radially averaged SAXS images of assembly products exhibit clear diffraction spots and peaks, respectively, highlighting long-range order in superlattices of sRD (l, q), mRD (m, r), lRD (n, s), octahedra (o, t), and cubes (p, u). In (l-p), the indexed SAXS images are shown with low beam intensity on the left and with various higher beam intensities on the right to resolve additional diffraction peaks. Peaks are not indexed for the octahedron SL (o, t), because they correspond to the patterns of a superposition of two unique SL structures. Figure reproduced from publication[52]. 36

4.5 *Simulation results.* Crystallization of nanocrystal superlattices in Monte Carlo simulations of hard particles. (a) Density range where homogenous nucleation and growth occurs for each particle shape using isochoric simulations starting from configurations rapidly compressed to a selected packing density. Rectangles in a density vs. shape grid are colored by the calculated system-average local order for rhombic dodecahedra, octahedra, cubes, and spheres. Low values (blue) indicate disordered local structure (fluid), while high values (red) indicate crystalline order. Empty cells demarcate the regions beyond random close packing. Each data point represents the average of ten runs over 50 million Monte Carlo cycles. (b) Early, middle and late stage growth of homogeneously nucleating superlattices for rhombic dodecahedra, octahedra, cubes, and spheres. Densities are selected to represent a typical Monte Carlo trajectory for the particular shape and crystallization may result from several nuclei. (c) Time to nucleate, as measured by the number of Monte Carlo cycles for the system to reach 20% crystallinity. (d) Time to grow, as measured by the time required to advance from 20% to 80% crystallinity. (e) Number of ordered layers equilibrated near hard boundaries at densities lower than where homogeneous nucleation occurs. Figure reproduced from publication[52]. . . 38

4.6 *Heterogeneous growth.* Monte Carlo simulations with impenetrable hard boundaries at the top and bottom (in the image) of the simulation box to study heterogeneous nucleation. The sides are connected via periodic boundary conditions. Simulations are conducted for systems of (a) RDs, (b) octahedra, (c) cubes, and (d) spheres. The crystal structure of the SLs observed near the wall is identical to the crystal structure observed in nuclei forming via homogenous nucleation with the exception of octahedra, which prefer the monoclinic SL near the wall. The packing fractions used in the simulations are $\phi = 0.56$ for RDs, $\phi = 0.56$ for octahedra, $\phi = 0.55$ for cubes, and $\phi = 0.54$ for spheres. Figure reproduced from publication[52]. 40

4.7 *Structural details and factors affecting quality of nanocrystal superlattices.* (a-c) Analysis of rhombic dodecahedra superlattices. In simulation we find a rotator (plastic) face-centered cubic phase at low density (a), and quenched in rotational disorder is also observed in SEM images (b, c). (d-j) Analysis of octahedron superlattices. A simulation that nucleated the Minkowski superlattice(d). In experiment we observe monoclinic superlattice (e, f), Minkowski superlattice (g), and simple hexagonal superlattice (s.h. parallel), in rare occurrences (h), alternation of octahedron orientations in layers of simple hexagonal superlattice is violated, as visible in the first and second layers of (h). Single layer of octahedron superlattice near walls in hexagonal packing in simulation (i) and experiment (j). Packing density and contact fraction of different lattices are compared in (k). (l, m) Analysis of cube superlattices. Simulation (l) and experiment (m) both show streaks in the fast Fourier transform images. (n) Monte Carlo simulations of hard spheres, typically resulting in stacking faults. Layers are colored by ABC stacking sequence (A = white; B = light blue; C = blue).Figure reproduced from publication[52]. 41

4.8 *Evidence for a rotator phase in rhombic dodecahedra.* Additional SEM images of mRD SLs from other directions aside from the bottom of glass cuvette, on which they were grown. (a) and (b) lateral views, (c) surface exposed by breaking the SL, (d) evidence for a rotator phase in mRD SLs. Typical example defects are highlighted in colors: 4-fold vertex (blue), face (yellow), edge up (purple), and improper $\frac{\pi}{6}$ rotation of a 3-fold vertex (green). Figure reproduced from publication[52]. 42

5.1 *Equations of state.* (a) Fluid and solid equations of state and (b), the chemical potential plotted over pressure. Phase coexistence occurs where the curves intersect the dotted black line. The intersection of the dashed horizontal line at $|\Delta\mu| = 0$ with the data for each shape illustrates the coexistence pressures of fluid and solid phases. The truncation point of the curves at the high-pressure end corresponds approximately to the point at which crystallization can occur spontaneously. From our publication[65]. 47

5.2 *Cluster statistics and free energies.* (a) Cluster size distributions, (b and c) free energy barriers from umbrella sampling, and (d) free energy maxima plotted against the chemical potential from interfacial pinning of hard rhombic dodecahedra and spheres, (e) directly measured nucleation rates. For plots of the free energy barriers, graphs of different colors represent free energy curves at different pressures (exact values are given by horizontal lines and tick labels on the color bars). Adapted from our manuscript[65]. 49

5.3 *Potentials of mean force and torque.* For (a) – (b) spheres and (c) – (h) rhombic dodecahedra, for fluid ((a), (c), (e), and (g)) and crystalline systems ((b), (d), (f), and (h)). All maps use the same coloring scheme; energies are shifted so that the deepest minimum corresponds to $\beta F = 0$. The top and middle figures represent cuts through the particle centers (in the case of the rhombic dodecahedron: perpendicular to the 4-fold and 3-fold symmetry axes, respectively). The bottom figures show the PMFTs for a fluid and crystal of rhombic dodecahedra, intersecting with a thin hemisphere corresponding to the first neighbor shell. Additionally, transparent isosurfaces are shown at an energy of $\beta F = 0.5$. The insets depicting the particle illustrate the orientation of the respective set of PMFTs. From our publication[65]. 52

6.1 *Studied Polyhedra*. Rhombic dodecahedron to rhombicuboctahedron shape family. From our publication[71]. 55

6.2 *Shape family equations of state*. (a) Equations of state for the six polyhedra and spheres. Particles and curves are colored correspondingly. The left set of curves correspond to the less dense metastable fluids, and the right set of curves to the face-centered cubic crystals. (b) Equations of state expressed as volume per particle available to the system. From our publication[71]. 57

6.3 *Chemical potentials*. Computed chemical potentials $\Delta\mu$ *vs.* pressure P resulting from integrating the equations of state for each polyhedra. Figure reproduced from publication[71]. 58

6.4 *Free energy barriers*. Umbrella-sampled free energy barriers to nucleation for the polyhedra family. From our publication[71]. 59

6.5 *Free Energy Penalties to Nucleation*. Free energy barrier maxima from the umbrella-sampled NPT simulations plotted against the driving force (chemical potential) for different polyhedra. From our publication[71]. 61

6.6 *Critical nuclei*. (a) Free energy maxima plotted against critical nucleus size. (b) Critical nucleus size *vs.* crystallization driving force. From our publication[71]. 62

6.7 *Potentials of mean force and torque*. (a) Family of polyhedra. (b,c) Cross sections through the four-fold axis are shown for the (b) fluid and (c) solid phases. (d,e) Three-dimensional views of the PMFT intersecting a thin hemisphere in the first coordination shell, with isocontours drawn at $\beta F = 0.4$ from the deepest minima for the (d) fluid and (e) solid phases. From our publication[71]. 63

ABSTRACT

Crystallization in systems of hard polyhedra

by

Richmond S. Newman

Chair: Sharon C. Glotzer

Hard particle Monte Carlo computer simulations can be used to study both the equilibrium crystal phases of polyhedra and the crystallization pathways in a simplified model system. We present simulations of elongated $LiYF_4$ square bipyramids, explain the assembly behavior of gold rhombic dodecahedra, cubes, and octahedra, and investigate in detail the thermodynamics and driving forces for nucleation of a continuous family of polyhedra. In the work on bipyramids we found that either truncation or particle interactions are required to form a novel antiparallel phase. In the study of gold nanopolyhedra we found that the nucleation behavior and structural quality for each polyhedra is strongly dependent on novel properties arising from each shape. Following this, we delved into the nucleation process studying the thermodynamics and free energy barriers to crystallization in rhombic dodecahedra and spheres, and found that the polyhedral faceting stabilized the nucleation pathway. We then demonstrated the importance of this faceting by studying truncations of the rhombic dodecahedra and found that the truncation undermined the local symmetry of the fluid and increased the driving forces required for nucleation. This work demonstrates the role of simulation in understanding experimental systems and how perturbations to shape can alter the pathway to crystallization.

CHAPTER 1

Introduction

1.1 Introduction

We are entering an era where more and more monodisperse colloidal building blocks can be synthesized and used for self-assembly. This opens up the search space for creating crystal structures at new length scales that were inaccessable to atomic systems. In addition, novel features arise when noble-metal building blocks are crystallized into ordered superlattices, such as the unusually strong surface plasmon resonance[1, 2, 3, 4] and collective oscillations of free electrons[5, 6, 7, 8, 9] that arise when these nanocrystal form superlattices[5, 9, 10]. Many of these building blocks are shaped like nanoscale polyhedra arising from crystalline faceting and minimization of surface free energies. The promise of length-scale control of crystals beyond the atomic is the subject of intense research interest[5, 11, 12, 13]. Furthermore, the size and shape of these nanopolyhedra can be controlled by using the surface-ligand interactions and other synthesis conditions, allowing for large numbers of different shapes to be synthesized, such as silver nanocubes to nanooctahedra[5], which have been successfully used for self-assembly[14] into superlattices, or the etching of vertices of gold rhombic dodecahedra into rhombicuboctahedra[15].

A first-order approximation of these polyhedral particles is the hard-particle model, which models the polyhedral excluded volume as non-overlapping regions. Hard-particle models have been in use in simulations since Rosenbluth and Metropolis in 1953[16] in a study of disks, to show a first order phase transition in hard spheres in 1957[17, 18], and continues to be used today. The hard particle model describes the excluded volume interactions of particles and allows for the study of the entropic effects of packing. In 2012, Damasceno[19] studied the equilibrium self-assembled structures of 145 different convex hard polyhedra and found that 101 crystallized given sufficient density, and the remaining 44 jammed before reaching an ordered packing. While many of the building blocks formed simple face- and body-centered cubic lattices, it was found that many shapes

formed crystals of surprising complexity, such as β-Mn, A15, σ, as well as the previously studied tetrahedron quasicrystal[20, 21] despite consisting of a single-component. Damasceno also found that the coordination number in the fluid, the number of local neighbors to each polyhedra, was a significant predictor of the crystalline solid, as was the isoperimetric quotient, the ratio of the volume of a polyhedron divided by the volume of a sphere, considered at equal surface area of each('isoperimetric'). Further simulations of anisotropic polyhedra found that facets have an entropic tendency to line up face-to-face to maximize excluded volume[22, 23], but this does not explain all structures, such as the self-assembly of octahedra into the Minkowski lattice[14], where particles in the crystal are not aligned face-to-face. In these theoretical investigations of hard particles, the driving force to assemble is free energy, which reduces to only entropy when there are no explicit interactions. In the literature, hard models and simulations[14, 19, 24] have been used successfully to explain the equilibrium behavior of experimentally self-assembled structures, including those of spheres, cubes, cuboctahedra, and octahedra[14, 6, 5, 25].

Simulations are continuing to guide the understanding of experimental self-assemblies of new nanopolyhedra, which we discuss in detail in two case studies of nanopolyhedra in chapters 3 and 4. Much is still unknown, however, about how crystals form in these polyhedral systems. In experiments, it is difficult to probe the time-evolution of a system. Zhang[25] used synchrotron-based *in-situ* grazing-incidence small-angle X-ray scattering (GISAXS) to study nanooctahedra in droplets. Their GISAXS results suggested a reversible phase transition as a function of solvent concentration, as well as reversible changes of the lattice constant when growing or shrinking the droplets, showing that density was a reversible and controllable parameter of their system. Unfortunately, the nucleation event itself was not readily observable despite the reversibility.

In the early 1990s, Auer and Frenkel pioneered methods for studying crystallization in hard spheres, developing methods that can calculate free energies of clusters in the fluid[26, 27, 28]. One advantage that comes into play in simulation is that we can probe directly the statistical mechanics of a model system. Unlike in experiments, exact measurements can be made of density, volume, pressure, interaction potential, and other properties of interest. Using umbrella sampling Auer managed to calculate free energy barriers to nucleation as a function of nuclei size for hard spheres using Monte Carlo simulations, and made comparisons to classical nucleation theory suggesting that this model held. Classical nucleation theory models the free energy for a crystalline nucleus where supersaturated solutions are driven to crystallize by a favorable chemical potential $\Delta\mu$, and resisted by an

interfacial energy term γ. For a spherical nucleus of radius R, the free energy is given by

$$\Delta G = \frac{4}{3}\pi R^3 \rho \Delta\mu + 4\pi R^2 \gamma. \tag{1.1}$$

A critical nucleus is defined to be a nucleus with 50% probability to crystallize, which occurs approximately when the free energy of a cluster of N particles $\beta G(N)$ is maximal. They also used estimates of cluster size fluctuations and attachment rates in conjunction with these free energies and estimates of diffusion to try to compute nucleation rates. Their results were found to have significant disparities between experimental and simulated results for nucleation rates: namely, at low supersaturations experimental systems appeared to nucleate many orders of magnitude faster. Both hard spheres, and believed to be hard sphere colloids (in the sense that the particles are as weakly interacting as possible) form cubic-close packed structures with many hexagonally close-packed stacking faults. A great difficulty in these comparisons lies in the fact that nucleation rates were shown by Auer[27] to be heavily dependent on density, with fluids at a packing fraction of $\phi = 0.521$ having critical nuclei at $\beta G = 42$, and at $\phi = 0.534$ barriers of only $\beta G = 18$. Potential other sources of error are matching the dense phase diffusion coefficients to provide a timescale for the Monte Carlo simulations, and the difficulty of measuring exact particle packing fractions in experiments as well as the potential for particles to have a 'soft' interaction due to surface charging, particularly for particles on the size scale suitable for positional tracking via confocal microscopy, of at least 1μm[29].

Further research on hard spheres investigated effects of polydispersity δ, or the Gaussian length-scale distribution of particles, which was found to significantly reduce nucleation for polydispersity $\delta > 5\%$[28]. They found that polydispersity causes the interfacial energy to rise with supersaturation, so once polydispersity reached $\delta = 10\%$ further increases to the driving force $\Delta\mu$ stopped reducing the nucleation barriers described by nucleation theory in equation 1.1. This suggests that polydispersity was not the source of discrepancy in nucleation rates between simulations and experiments as it further hinders nucleation.

Recently, advances in computational resources have expanded sufficiently to allow for similar studies of nucleation to be carried out on hard polyhedra, which are much more expensive to simulate due to the computational costs of checking whether configurations overlap.

Work on polyhedral polydispersity by Agarwal[30] found similar results to the hard sphere literature, but for a select few polyhedra. They found that two space filling polyhedra, cubes and truncated octahedra, respectively, were more tolerant to polydispersity

than cuboctahedra or octahedra before failing to self-assemble. Generally the ranges of polydispersity in simulation are consistent with what is known to work in experiments. Moreover, recently first investigations of the nucleation behavior of polyhedra have been undertaken by Thapar[31], who suggests that local polyhedra orientations are important for self-assembly, and that orientational order 'fosters the growth of orientationally disordered nuclei'. I will elaborate on these ideas further in chapter 5, where I discuss the crystallization (including free energy barriers) of rhombic dodecahedra and spheres into face-centered cubic crystals in detail to better understand these two common shapes and their self-assembly. Chapter 6 expands on this further, computing nucleation barriers and driving forces for a continuous change from a rhombic dodecahedron to a rhombicuboctahedron for a family of face-centered cubic forming polyhedra to isolate the impact of faceting in a controlled manner instead of studying disparate shapes.

CHAPTER 2

Methods

2.1 Hard Particle Models

When we discuss hard particles, we mean particles that cannot overlap in the slightest. When used as a model of colloid systems, this can be thought of accounting for the excluded volume and helps us understand the role of entropy in the system as it possesses no enthalpic contributions. For hard spheres of diameter σ this leads to pairwise potential energies between particles i and j of the form

$$U(i,j) = \begin{cases} 0 & |r_{ij}| < \sigma \\ \infty & |r_{ij}| \geq \sigma \end{cases}, \tag{2.1}$$

where r_{ij} is the distance vector from i to j. For simulations of hard polyhedra, a similar rule holds where the energy is either 0 or ∞ based on whether or not the polyhedra overlap. Overlap checks for hard particle simulations to evaluate this pair potential are based on the Gilbert-Johnson-Keerthi distance algorithm [32, 33]. This algorithm searches for overlaps between pairs of polyhedra A and B by considering the set difference of all points within them

$$A - B = \{a - b | a \in A, b \in B\}. \tag{2.2}$$

The algorithm defines a simplex consisting of vertices of the convex polyhedron $A - B$ and iteratively updates it, swapping vertices, in a search towards the origin. If the origin is found, it means $a - b = 0$ existed for some $a \in A$ and $b \in B$, so that the two polyhedra overlap. If the algorithm converges without finding the origin, then the sets of space defining A and B are disjoint.

2.2 Statistical Mechanics and Thermodynamics

A brief primer on statistical mechanics is given here as it is necessary to understand the Monto Carlo simulation method, as well as useful for understanding the umbrella sampling, interfacial pinning, and thermodynamic integration methods.

2.2.1 Canonical Ensemble

A statistical mechanical ensemble for a given system is defined to be the set of all possible states that the system can possess. Different ensembles can be defined for different thermodynamic systems, but as we wish to describe systems of colloidal particles, let us first consider a system with a fixed number of particles N, volume V, in contact with a heat bath of temperature T. This ensemble is called the canonical ensemble, and referred to as the NVT ensemble. Particles are allowed to possess continuous positions $\mathbf{r}$ and momenta $\mathbf{p}$. The particles may have some interactions, which are included in the Hamiltonian of the system $\mathcal{H}$.

These statistical mechanical ensembles are described by the partition function–also known as the configurational integral–which as the later name suggests is the integral over all possible microstates (configurations). For the ensemble described in d dimensions and isotropic particles, the partition function is

$$Z_{NVT} = \frac{1}{N!}\frac{1}{h^{dN}}\int\int d\mathbf{p}^N d\mathbf{r}^N \exp\left[-\frac{\mathcal{H}(\mathbf{p}^N,\mathbf{r}^N)}{k_B T}\right]. \tag{2.3}$$

This is simplified by inserting the Hamiltonian and separating the integrals describing kinetic and potential energy

$$Z_{NVT} = \frac{1}{N!}\frac{1}{h^{dN}}\int d\mathbf{p}^N \exp\left[-\frac{|\mathbf{p}_i|^2}{2mk_B T}\right]\int d\mathbf{r}^N \exp\left[-\frac{\mathcal{U}(\mathbf{r}^N)}{k_B T}\right] \tag{2.4}$$

and continuing on, integrating over the particle momenta,

$$Z_{NVT} = \frac{1}{N!\Lambda^{dN}}\int d\mathbf{r}^N \exp\left[-\frac{\mathcal{U}(\mathbf{r}^N)}{k_B T}\right], \tag{2.5}$$

where $\Lambda = \sqrt{h^2/(2\pi m k_b T)}$. The potential energy of the system $\mathcal{U}$ usually arises from a pairwise potential energy U between particles

$$\mathcal{U} = \sum_{i=1}^{N}\sum_{j=1}^{N} U(i,j)(1-\delta_{ij}), \tag{2.6}$$

for all particles i and j. This integral for many-body systems is generally nontrivial to compute analytically. The exception is the ideal gas, where the integral over each particle position of $\mathcal{U} = 0$ gives V^N. The Monte Carlo method, described later, is an approach for sampling this integral numerically. Full knowledge of the partition function gives enormous information about the thermodynamics of the system. It can be shown that the log of the partition function gives the Helmholtz free energy

$$F = -k_b T \ln Z \tag{2.7}$$

or equivalently,

$$Z = e^{-F/(k_b T)} \tag{2.8}$$

Other thermodynamic properties can be derived from the Helmholtz energy using the fundamental relation

$$dF = -SdT + PdV - \mu dN. \tag{2.9}$$

Rearranging yields expressions for entropy, pressure and chemical potential.

$$P = -\left(\frac{\partial F}{\partial V}\right)_{T,N} \tag{2.10}$$

$$S = -\left(\frac{\partial F}{\partial T}\right)_{V,N} \tag{2.11}$$

$$\mu = \left(\frac{\partial F}{\partial N}\right)_{T,V} \tag{2.12}$$

Needless to say, it is desirable to know the partition function because it describes the thermodynamics of the system, but, unfortunately it is challenging to compute the integrals over $\mathbf{r}^N$.

Another important feature of the ensemble is that the probability of a given microstate occuring follows the Boltzmann distribution, with the probablity $\Pr$ of a particular configuration depending only on the potential energy U associated with that microstate r_i^N, that is

$$\Pr(r_i^N) = \frac{1}{Z} e^{-\mathcal{U}(r_i^N)/(k_b T)} \tag{2.13}$$

An important consequence of this is that ensemble averages of a thermodynamic observable A can be computed by a weighted integral via these probabilities,

$$\langle A \rangle = \frac{\frac{1}{N!\Lambda^{dN}} \int d\mathbf{r}^N A(\mathbf{r}^N) \exp\left[-\frac{\mathcal{U}(\mathbf{r}^N)}{k_B T}\right]}{Z_{NVT}}. \tag{2.14}$$

$$\langle A \rangle = \frac{\int d\mathbf{r}^N A(\mathbf{r}^N) \exp\left[-\frac{\mathcal{U}(\mathbf{r}^N)}{k_B T}\right]}{\int d\mathbf{r}^N \exp\left[-\frac{\mathcal{U}(\mathbf{r}^N)}{k_B T}\right]} \tag{2.15}$$

Similar results for ensemble averaging can be written for other ensembles. For instance, in the isothermal-isobaric (NPT) ensemble, the volume is allowed to fluctuate. This leads to an analogous result that integrates over the configuration of the particles within the system as before, but with an additional integral over different possible system volumes and a PV work term:

$$\langle A \rangle_{NPT} = \frac{\int dV \int d\mathbf{r}^N A(\mathbf{r}^N) \exp\left[-\frac{\mathcal{U}(\mathbf{r}^N)}{k_B T}\right] \exp\left[-\frac{PV}{k_B T}\right]}{\int dV \int d\mathbf{r}^N \exp\left[-\frac{\mathcal{U}(\mathbf{r}^N)}{k_B T}\right] \exp\left[-\frac{PV}{k_B T}\right]}. \tag{2.16}$$

In section 2.3 we will discuss how to approximate equations 2.15 and 2.16 using Monte Carlo simulations. For more details on classical statistical mechanics in relation to simulations we refer to the excellent books on molecular simulation by Frenkel and Smit[34] or Sethna[35].

2.3 Monte Carlo Simulation Method

The Monte Carlo method is a technique that allows for simulations to effectively sample statistical mechanical ensembles. In the discussion of statistical mechanics we saw that solving the configurational integrals and for the partition function would yield almost all information about the system. As it turns out, solving the configurational integrals are beyond Herculean, so we must look for a new approach if we wish to study systems of more than a few particles in the canonical or isothermal-isobaric enembles. Metropolis and Rosenbluth[16] provided an approach to sample these integrals in their study of hard disks. They proposed a numerical solution to the dN dimensional integrals by sampling configurations with a probability of $\exp(-\mathcal{U}/k_b T)$ and weighting them evenly, rather than trying to sample random configurations within phase space $\mathbf{r}^n$, and weighting them by $\exp(-\mathcal{U}/k_b T)$ as dictated by equation 2.13. The difference allows avoiding excessive sampling of high-energy states that contribute little to the partition function.

For the case of hard particles, any system possessing any overlaps has $\mathcal{U} = \infty$ corresponding to probability 0. For moderately dense systems that crystallize in $d = 3$, we usually need thousands of particles to avoid finite size effects at a packing fraction $\phi \approx 0.5$. Random states at these densities almost surely overlap, such that importance sampling towards low-energy states (for hard particles, those not overlapping) is required to efficiently

or usefully sample configurational phase space.

This sampling of microstates weighted by $\exp(-U/k_bT)$, the same probability as those in the canonical ensemble (equation 2.13), means that we can calculate statistical mechanically correct ensemble averages of thermodynamic observables as simply

$$\langle A \rangle = \frac{1}{M} \sum_{i=1}^{M} A(r_i^N), \tag{2.17}$$

where the sum carries over measurements i of the system, and $A(r_i^N)$ is the value of the observable A at a given configuration of the system r_i^N. This lets us properly sample observables once the simulations equilibrate, without analytically solving the partition functions and integrals in equations 2.15 and 2.16.

The generation of new microstates in this importance sampling does require certain conditions to be met to accurately represent statistical mechanical ensembles. This is done by generating a particular Markovian random walk through configurational space. The most common update moves to this random walk are a perturbation of the particle positions (or orientations) through phase space, each of which is called a trial move. The acceptance probability of each trial $\Pr_{accept}$ is based upon the change in energy

$$\Pr_{accept} = \min\{1, e^{-(\mathcal{U}_{new} - \mathcal{U}_{old})}\}. \tag{2.18}$$

The simulations move forward by iteratively running trial moves. For a system of N particles, we consider N positional moves to constitute one Monte Carlo cycle, and also include N orientational moves if anisotropic and one volumetric move if in the NPT ensemble. In the Monte Carlo scheme for the simulations in this thesis, local positional moves on random particles are chosen on a uniform random distribution within a small ball of fixed size, and similarly, rotational moves on anisotropic particles are confined to a local perturbation of the quaternion representing orientations of particles. Other Monte Carlo moves can be defined as well to speed equilibration of systems, such as particle type exchanging moves in binary systems[36], but are not used in this work.

The changes in each trial also are chosen to obey detailed balance, a sufficient but not necessary constraint that the transition probabilities between given states be equal. Detailed balance is simply that the probability flux between any pair of microstates i and j are equal; that is, given the probability of being in a microstate π_i, and transition probabilities of i to j denoted as q_{ij}, detailed balance is given by

$$\pi_i q_{ij} = \pi_j q_{ji}. \tag{2.19}$$

In fact, the acceptance criterion described in 2.18 is chosen to satisfy this constraint given that the microstate probabilities π_i are distributed according to 2.13. Substituting both equations yields detailed balance.

The sufficient and necessary condition for the simulation moves to converge to sampling the canonical ensemble is that they are chosen so they follow global balance[37]. This requirement constrains the net flux in and out of any given state,

$$\pi_i \sum_{j \neq i} q_{ij} = \sum_{j \neq i} \pi_j q_{ji}. \tag{2.20}$$

The pairwise detailed balance assures global balance, as it implies that each pair of i and j possible in the global balance summation are equal, such that the sums must be equal. Satisfying the global balance constraint guarantees that the simulation should eventually converge to equilibrium given sufficient time and allow for sampling of observables.

The description of a Monte Carlo simulation and its requirements here was given for the NVT ensemble, but simulations in other ensembles are performed as well. Simulations in the NPT ensemble require a box update move and acceptance criterion over volumes that maintain detailed balance. Further discussion of implementations of such are available elsewhere[33, 34], and when done correctly allow equilibrium measurements of a simulation to calculate thermodynamic averages using equation 2.17.

In this work we used a Monte Carlo simulator implemented by Michael Engel, as well as HPMC[33], a parallelized Monte Carlo simulation code written as an extension to HOOMD[38], a high performance molecular dynamics simulation package.

2.4 Order Parameters

Order parameters are useful for quantifying the results from computer simulations. Datasets can be generated for as many state-points as computational resources allow, and it is useful to be able to characterize properties of the system using automated, analytic methods rather than doing structural identification by hand. Moreover, events such as finding small nuclei in a bath of fluid would be impossible without techniques to robustly identify them. For such studies, each simulation state would represent a haystack that may not even contain a needle. Discussed here are order parameters that have broad or common use. Specific order parameters developed for use on specific papers are discussed in the appropriate chapters describing the work.

2.4.1 Local Bond Order Parameters

Characterizing particle local structures is often done by considering their local bond environment, where the bonds are constructed between neighboring particles. Several choices exist for defining neighbors. The most common is to define neighbors as those lying within a sufficiently close, fixed distance, that is generally taken to be within the first peak of the radial distribution function, oft called the pairwise correlation function $g(r)$. We colloquially call this cutoff radius r_{cut}. A second is to use a fixed number of nearest neighbors, which is a good choice for crystals whose local structure is known. An example of this is hard disks having six neighbors when placed on a triangular lattice. A third approach is to weight neighbors by their contact area in a Voronoi tesselation[39]. The latter has the useful property of continuity with respect to small perturbations in particle positions, making the methods more numerically stable and continuous. The latter approaches are often unnecessary, however, and are significantly more computationally expensive[40]. In this work we generally used a fixed distance cutoff to classify neighbors r_{cut} that is common in the literature and which functions well for structures with at least 10 neighbors. For structures such as diamond with a coordination number of 4, the use of the latter two methods should be considered.

These local environments are frequently characterized using spherical harmonics. Spherical harmonics Y_{lm} are a set of functions that arise as the angular solution to Laplace's equation, $\nabla^2\varphi = 0$, in spherical coordinates. This set of functions is a natural choice for representing orientational information as they form a complete orthonormal basis of functions on the unit sphere. This means that there exists a linear combination of spherical harmonics equal to any square-integrable function $f(\theta, \phi)$. This is analogous to the Fourier series which uses sums of sines and cosines as a basis to represent square integrable functions on finite intervals in $\mathbb{R}$.

The spherical harmonics are defined as

$$Y_{lm}(\theta,\phi) = \sqrt{\frac{2l+1}{4\pi}\frac{(l-m)!}{(l+m)!}}P_l^m(\cos\theta)e^{im\phi}, \tag{2.21}$$

where

$$P_l^m(x) = \frac{(-1)^m}{2^l l!}(1-x^2)^{m/2}\frac{d^{l+m}}{dx^{l+m}}(x^2-1)^l. \tag{2.22}$$

Steinhardt defined locally invariant order parameters[41] based on these spherical harmonics; these have been implemented in our group's analysis package, Freud[42]. Rotationally invariant order parameters are desirable as they yield the same value when analyzing systems with different crystal orientations. I implemented his local Q_l order parameter,

defined for each particle i in a system as

$$Q_l(i) = \left(\frac{4\pi}{2l+1} \sum_{m=-l}^{l} |Q_{lm}|^2 \right)^{\frac{1}{2}}, \tag{2.23}$$

where

$$q_{lm}(i) = \sum_{j=1}^{N_n(i)} Y_{lm}(\theta_{ij}, \phi_{ij}). \tag{2.24}$$

$N_n(i)$ is the number of neighboring particles j of particle i and the spherical harmonic Y_{lm} is computed over orientations θ and ϕ_{ij} from the interparticle distance vector $r_{ij} = r_j - r_i$. These order parameters are useful for quantifying different fluids and crystals when averaged over the system, and are also useful metrics of local ordering or fluctuations in the system.

2.4.2 Solid-Liquid Order Parameters for Nuclei Detection

Robust order parameters exist for separating crystalline regions from disordered fluid for a variety of crystal structures. The order parameter by ten Wolde[43] robustly solves this task. I have written an implementation for this into our research group analysis code, Freud, which is to be open sourced in the near future[42].

In the first step, we compute the local bond-orientational order, given above in equation 2.24. The bond orientational order measures the local environment of each particle. To look for crystalline regions a scalar product between all pairs of local environments is used as a measure of correlation given as

$$q_l(i,j) = \sum_{m=-l}^{l} \text{Re}(q_{lm}(i) q^*_{lm}(j)). \tag{2.25}$$

It can be expected that the local environments of particles in a crystal have more coherent products than the disordered fluid because the crystal has long-range positional order. This means that particles that are in the crystals should have larger real components after the product in equation 2.25. In equation 2.25 we do not normalize the the sum as the magnitude is a reflection of the quality of the match and indicative to some extent of the number of neighbors. This matches the convention used by Auer[26, 27, 28]. Other authors choose to normalize equation 2.25 with the magnitude of equation 2.24, which leads to different cutoff values being required[44, 31, 45]. Overall the choice to normalize makes little difference in the ability to detect crystalline clusters in systems.

For each pair of particles that correlate sufficiently we define solid-like bonds if the values of $q_l(i,j)$ exceed a certain threshold cutoff q_c:

$$S(i) = \sum_{j=1}^{N_n} H(q_l(i,j) - q_c), \tag{2.26}$$

where H is the unit step function. Particles that then possess sufficient numbers of solid-like bonds S greater than or equal to another cutoff s_c are considered to be in a crystalline local environment and are eligible for particle clustering by joining neighbors within a local distance cutoff to locate disjoint clusters.

While broadly tunable for a wide variety of structures, this metric of ordering requires at least four parameters, l, r_{cut}, q_c, and s_c. It also requires a choice of neighbor environment, usually taken to be a fixed r_{cut}. Our implementation also allows for selecting the k closest neighbors, for instance $k = 12$ for FCC, and for only using a radial shell of neighbors for computing equation 2.25. This large parameter search space often requires training on known fluid and crystal frames to find desirable values for the cutoffs.

This order parameter is capable of identifying many common structures from disordered fluids, such as face centered cubic, body centered cubic, diamond, single including the common such as simple cubic, body-centered cubic, face-centered cubic, hexagonal close packing, diamond, as well as more complex structures such as the dodecagonal quasicrystal studied by Engel[46] created from a pair potential. A section of quasicrystal is shown in Figure 2.1, illustrating the use of this order parameter in distinguishing fluid from solid. This order parameter is used to analyze simulations of polyhedra in chapters 4, 5, and 6.

2.5 Umbrella Sampling

The formation of clusters in the homogeneous nucleation regime is rare and without biasing methods adequate statistics cannot be determined to sufficient precision to calculate free energies. As direct sampling of simulations is inadequate we turn to the technique of umbrella sampling to help sample adequate statistics of the cluster size distribution [26, 27, 28, 44, 47]. In this approach, a harmonic bias potential ('umbrella', after the shape) is added to the simulation to allow for sampling near a particular value of an order parameter. Here we use N, the size of the largest cluster, in the simulation as the order parameter and bias towards a target size N_t by adding the harmonic biasing potential shown in equation 2.27.

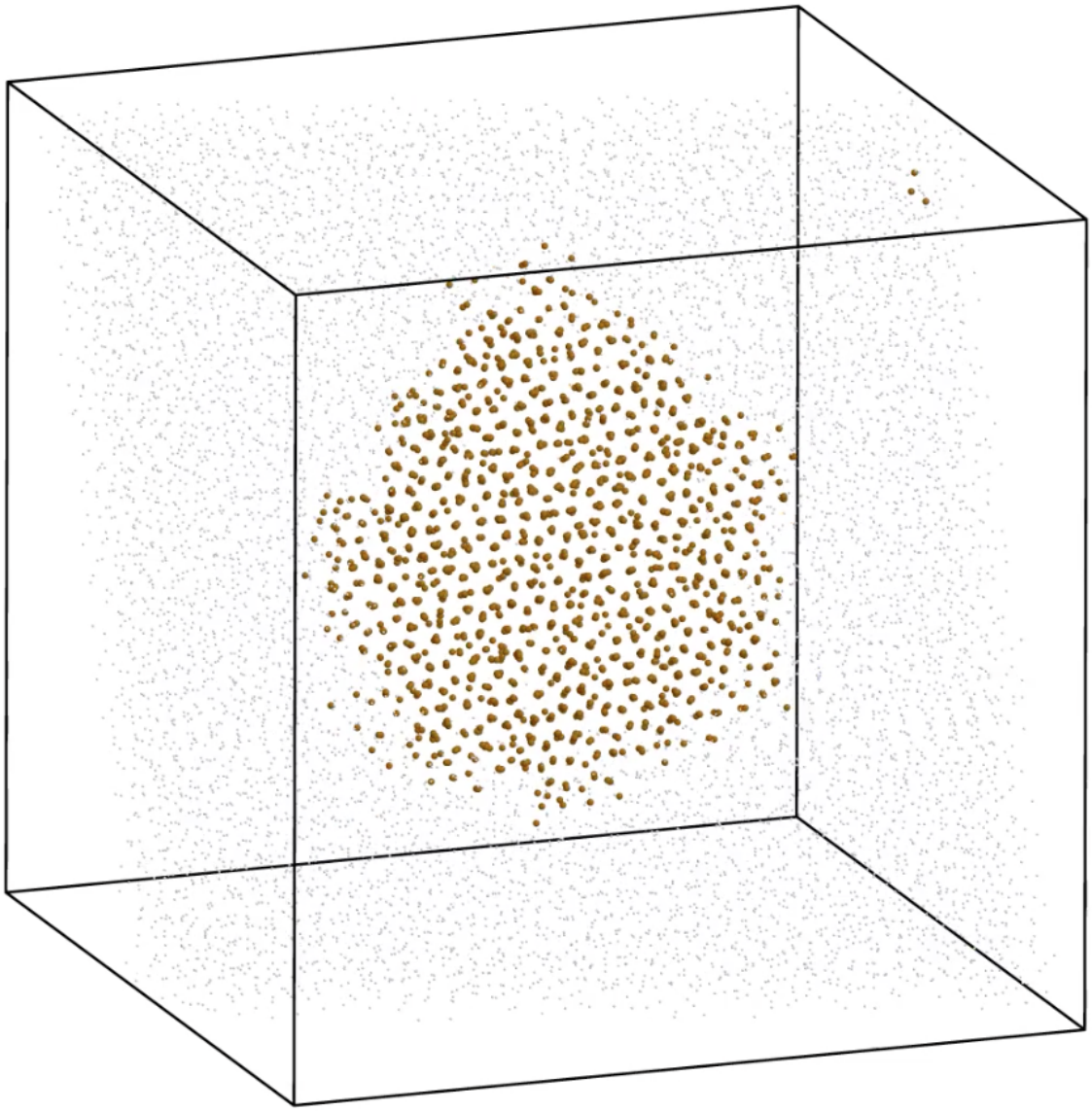

Figure 2.1: *Solid-Liquid order parameter identifying a quasicrystal.* Quasicrystalline particles are colored yellow. Fluid particles are displayed as small grey dots and only a thin slice of the dense simulation box is shown to make it easier to see the structure. Parameters were set to $l = 10$, $q_c = 5.2$, $s_c = 20$. For computing q_{lm} (equation 2.24) and solid particle clustering a radius of up to 2.1 was used to define neighboring particles. For computing $q_l(i, j)$ in equation 2.25 particles within a shell between r_{min} and $r_{max} = 3$ were used. These convoluted parameters were found by brute force training on files of known disordered and ordered states. This image was produced by Michael Engel.

In practice, short Monte Carlo trajectories (say 25 MC cycles) are run on the system before evaluating the bias energy to amortize computational expenses of the order parameter. Measurements of the cluster size are taken after each trajectory, and the energy is evaluated as

$$U_N = k(N - N_t)^2. \tag{2.27}$$

Values of this potential energy are added to the total potential energy $\Delta\mathcal{U}$, which is used as the energy in the Monte Carlo acceptance criterion. For hard particles, this is the only relevant energy. We show the potential containing the order parameter we use, but it can be any other that tracks desirable system properties.

The use of this bias potential is to move the simulation to sample values of the order parameter that would normally be too rare to get statistics. The end goal, however, is to compute free energies of different values of this order parameter, which requires a probability distribution consistent with the original ensemble. The count of largest clusters of size N given a system containing N_P particles is denoted $C_N(N)$. Using this observable, sampled from many measurements over the system we can compute an ensemble average similar to that in equations 2.17, but we must weight the states by the inverse of the applied bias to the simulation:

$$\langle C_N \rangle = \frac{\sum_i^M C_N e^{\beta U_N(N)}}{\sum_i^M e^{\beta U_N(N)}}, \tag{2.28}$$

and also normalize by the remaining correction to the partition function, which was previously only the number of samples. After sampling many microstates, we can construct a probability distribution of having a cluster of size N within the system,

$$\frac{p(N)}{N_p} \simeq \frac{C_N(N)}{N_p} \tag{2.29}$$

The equality holds if the probability of having a second cluster of size N is extremely small[27]. For sections of $p(N)$ where this is not true, direct sampling of the cluster size distributions considering all clusters, instead of the largest is required. From this we can compute free energy barriers using the probability distribution

$$\beta G(N) = -\ln P(N) \tag{2.30}$$

Free energy curves have an arbitrary shift for each sampled target N_t, and need to be aligned to form a single contiguous curve. We align the free energy curves for different N_t using the weighted histogram analysis method[48], and shift the overall curve such that $G(N = 0) = 0$.

In this work we use a spring constant $k = 0.1$. To detect face-centered cubic structures we use the order parameter described in the prior section, with $l = 6$, $Q_c = 20$, $S_c = 6$, and an $r_{cut} = 1.7$ about unit volume shapes. Once equilibrated, for each simulated state-point as a function of N_t, pressure P and shape we perform at least 50,000 umbrella trials on 10 independent replicates. Small clusters are sampled directly without this technique, and for larger clusters we use values of $N_t = 15$ for the first target cluster size, and then multiples of ten (starting a twenty) until we have sampled sizes large enough to exceed the free energy maxima.

2.6 Thermodynamic Integration

The chemical potential μ between two phases at pressure P is calculated by integrating the fluid and solid equations of state from the coexistence pressure to P. We can derive the necessary integral starting with the thermodynamic potential for Gibbs free energy,

$$dG = -SdT + VdP + \mu dN. \tag{2.31}$$

In a hard particle NPT ensemble, we have both fixed N and no relevant temperature scale for dT so dG simplifies to

$$dG = VdP. \tag{2.32}$$

As $\mu = G/N$ for a one component system, the chemical potential then follows the relation

$$\frac{d\mu}{dP} = \frac{V}{N}. \tag{2.33}$$

By definition, the chemical potential between the fluid and crystal is zero at the coexistence pressure, so the driving force $\Delta\mu$ between the two phases is given by

$$\Delta\mu = \int_{P_{coex}}^{P} \frac{V_{cry}}{N} - \frac{V_{flu}}{N} dP', \tag{2.34}$$

where V_{cry} and V_{flu} are the simulation box volumes for a system of N particles. This chemical potential represents the Gibbs energy per particle to rearrange from fluid to crystalline solid in the thermodynamic limit. The coexistence pressure P_{coex} can be determined by using the method of interfacial pinning [49, 50].

2.7 Interfacial Pinning

Interfacial pinning is used to determine coexistence pressures that are in turn used to calculate the chemical potential via thermodynamic integration[49, 50].

This method runs a two-phase simulation that holds a fluid and solid in an elongated box. A harmonic potential is applied to the system that attempts to force the stability of the phase coexistence to be half fluid and half solid in a manner similar to the umbrella sampling described previously. A two-phase simulation is constructed such that the two phases, fluid, and solid, coexist along the z axis, and such that the box dimensions in the xy-plane are appropriate for an equilibrated crystal at the given pressure. In the NPT simulation only box length L_z is allowed to vary. As the interfaces span the box with constant L_x and L_y, changes in the amount of fluid and solid do not alter the interfacial area or energy long as the system remains two-phase. For each shape, several simulations are performed at different pressures. The coexistence pressure is determined by finding the pressure at which the mean applied bias energy is zero. We accomplish this search by simulating many systems at various pressures.

2.8 Potentials of Mean Force and Torque

We calculated the potential of mean force and torque (PMFT) to identify particle neighbor bonds[22, 23]. Local particle bond environments are rotated with respect to the orientation of the single central particle, and binned in Cartesian space to construct a probability distribution of particle neighbors in $\mathbb{R}^3$, integrating out orientational degrees of freedom of the adjacent neighbors. The procedure is averaged over many simulation states and once sufficient statistics are gathered, we then express and plot the distribution in units of free energy by taking the negative logarithm of the probability distribution.

CHAPTER 3

Self Assembly of Lithium Yttrium Fluoride Bipyramids

In this study we look to explain the behavior of experimental self-assemblies of $LiYF_4$ bipyramids that assemble into two unique morphologies. This work is taken from a paper with our collaborators, and is described here to focus on the simulations that I contributed. Full details about the self-assembly experiments and extensive synthesis procedures will be available in our publication, which is currently in preparation for submission:

"Size and Shape-Controlled Synthesis of Doped $LiYF_4$ Upconversion Nanophosphors and their Shape Directed Self-Assembly." Xingchen Ye, Joshua E. Collins, Richmond S. Newman, Michael Engel, Jun Chen, Guozhong Xing, Cherie R. Kagon, Sharon C. Glotzer, and Christopher B. Murray. *Preprint*[51].

Simulations were performed by Richmond S. Newman under the supervision of Michael Engel and Sharon C. Glotzer. Experiments were conducted by the remaining coauthors.

The goal of the simulations produced was to understand the self-assembly mechanisms for the parallel and antiparallel bipyramid assembly motifs shown in Figure 3.1(a) and (b). Additionally simulation phase diagrams also explained a less common assembly 3.1(c), and a bulk body-centered tetragonal structure 3.1(d).

3.1 Experimental Assemblies Synopsis

My collaborator Xingchen Ye synthesized and performed self-assembly experiments on $LiYF_4$ square bipyramids coated with oleic acid and suspended in hexane over a substrate of diethylene glycol subphase, which is immiscible to hexane. The square bipyramids have an elongated axis such that one tip-to-tip distance is nearly twice the other, with lengths of about $100 - 200$nm, depending on synthesis. The particles are found to self-assemble after the hexane phase has evaporated, leaving monolayer films consisting of one of two

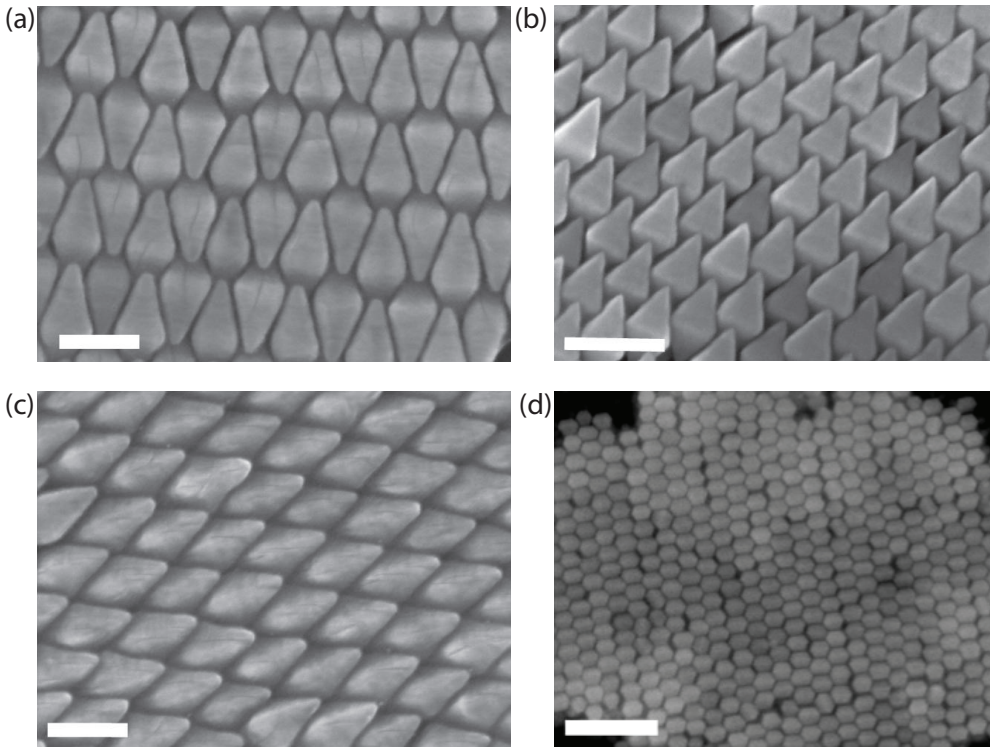

Figure 3.1: *Selected SEM images of assemblies.* Assemblies of $LiYF_4$ nanobipyramids by our collaborators. (a) Alternating motif, (b) parallel motif, (c) rare parallel motif (d) body-centered tetragonal bulk structure from tip-truncated bipyramids. Scale bars are (a−c) 100nm, (d) 50nm. Reproduced from our work [51].

different motifs above the diethylene glycol which are then removed for characterization. Because the particles successfully self-assemble, we suspect the particles concentrate in the hexane above the diethylene glycol, and are not embedded in the interface where they would be subject to strong capillary forces that would likely cause irreversible aggregation. The details of the particle synthesis conditions are in our paper[51], which also includes discussion of building block tuning, such as altering the aspect ratio, size, and etching the tips with Mn salts.

3.2 Bipyramid Simulation Methods

We model the bipyramids as hard particles, with the six vertex coordinates V given as:

$$V = (\pm 1, 0, 0), (0, \pm 1, 0), (0, 0, \pm A), \tag{3.1}$$

for aspect ratio A. One of the important features of the system is that particles in the resultant assemblies lie within a plane against the substrate. To model this behavior we impose a confining harmonic potential on the system, that applies an energetic penalty for particle vertices exiting a narrow region around the $z = 0$ plane. That is, we confine shapes by summing over their vertices

$$U = k_z \sum_{i=1}^{N_v} (|z_i| - \delta_z)^2 H(|z_i| - \delta_z) \tag{3.2}$$

where $k_z = 100$ is the spring constant, $\delta_z = 0.7$ is the width, H is the unit step function, and z_i is the z-position of vertex i. This allows us to effectively simulate a quasi-2D system where the particles are constricted along the z-axis, but free to move and rotate within a region near the xy-plane. This potential energy is added to the system for all particle vertices in the system. We also perform simulations using edge-truncated shapes, as well as investigate the role of face-centered attractive patches. The truncated bipyramids truncation are shown in Figure 3.2. As an approximation of face attractions, we use a triangular potential with depth ϵ and length 0.4 across the face of the particles with the particles sizes defined as above. The short range of this potential allows for patches on a given particle to only interact with one other patch on another particle.

Two order parameters were used to describe the simulations. The first, the local orientational order parameter, ϕ_l, discriminates between parallel and antiparallel bipyramid ordering. It sums over all particles N_p the dot products of local orientations v of each

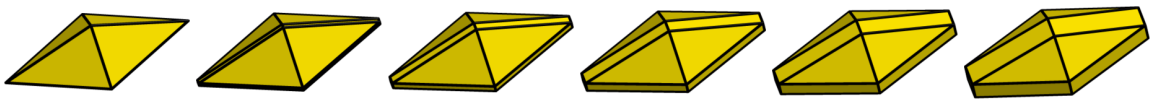

Figure 3.2: *Truncated bipyramids*. Images of bipyramids with aspect ratio $A = 2$, ranging from untruncated $t = 0.0$ (left) to a truncation of $t = 0.20$ (right) in intervals of $\delta t = 0.4$.

particle i with neighbors j,

$$\phi_l = \frac{1}{N_p} \sum_{i=1}^{N_p} \frac{1}{N_N} \sum_{j=1}^{N_N} v_i v_j, \tag{3.3}$$

where N_N is the number of local neighbors of particle i. Neighbors are defined as those in the local region where there are only typically 4 neighbors, and the particle orientations v_i are chosen in the direction of the vertex on the elongated bipyramid axis with positive z-component, projected into the xy-plane. The value of ϕ_l is 1 in ideal parallel arrangements, and -1 for antiparallel arrangements. Intermediate values near zero, however, can correspond to either a fluid, polycrystalline system, or a series of parallel and antiparallel stacking faults.

To distinguish the other cases, we define the global orientational order parameter,ϕ_G, as the variance of the histogram of all particle orientations in the system, given as

$$\phi_G = \text{Var}(H(\text{atan2}(e^{i2\theta_i}))), \tag{3.4}$$

where θ_i is the orientation angle of the vector v_i. The complex exponential is converted into $x + iy$ format, and given to atan2, the two component inverse tangent that accounts signs and can return angles in all four quadrants, *i.e.*, outputs on a range of $[-\pi, \pi)$, as opposed to atan on range $[-\pi/2, \pi/2)$. The complex exponential with $2\theta_i$ reflects that we are only looking at axial alignment, and not the direction (so the calculation is invariant under rotations by π). This histogram is approximately uniform for liquid phases and has low variance, and sharply peaked for axially aligned systems, and has high variance. In this work the number of bins chosen was 50, and the order parameter was scaled linearly to lie within 0 and 1 by normalizing by the largest values found in any system.

Simulations in this study looked at $N_p = 25^2 = 625$ particles, and were equilibrated for at least 15 million MC cycles. All phase diagrams are based on averaging the above order parameters from five replicate runs.

3.3 Bipyramid Simulation Results

To understand our collaborator's parallel and antiparallel bipyramid motifs shown in Figure 3.1(a) and (b), we performed three main sets of simulations: 1) a study of different aspect ratios, 2) a study of different truncations at $A = 2.0$, and 3) a study of face-centered attractive patches.

In Figure 3.3 we show the results of our hard particle simulations confined to a narrow interface. We studied aspect ratios between $A = 1$, an octahedron, to $A = 3$, a more elongated bipyramid than observed in the experiments, and ran NVT simulations at several number densities ρ. Each simulation statepoint is quantified using a local parallel order parameter, which measures whether or not a particle is aligned with (parallel) or against (antiparallel) its four neighbors. This order parameter maps out a phase diagram which is shown in 3.3(a). This order parameter works well for characterizing the systems for $A \geq 1.4$, however there is no particular favored 'tip' for octahedra, as the particles can easily adopt one of three equivalent orientations when forming the triangular tiling shown in Figure 3.3(b). The colors shown are degenerate as there is no specific tip of the particles, and the particles align into one of three equivalent orientations. For small deviations from this aspect ratio, a preferred orientation does not appear until the bipyramids are sufficiently elongated. In Figure 3.3(c) we show that near $A = 1.6$ we can form well-ordered parallel motifs using this hard particle model suggesting that excluded volume alone is sufficient to describe this phase given the constraints of the particles being located on the interface. We also find that with much larger aspect ratios near $A = 2.8$ we are able to find systems with an abundance of stacking faults between the parallel and antiparallel motifs which overall are weakly antiparallel (see Figure 3.3(d)). This ordering, however, is highly defective compared to that seen in the experimental assemblies.

To look for factors that might stabilize the antiparallel phase, we proposed two models: one of edge truncation, and one of face attractions that we believe may alter the behavior of the particles. The model of edge truncation was proposed to account for the excluded volume of the particles being rounded from their oleic acid coating. The model of attraction was introduced to capture the expected attraction between nanoparticles.

We simulated the truncated particles shown in Figure 3.2. NVT simulations were performed for ten nontrivial truncations, over several number densities. The results of this set of simulations are shown in Figure 3.4. The simulations were analyzed by computing phase diagrams of local orientational ordering (Figure 3.4(a)) and also by computing global axial order (Figure 3.4(b)), which measure the degree of global axial ordering to distinguish aligned regions from disorder. The results of the local directional order parameter

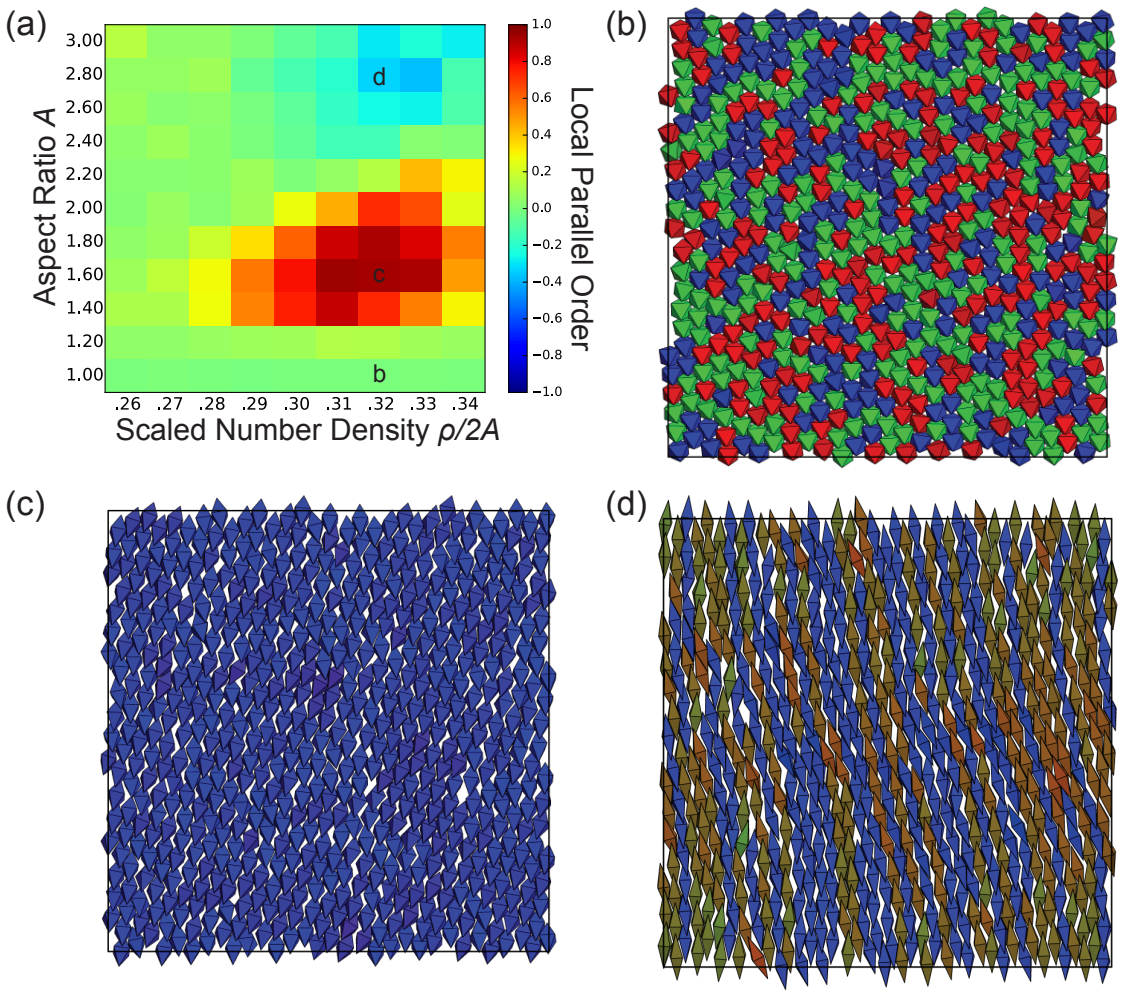

Figure 3.3: *Bipyramid aspect ratios*. (a) Local parallel order parameter for various aspect ratio of bipyramids. Labeled locations correspond to (b), (c), and (d). (b) Octahedra at $\rho = 0.32$ and $A = 1.0$ assembled into a triangular lattice. Particles are colored by their orientation in the xy-plane, with orientation given by the $\pm A$ vertex with a positive z-component. (c) Bipyramids at $\rho = 0.32$ and $A = 1.6$ form a parallel-aligned motif. (d) Bipyramids at $\rho = 0.32$ and $A = 2.8$. Figure from our collaboration[51].

display two distinct regions of strong parallel ordering, separated by a region of antiparallel ordering. The global axial order suggests the system possesses good axial alignment along a narrow band of number densities between $\rho = 0.29$ and $\rho = 0.32$, which drifts slightly lower with increased truncation. This helps show that the regions of neither parallel or antiparallel ordering in Figure 3.4(a) still are aligned, but with large numbers of stacking faults, similar to the untruncated systems at higher aspect ratios shown in Figure 3.3(d). The low density regions with neither local directional nor global axial order remain too fluid to crystallize, and the high density regions correspond to systems that are heavily polycrystalline and are kinetically frustrated from fully assembling. Simulations are shown at the local extrema of the local directional order parameter, in parallel motif Figure 3.4(c), antiparallel motif in Figure 3.4(d), and a rolled parallel phase in Figure 3.4(c) where the particles no longer lie with faces parallel to the xy-plane. This truncation model reproduces the three monolayer phases shown in the experimental assemblies, Figure 3.1.

Further simulations were run on $A = 2$ bipyramids with short-ranged attractive patches. The results of these simulations are shown in Figure 3.5. We show the local and global order parameters in Figure 3.5(a) and (b), and found that this model stabilizes antiparallel ordering as well. Interaction energies of $\epsilon = 3k_bT$, illustrated in Figure 3.5(d), were found to stabilize antiparallel ordering as well as those found in the truncation $t = 0.12$ systems Figure 3.4(d).

The addition of Mn salts causes the tips of the bipyramids to be lost and exposes new facets. Such nanoparticles assemble into a 3-dimensional body-centered tetragonal structure, which can be assembled easily in a simulation with full periodic boundary conditions (without the confining potential used for the monolayer simulations above). Images of experimental and simulation assemblies are shown in Figure 3.6. Entropy alone is sufficient to stabilize these assemblies.

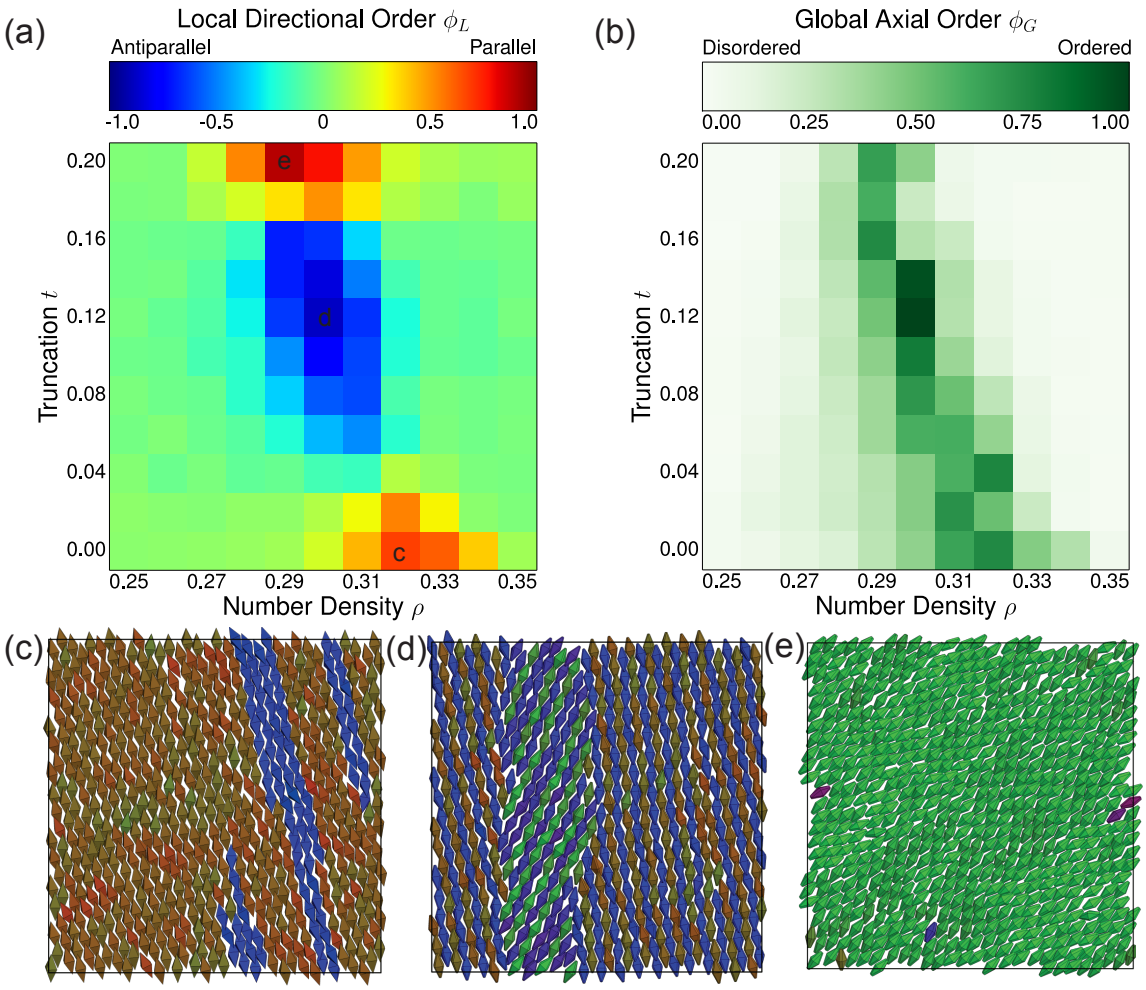

Figure 3.4: *Bipyramid Truncations*. (a) Local directional order phase diagram for the aspect ratio $A = 2$ edge truncated bipyramids illustrated in Figure 3.2. Locations labeled on this subfigure correspond to the statepoints shown in (c),(d), and (e). (b) Global axial order parameter for the same system. (c) Parallel ordered phase assembly, (d) Antiparallel ordered phase assembly, (e) Rolled-parallel ordered phase assembly. From our publication[51].

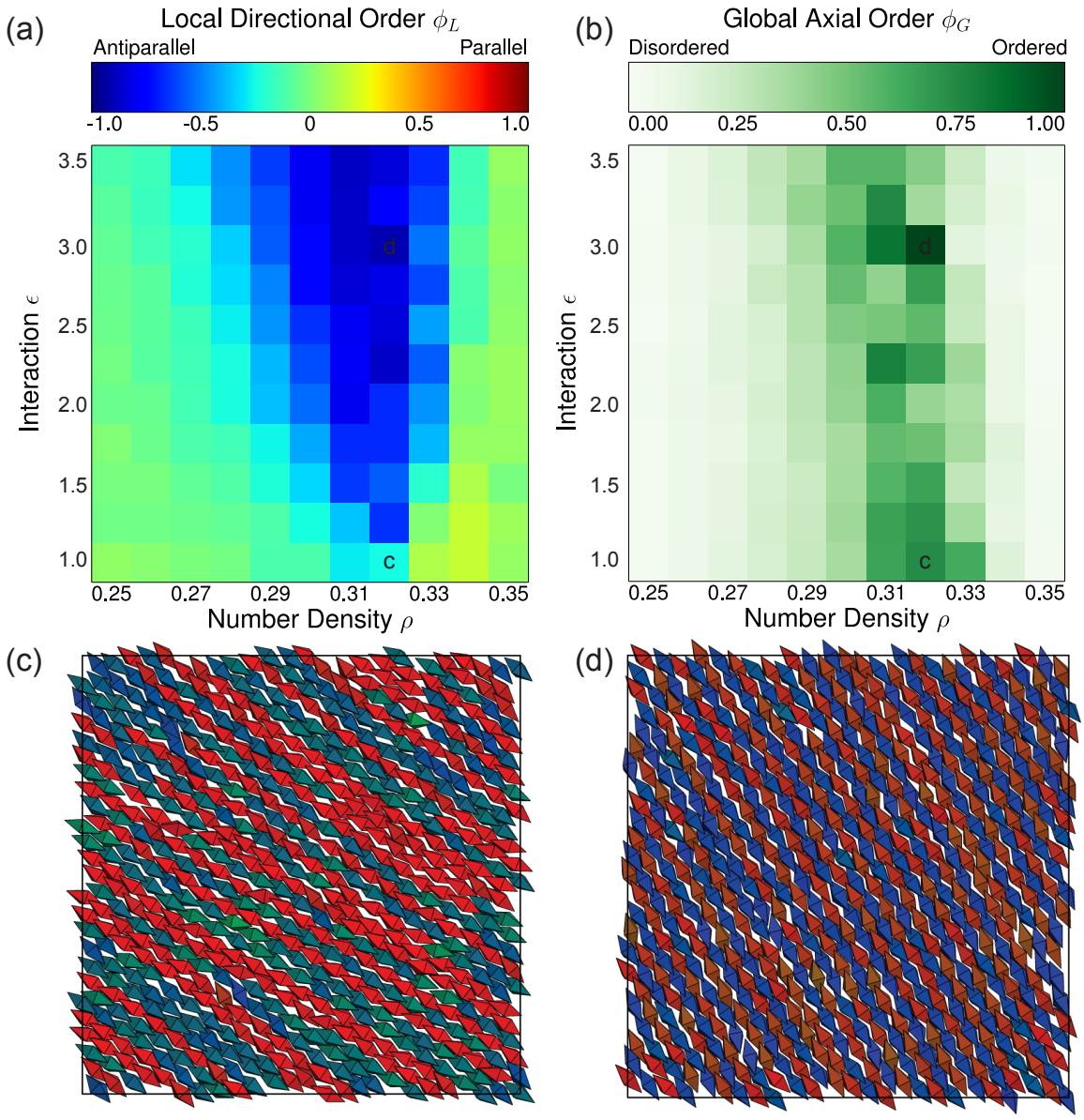

Figure 3.5: *Face-attractive bipyramids*. (a) Local directional order phase diagram for the aspect ratio $A = 2$ bipyramids, with face-centered attractive patches (Details in section 3.2). Locations marked on this subfigure correspond to the simulations shown in (c) and (d). (b) Global axial order parameter for the same system. (c) Poor quality mixed parallel and antiparallel phase occurs when the interactions are weak at $\epsilon/k_bT = 1$. (d) Stronger face centered attractive patches at $\epsilon = 3/k_bT$ lead to the formation of highly ordered antiparallel phases. From our collaboration[51].

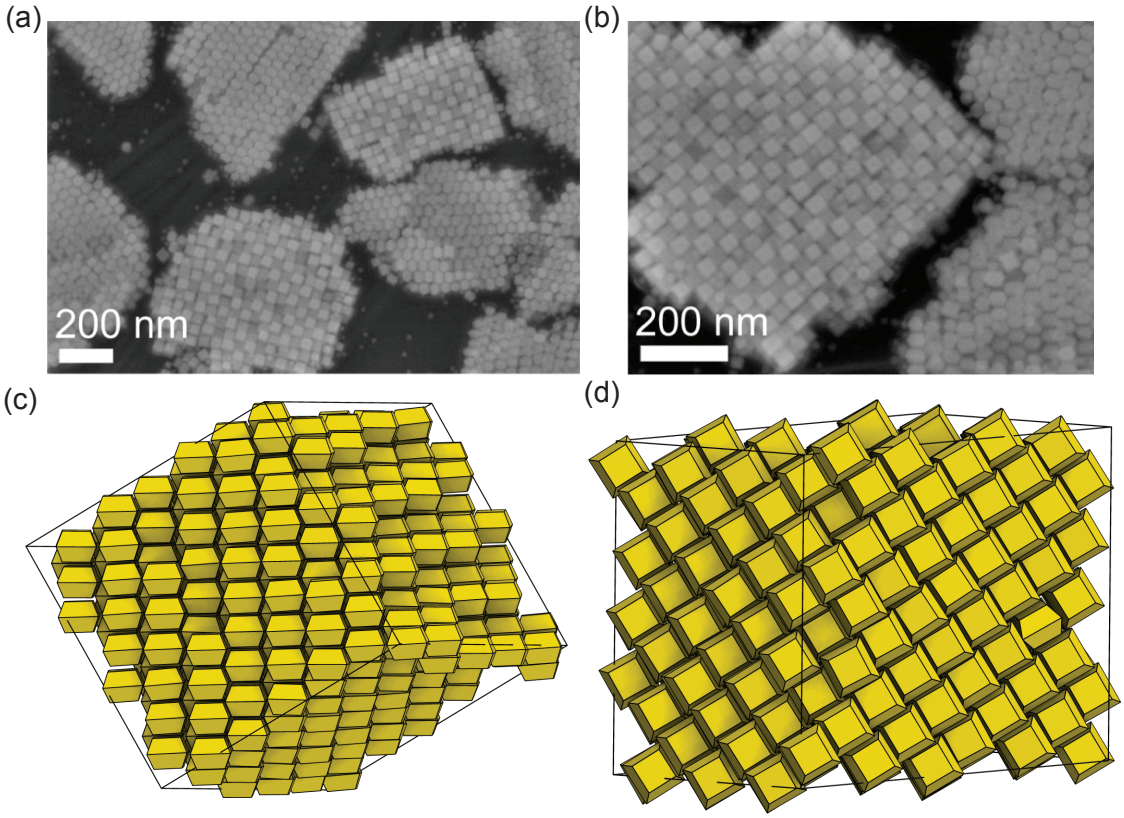

Figure 3.6: *Tip-truncated bipyramids*. (a,b) SEM images of tip-truncated bipyramids forming a body-centered tetragonal structure. (c,d) Simulations of similarly-shaped hard particles readily crystallize into the same bulk structure. From our work[51].

3.4 Concluding Remarks - Bipyramids

Xingchen Ye *et al*. self-assembled monolayers of tetragonal bipyramidal nanoparticles and discovered two dominant competing arrangements. Monte Carlo simulations were used to successfully explain the observed behaviors and discovered two potential mechanisms to stabilize the more unusual antiparallel motif: truncations or face attractions. We also found that ideal hard bipyramids do not readily form the antiparallel arrangements with a high degree of correlation for similar aspect ratios to the experimental lithium yttrium fluoride nanobipyramids. The antiparallel motifs could be stabilized by both truncation and interaction, and all three monolayer phases were predicted in the models of the hard particle truncation family. Hard particle simulations are also able to predict the assembly of truncated-tip bipyramids into body-centered tetragonal phases. This study demonstrates the value of simple simulation models in informing, predicting, and understanding experimental colloidal systems.

CHAPTER 4

Shape-Dependent Ordering of Gold Nanocrystals into Large-Scale Superlattices

The self-assembly of individual building blocks into highly ordered structures, analogous to the spontaneous growth of single crystals from atoms, is a promising approach to realize the collective properties of nanocrystals. Yet the ability to reliably produce macroscopic assemblies is not in hand, and key factors determining assembly quality and yield are not understood. In this chapter, we study the formation of highly ordered superlattices (SLs) with single-crystalline domains of up to half a millimeter from gold nanocrystals with several tens of nanometers in diameter. We combine experimental and computational results for gold nanocrystals in the shape of spheres, cubes, octahedra, and rhombic dodecahedra to investigate the entire self-assembly process from disordered suspensions to large-scale ordered superlattices induced by nanocrystal sedimentation and eventual solvent evaporation. Our findings reveal that the ultimate coherence length of superlattices strongly depends on nanocrystal shape. Factors inhibiting the formation of high-quality large-scale superlattices are explored in detail for each building block.

The results here are taken from our publication "Shape-Dependent Ordering of Gold Nanocrystals into Large-Scale Superlattices", Jianxiao Gong, Richmond S. Newman, Michael Engel, Sharon C. Glotzer, Zhiyong Tang. *Preprint*[52].

Jianxiao Gong and Zhiyong Tang conceived and designed the experiments. Jianxiao Gong performed the experiments. Richmond S. Newman, Michael Engel, and Sharon C. Glotzer collaboratively designed the computer simulations performed by Richmond S. Newman. All authors analyzed and discussed the results, and co-wrote the paper.

4.1 Synthesis and Assembly Experiments

Jianxiao Gong synthesized single crystalline gold nanocrystals (NCs) with four common shapes using the seed-mediated growth method[53]. Spherical NCs of diameter $\sigma = 40$ nm

were obtained by etching nanorod precursors and then grown into polyhedra by varying the Wulff shape (the shape with minimal surface free energy) of nanocrystalline gold by altering solvent chemistry. The solvent conditions effect the stability of different exposed facets and allow for the formation of different polyhedral shapes. The naopolyhedra are characterized by their type and edge length: octahedra (74 nm), cubes (69 nm) and three sizes of rhombic dodecahedra: small (sRD, 33 nm), medium (mRD, 45 nm), and large (lRD, 74 nm). Each set of NCs is monodisperse with size dispersity equal to or less than 5%. As-synthesized gold NCs with concentration of 10^{-9} mol/L were dispersed in a cetylpyridinium chloride (CPC) solution of controlled concentration. CPC molecules attach to the NC surface and offer short-range steric repulsion to counterbalance van der Waals attraction, preventing the NCs from undergoing uncontrollable aggregation. The gold NCs were allowed to assemble in tilted glass cuvettes at room temperature in an undisturbed environment by densification *via* sedimentation. As the monodisperse gold NCs gradually settled to the bottom of the cuvette over the course of one day for the largest NCs and up to a few days for the smallest NCs, local NC concentrations and collisions increased, and self-assembled SLs emerged slowly. In parallel with sedimentation, but on the slower time scale of a week, evaporation of the water contributed to the densification by reducing the volume available to the NCs. The ordered SLs dried during the final stage of the solvent evaporation, and remained in the cuvette as a bulk film with a thickness ranging from a few NC layers (at least 100 nm) to hundreds of NC layers (approximately 10 m). Films were peeled off from the cuvette wall using conductive carbon adhesive tape. The final assembly product is a free-standing film composed exclusively of a highly ordered arrangement of CPC-stabilized gold NCs in macroscopic sizes.

Scanning electron microscopy (SEM) images of SLs assembled with each of the six sets of NCs are shown in Figure 4.1. Except for spheres, all sets of NCs formed films that were visibly ordered over a distance of a minimum of several tens of microns. As expected, the geometric arrangements of the NCs inside the ordered SLs depend on the shapes of the building block[19]. Additionally, SL orientations are influenced by the substrate. The polyhedra prefer contacting the cuvette wall with one of their planar facets to achieve layers of dense packing, with the exception of RDs, which achieve a higher in-plane packing density by having a vertex in contact with the cuvette. It is evident from the SEM images that the quality of the sphere SL is the lowest among the shapes studied here. As shown in Figure 4.1(f), the spherical gold NC assembly exhibits no long-range ordering, and only diffuse rings rather than sharp peaks are discernible in the fast Fourier transform (FFT) image. The largest ordered areas in the sphere SLs are several microns in size and are visible in Figure 4.1(f). These ordered domains are significantly smaller than the size of

those in SLs assembled from RDs, octahedra, and cubes.

4.2 Superlattice Quality and Crystallographic Order

To analyze the size of the SL domains on larger scales, small-angle x-ray scattering (SAXS) measurements were carried out using the Beijing Synchrotron Radiation Facility. We observe sets of clear diffraction spots in two-dimensional SAXS patterns of all the assemblies from polyhedra (Figure 4.4(l-p), indicating three-dimensional long-range order throughout the samples. Previously reported SLs are with few exceptions[54] not single-crystalline and thus generate rings or multiple sets of diffraction spots. In contrast, there are no diffraction spots discernible for gold sphere assemblies which indicates that the ordered domain size for sphere SLs is significantly smaller than the sample dimension.

The crystallographic structures of the SLs can be determined along with analysis of the long-range order achieved for each shape. SEM images confirm the expected close-packing of RDs into the face-centered cubic lattice[22]. Each RD contacts with twelve other RDs facet-to-facet (Figure 4.4(a-d)). Also, the diffraction peaks are well indexed to the face-centered cubic lattice (Figure 4.4(q-s)). Although all sets of RDs with varying size (sRD, mRD, and lRD) show clear diffraction peaks, the smallest particle (sRD) SLs exhibit the sharpest and most intense single-crystalline diffraction spots, suggesting that, despite their relatively smaller size, their ordered domain size is the largest among the four shapes. The SL grain size may normally be obtained using the Scherrer formula from measurements of the full width at half-maximum intensity of a diffraction peak[55, 56]. However, here we observe the peak widths comparable to the resolution limit of the beamline, which corresponds to a maximally detectable domain size of 1.55 μm. As this is much smaller than the ordered domain sizes directly observed by SEM in Figure 1, the analysis of peak widths only provides a lower bound on the size of SLs. Instead, we rely on visual inspection over macroscopic distances using SEM to analyze domain sizes. For sRD, we find single-crystalline SL domains larger than 0.5 mm in extent, which are shown in Figure 4.2 by comparing the crystal orientation along the sample. Order persists over more than 100 layers for all the RD NCs regardless of their size. The observation that smaller particles have ordered domains with larger absolute size is in good agreement with our SAXS measurements.

The SAXS pattern of octahedron SLs has well-defined peaks that cannot be assigned to a single lattice type shown in Figure 4.4(o) and (t), in contrast to SLs of RD. Indeed, as the SEM analysis in real space reveals, octahedral NCs frequently assemble in two crystallographically distinct stacking modes of close-packed hexagonal planes: a base-centered

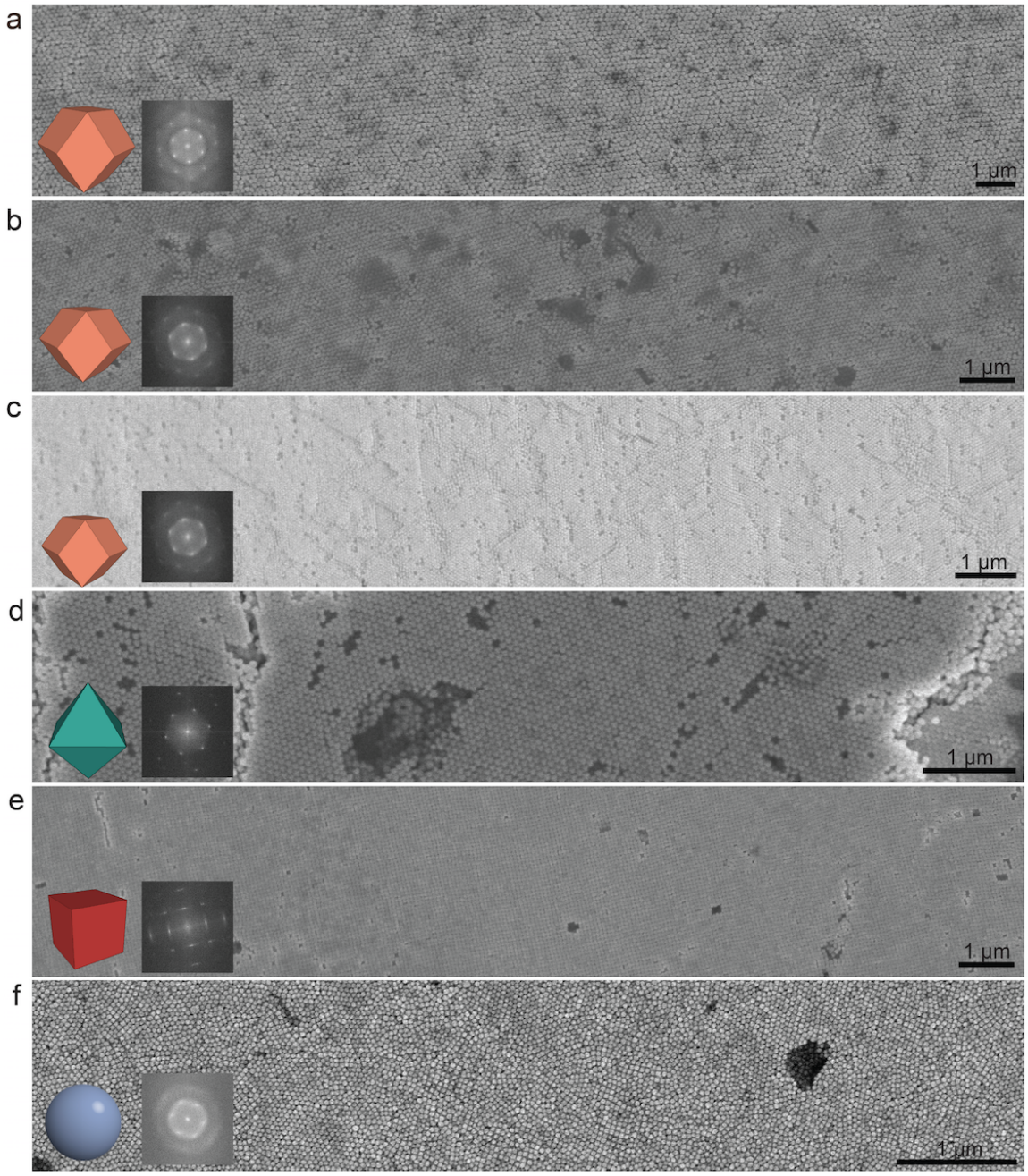

Figure 4.1: *Large-scale SEM images of superlattices using gold nanocrystals.* The nanocrystal shapes are (a) large (lRD), (b) medium (mRD), (c) small (sRD) rhombic dodecahedra, (d) octahedra, (e) cubes, and (f) spheres. The view is chosen perpendicular to the bottom of the superlattice surface, which was in contact with the glass cuvette before peeled off. The particle shape and a fast Fourier transform of the SEM image are shown as insets. As confirmed by sharp spots in the diffraction images, all superlattice films with the exception of that formed from spheres are single domains across SEM images. Figure reproduced from publication[52].

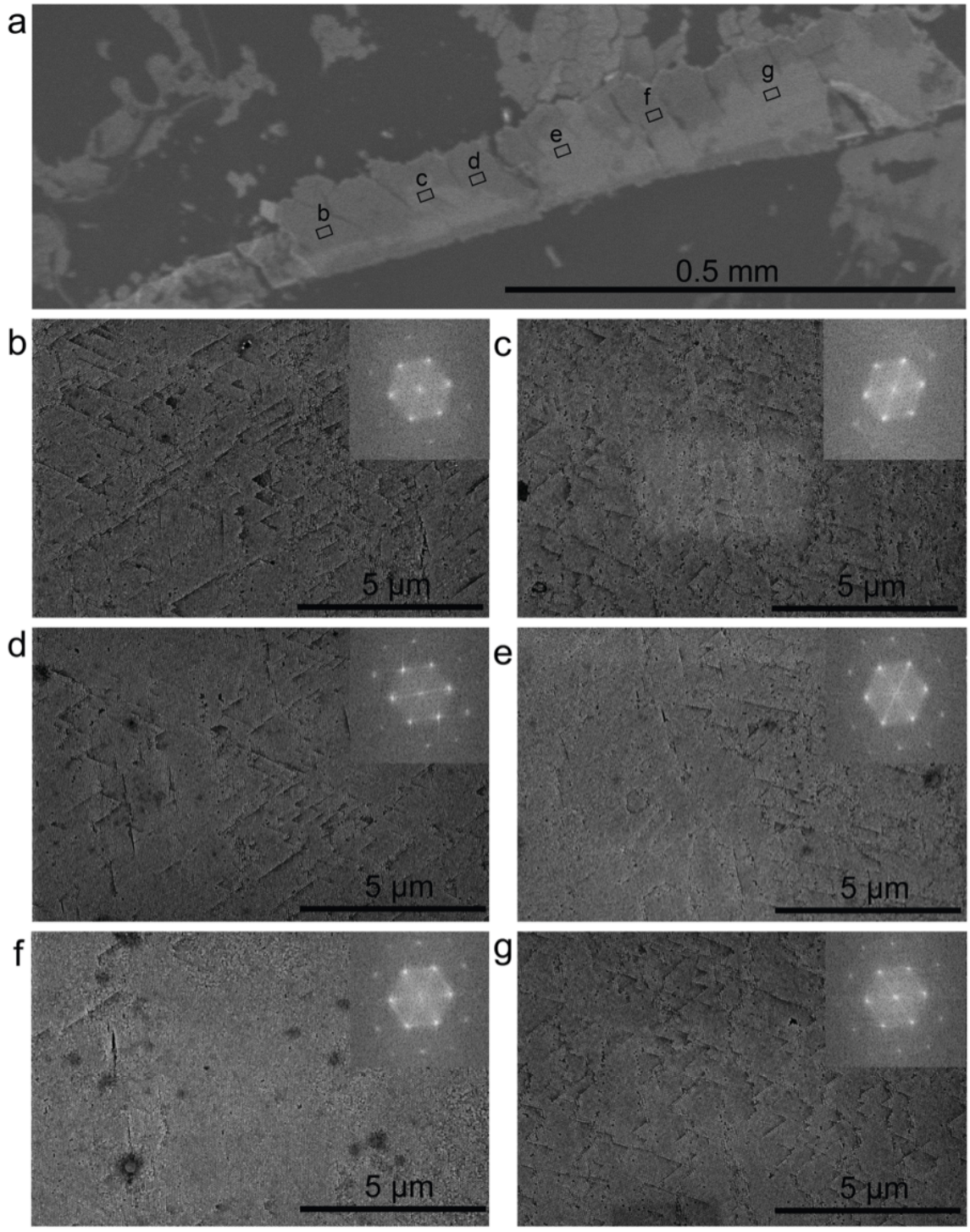

Figure 4.2: *Large-scale SEM of rhombic dodecahedra.* (a) Low-magnification SEM image of a millimeter-scale sRD sample. (b-g) Six higher-magnified images taken at various points along the sample. The fast Fourier transform patterns over different regions have identical orientation suggesting the entire sample is single-crystalline. Figure reproduced from publication[52].

monoclinic SL with a two-particle unit cell (Figure 4.4(e) and (h)) and a simple hexagonal SL (Figure 2e-g). The third structure, the densest packing of octahedra with density 18/19 known as the Minkowski lattice, appears occasionally in experiments. The Minkowski lattice, Figure 4.7(g) and Figure 4.3, was previously reported to assemble from hard octahedra in simulation[14, 57, 58]. The simple hexagonal and the Minkowski SLs have been assembled previously from silver octahedra[14]. Inside both monoclinic and the hexagonal assemblies, six NCs surround each octahedron in partial facet-to-facet contact to form dense packing layers (Figure 4.4(e)). The difference lies only in the NC orientation and the relative translational offset of the particles between the adjacent dense packing layers. In the monoclinic packing, all octahedra have the same orientation and the adjacent layers are offset; a vertex touches the center of an edge which can be seen in Figure 4.4(h). In the simple hexagonal arrangement, particles in adjacent layers have opposite orientation, but are not offset, illustrated in Figure 4.4(f) and 4.4(g). Among the possible polymorphs for the octahedron SLs, we observe the simple hexagonal arrangement most frequently. Visual inspection and sampling diffraction shows that the size of ordered domain of octahedron SL typically reaches only 100 microns, even smaller than lRD domains, indicating that shape rather than particle size is the key to determine the quality of the assembly products.

It is evident from the SEM images that cube NCs arrange into a simple cubic lattice, see Figure 4.4(i) and 4.4(j). SAXS data suggest that it is more challenging to achieve order with cubes over large areas as compared to both RDs and octahedra, Figure 4.4(p) and 4.4(u). The largest domain size visible from large-area SEM images is about 30 microns. Some amount of positional disorder can be seen in the SEMs of the cube SL assemblies that manifests as a slight drifting in the orientation of rows, which is consistent with simulation predictions[59].

4.3 Nucleation and Growth of Superlattices in Monte Carlo Simulation

The experimental results represent the first clear evidence that NC shape has a strong effect on SL quality. To understand how particle shape matters, I performed hard particle Monte Carlo (HPMC) computer simulations of the self-assembly process. Since it is not possible to reach experimental system sizes ($> 10^{7-10}$ NCs) or the time span of an assembly experiment ($> 10^5$ seconds) with present or near-future computer resources, we extrapolate from small systems and short simulation times compared to experimental conditions. In solution, the NCs interact with each other *via* van der Waals attraction of the gold cores,

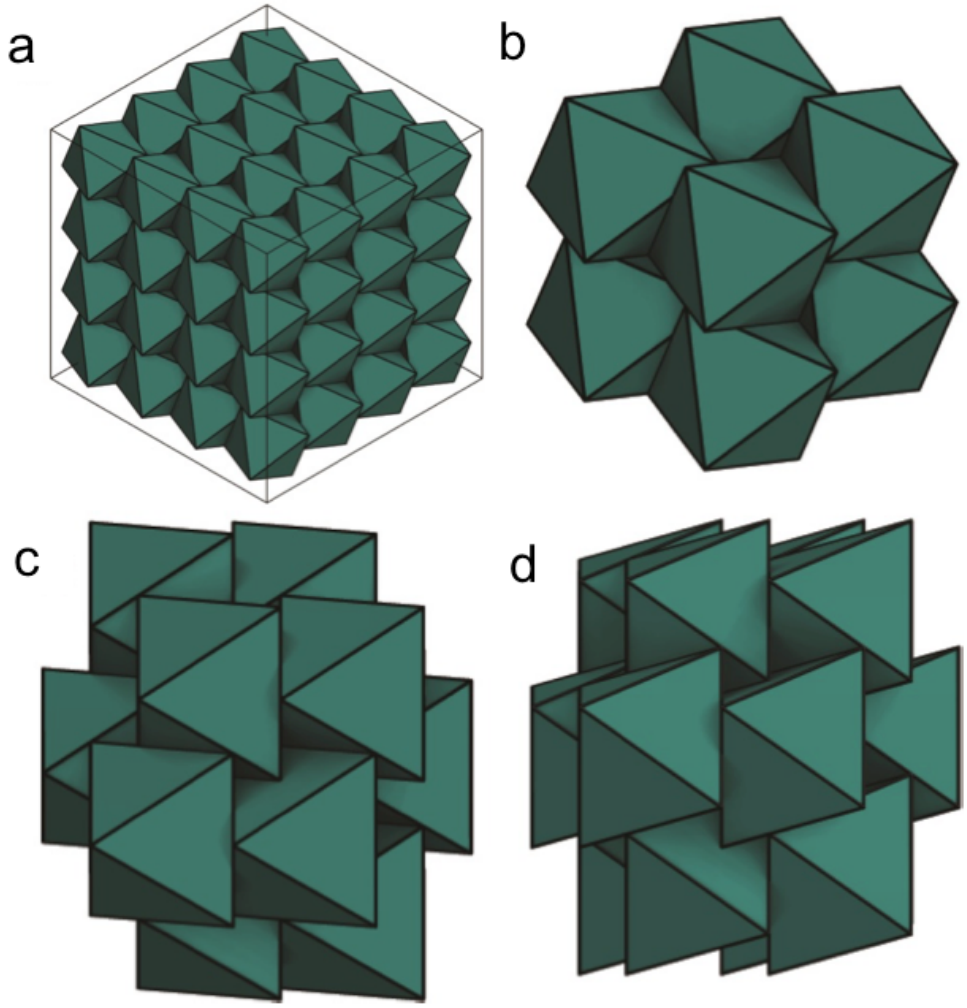

Figure 4.3: *Minkowski lattice.* The Minkowski lattice is the densest known packing of octahedra. (a) A $4 \times 4 \times 4$ Minkowski crystal. (b-d) A single octahedron surrounded by its first coordination shell of adjacent octahedra observed under three different projections. Figure reproduced from publication[52].

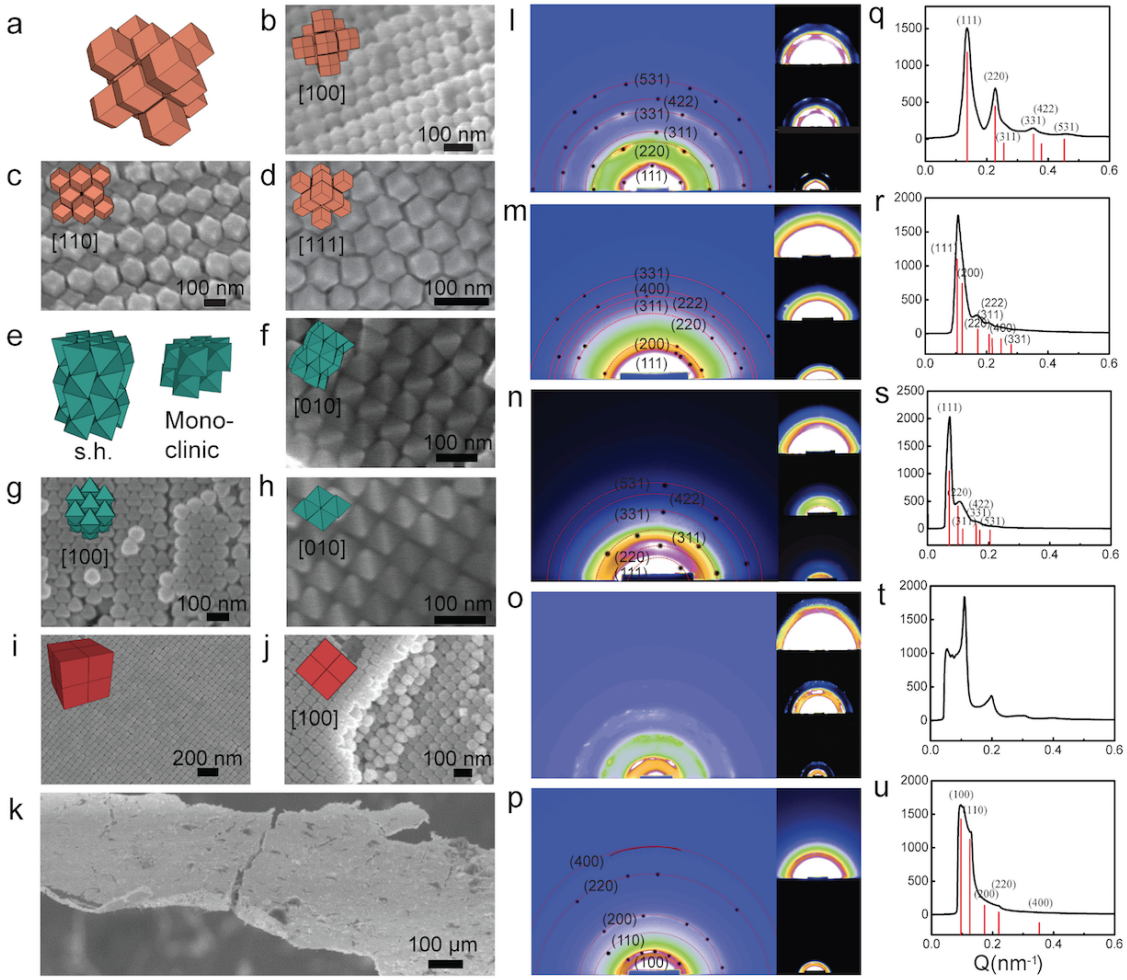

Figure 4.4: *SEM analysis of gold superlattices.* Analysis of nanocrystal superlattices in (a-k) real space using SEM and (l-u) reciprocal space using SAXS. (a-d) Rhombic dodecahedra form a face-centered cubic superlattice visible along different projection directions. (e-h) Octahedra are found predominantly in two crystallographically distinct superlattices: simple hexagonal (e-g) and monoclinic (e, h). Cubes, (i, j), assemble into a simple cubic lattice. (k) A macroscopic view shows a complete superlattice film. (l-p) Two-dimensional and (q-u) radially averaged SAXS images of assembly products exhibit clear diffraction spots and peaks, respectively, highlighting long-range order in superlattices of sRD (l, q), mRD (m, r), lRD (n, s), octahedra (o, t), and cubes (p, u). In (l-p), the indexed SAXS images are shown with low beam intensity on the left and with various higher beam intensities on the right to resolve additional diffraction peaks. Peaks are not indexed for the octahedron SL (o, t), because they correspond to the patterns of a superposition of two unique SL structures. Figure reproduced from publication[52].

depletion attraction caused by unabsorbed CPC molecules, and electrostatic repulsion of CPC ligands[60]. These interactions balance to produce contact forces that act over short distances of only a few nanometers. The hard particle model is frequently employed in the literature[19, 31, 24], and it maintains the anisotropy and orientational dependence of the effective pairwise entropic interaction. Hard polyhedra tend to align along their facets to maximize entropy and minimize free energy[55, 61]. These directional entropic forces increase in strength and range with increasing facet dominance[22], which suggests that certain polyhedral NCs should be superior candidate building blocks for forming high quality SLs compared to spherical NCs, as borne out by our experiments.

We first studied the effect of NC shape on homogenous nucleation. Crystallization of these polyhedra requires a sufficient density to be thermodynamically favorable, but needs to remain low enough such that diffusion and rearrangement times are kinetically accessible. This means there is a time window during sedimentation in which the density is high enough to form SLs, but low enough to anneal out defects. We estimate this time window by the density range over which a given system of NCs exhibits dynamics. Figure 4.5(a) summarizes, for each shape, the density window for SL formation in simulation. Notably, each shape orders robustly and rapidly at packing densities near 56%. However, the density ranges over which assembly and annealing of defects are observed vary significantly between shapes. Cubes and RDs order reliably over a wide range of densities, while octahedra and spheres require fine-tuning for assembly to occur.

Differences in the assembly behavior of differently shaped NCs affects the quality of as-formed SLs. Representative early, middle, and late time formation of SLs for each shape is illustrated in Figure 4.5(b). We compare the time in units of Monte Carlo cycles to nucleate. Time to nucleation, shown in Figure 4.5(c), is defined as the time for a system to reach 20% crystalline, and the growth duration, Figure 4.5(d), defined as the time to reach 80% crystalline from the nucleation time. As discussed in Appendix 7.2, we estimate that one second of the assembly experiment corresponds to on the order of 10^4 Monte Carlo cycles. We learn from Figures 4.5(b-d) that RDs rapidly form multiple nuclei from the metastable equilibrium fluid state at high enough density. Nuclei readily rearrange and anneal out defects, resulting in high quality SLs. In contrast, octahedra only show isolated (rare) nucleation events up to high densities. Nuclei grow quickly until crystallization is complete, but arrest sets in early. Cubes adopt local positional and orientational order almost immediately after reaching high enough density. There is neither an observable metastable fluid state nor a well-defined nucleation event for cubes, suggesting the nucleation barrier is negligible at almost all densities where the cubic SL is stable. Spheres have a comparably narrow density window where nucleation occurs[26, 27, 28]. Multiple nuclei form rapidly

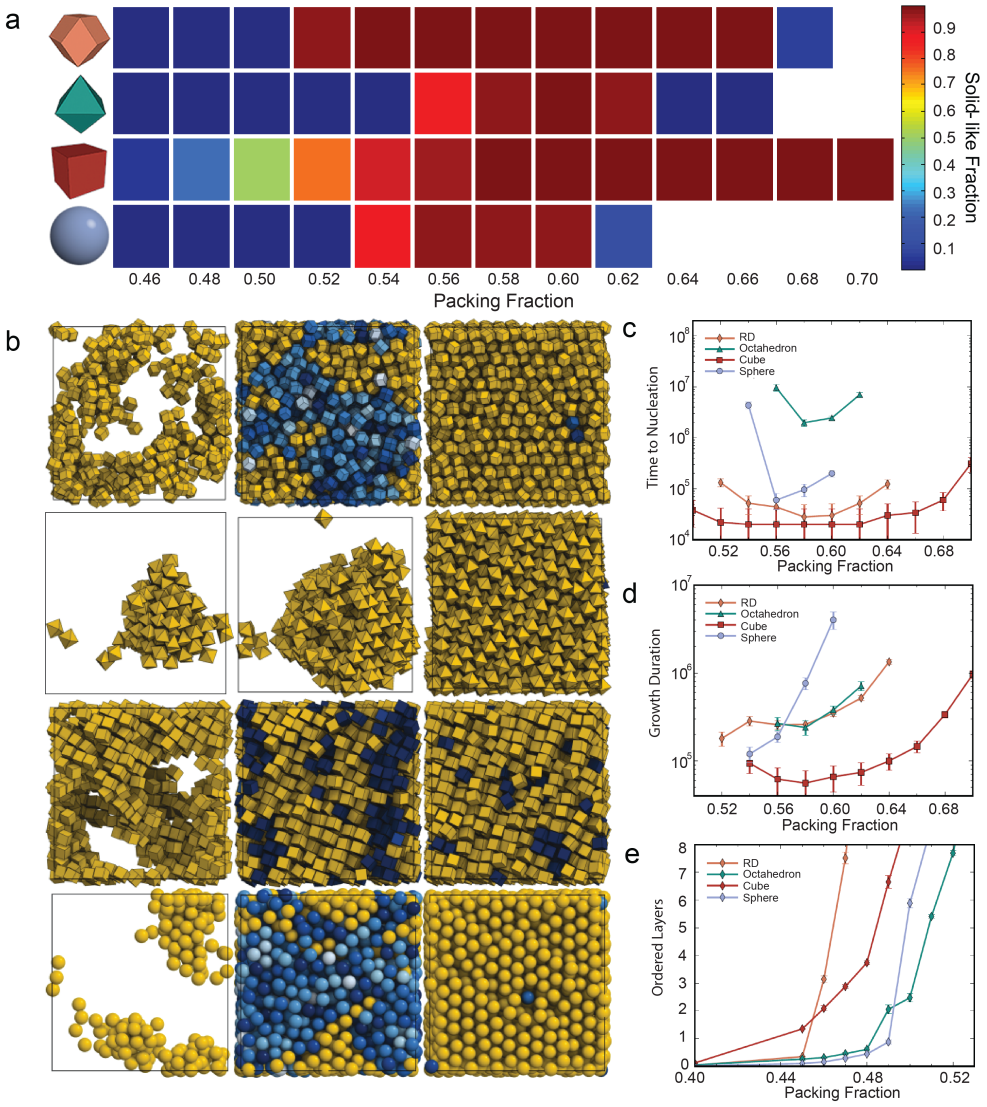

Figure 4.5: *Simulation results.* Crystallization of nanocrystal superlattices in Monte Carlo simulations of hard particles. (a) Density range where homogenous nucleation and growth occurs for each particle shape using isochoric simulations starting from configurations rapidly compressed to a selected packing density. Rectangles in a density vs. shape grid are colored by the calculated system-average local order for rhombic dodecahedra, octahedra, cubes, and spheres. Low values (blue) indicate disordered local structure (fluid), while high values (red) indicate crystalline order. Empty cells demarcate the regions beyond random close packing. Each data point represents the average of ten runs over 50 million Monte Carlo cycles. (b) Early, middle and late stage growth of homogeneously nucleating superlattices for rhombic dodecahedra, octahedra, cubes, and spheres. Densities are selected to represent a typical Monte Carlo trajectory for the particular shape and crystallization may result from several nuclei. (c) Time to nucleate, as measured by the number of Monte Carlo cycles for the system to reach 20% crystallinity. (d) Time to grow, as measured by the time required to advance from 20% to 80% crystallinity. (e) Number of ordered layers equilibrated near hard boundaries at densities lower than where homogeneous nucleation occurs. Figure reproduced from publication[52].

above the critical density. Growth is also initially rapid, but defects anneal out significantly more slowly than for RDs. Kinetic arrest sets in at lower density for spheres and octahedra than for RDs and cubes.

In experiment, large-scale SL assembly proceeds via a sedimentation process wherein the density rises slowly near the cuvette wall. To investigate the entropic influence of the cuvette wall, we employ Monte Carlo simulations with a hard wall along one coordinate axis. We find multiple crystalline layers forming heterogeneously adjacent to the wall at significantly lower densities than those required for homogenous nucleation (Figure 4.5(e) and Figure 4.6). For example, in the case of spheres, multiple ordered layers are present already at density 50%, while homogeneous nucleation starts at around 52%, consistent with prior simulations[62]. The wall affects the dominant SL structure only in the case of, octahedra and not for other shapes, in agreement with structure seen experiments.

4.4 Factors Affecting Superlattice Quality

Our results agree with earlier observations that sedimentation-driven assembly is more robust in yielding high-quality NC SLs than experiments where density is under evaporative control[14]. Equilibrium order close to the wall could be reached within a few million Monte Carlo cycles, or on the order of seconds to minutes in experiment. So, in all cases, nucleation and growth is several orders of magnitude faster than the typical sedimentation time, which suggests that the assembly process is quasistatic with respect to changes in density. Neither homogenous nucleation nor heterogeneous nucleation is the rate-limiting factor. The quality of the SLs for each polyhedron shape should be dominated by other yet-unexplored factors, which are elucidated below.

The incomplete parallel orientation of RDs found in some of the SEM images seen in Figure 4.7(b-c), and Figure 4.8 likely originates from either a quenched-in rotator phase, which is stable at intermediate density in simulations, Figure 4.7(a), or a surface effect. At higher density, NC facets align due to directional entropic forces[55, 22, 23] and ligand-induced attractive interactions, neither of which are available in spheres. As a result, stacking defects, which frequently occur with spheres[63], illustrated in Figure 4.7(n), are suppressed in RDs. We note also that another factor that may affect the quality of SLs from spheres in experiment. In contrast to micron-sized spherical colloids, the sphericity of NCs is limited by their natural tendency for the development of crystalline facets promoting shape anisotropy. Together, practical limitations of sphere NC synthesis and the more efficient packing of RDs in combination with localized orientational ordering[31] contribute to the higher quality of SLs assembled from RDs than from spheres.

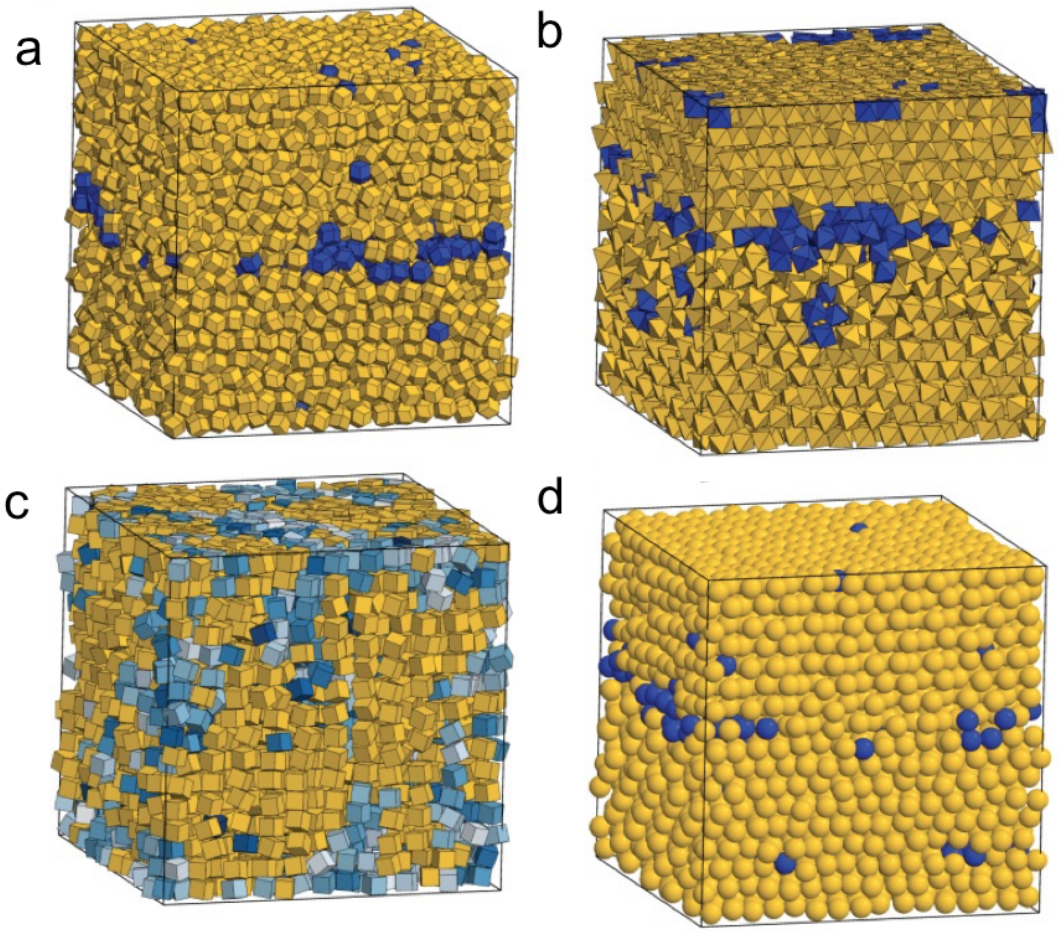

Figure 4.6: *Heterogeneous growth.* Monte Carlo simulations with impenetrable hard boundaries at the top and bottom (in the image) of the simulation box to study heterogeneous nucleation. The sides are connected via periodic boundary conditions. Simulations are conducted for systems of (a) RDs, (b) octahedra, (c) cubes, and (d) spheres. The crystal structure of the SLs observed near the wall is identical to the crystal structure observed in nuclei forming via homogenous nucleation with the exception of octahedra, which prefer the monoclinic SL near the wall. The packing fractions used in the simulations are $\phi = 0.56$ for RDs, $\phi = 0.56$ for octahedra, $\phi = 0.55$ for cubes, and $\phi = 0.54$ for spheres. Figure reproduced from publication[52].

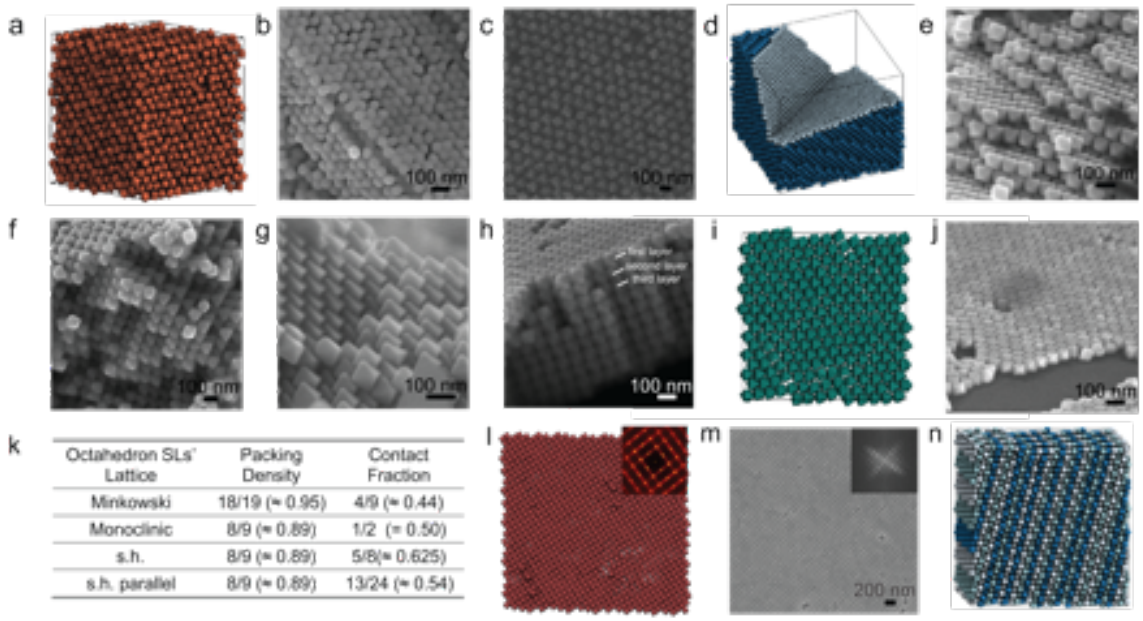

Figure 4.7: *Structural details and factors affecting quality of nanocrystal superlattices.* (a-c) Analysis of rhombic dodecahedra superlattices. In simulation we find a rotator (plastic) face-centered cubic phase at low density (a), and quenched in rotational disorder is also observed in SEM images (b, c). (d-j) Analysis of octahedron superlattices. A simulation that nucleated the Minkowski superlattice(d). In experiment we observe monoclinic superlattice (e, f), Minkowski superlattice (g), and simple hexagonal superlattice (s.h. parallel), in rare occurrences (h), alternation of octahedron orientations in layers of simple hexagonal superlattice is violated, as visible in the first and second layers of (h). Single layer of octahedron superlattice near walls in hexagonal packing in simulation (i) and experiment (j). Packing density and contact fraction of different lattices are compared in (k). (l, m) Analysis of cube superlattices. Simulation (l) and experiment (m) both show streaks in the fast Fourier transform images. (n) Monte Carlo simulations of hard spheres, typically resulting in stacking faults. Layers are colored by ABC stacking sequence (A = white; B = light blue; C = blue).Figure reproduced from publication[52].

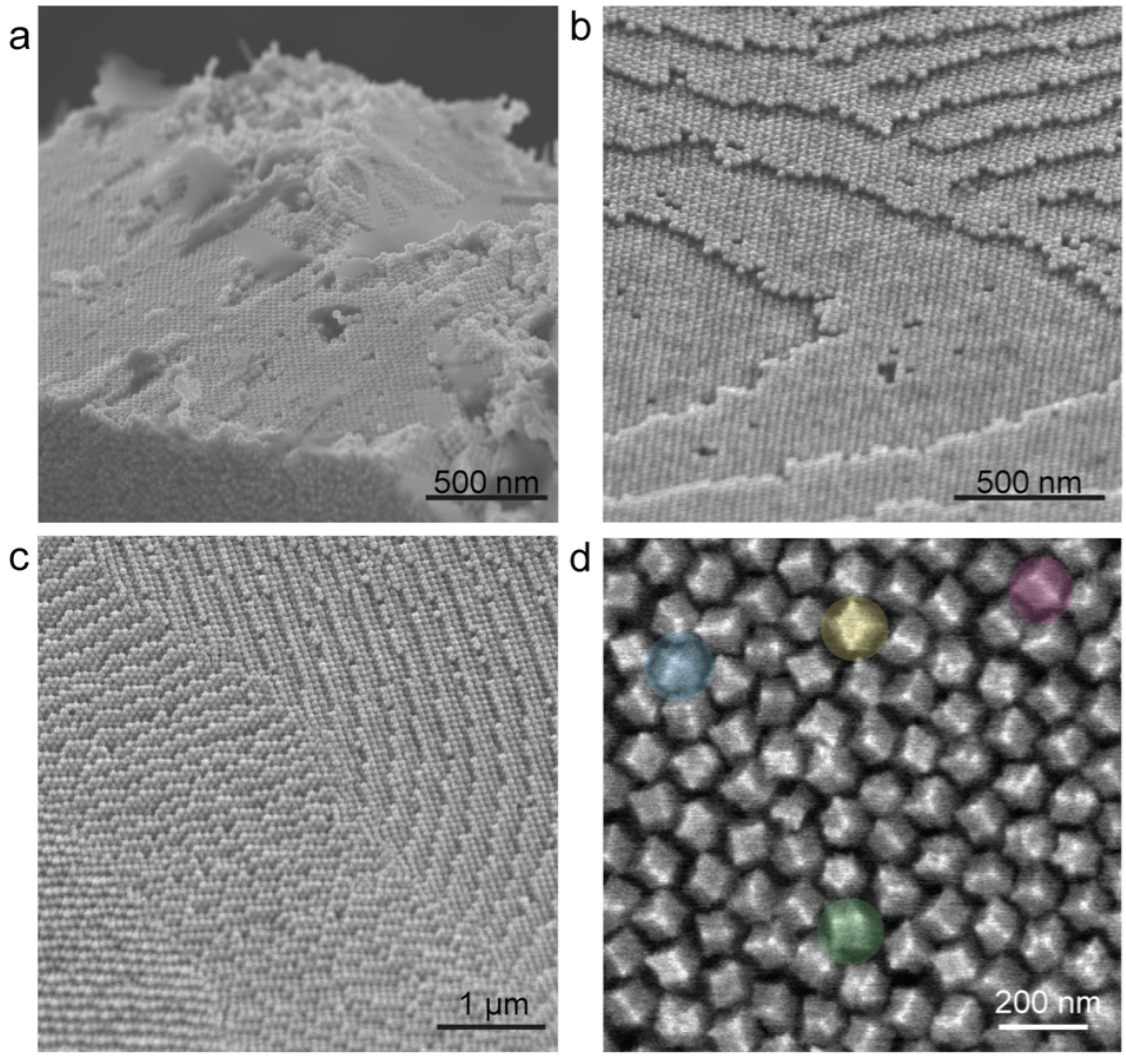

Figure 4.8: *Evidence for a rotator phase in rhombic dodecahedra.* Additional SEM images of mRD SLs from other directions aside from the bottom of glass cuvette, on which they were grown. (a) and (b) lateral views, (c) surface exposed by breaking the SL, (d) evidence for a rotator phase in mRD SLs. Typical example defects are highlighted in colors: 4-fold vertex (blue), face (yellow), edge up (purple), and improper $\frac{\pi}{6}$ rotation of a 3-fold vertex (green). Figure reproduced from publication[52].

For octahedra, the presence of competing phases poses further complexity not present in the other shapes. Homogenous nucleation simulations result in the Minkowski SL, Figure 4.7(d), or with similar probability, the monoclinic SL. Whichever SL nucleates first grows and determines the final structure. The situation might be even more complicated in experiment and depends subtly on the proximity to the cuvette walls. We compare the packing density and contact fraction of four octahedron SL candidates in Figure 4.7(k). The contact fraction is defined as the area of the octahedron surface in contact with the surface of a neighbor. Furthermore, octahedron SLs can have easy sliding modes, where 'easy sliding' means that a column or plane can shift freely without encountering obstruction. While the Minkowski SL is mechanically rigid, Figure 4.7(g), the three other SLs are stackings of dense hexagonal layers, shown in Figure 4.7(i) and (j). These layers constitute easy shear planes. In addition, the monoclinic SL has easy sliding columns, visible as grooves in the SEM images in Figure 4.7(e) and (f). Fracturing often occurs along these sliding planes and columns. The dilemma of octahedra is apparent in the fact that three of the candidate structures each possess a unique extremal property: (i) the Minkowski SL is the densest packing. It is the preferred phase under high pressure. (ii) The simple hexagonal SL has the highest contact fraction. It is the preferred phase if attraction dominates. (iii) The monoclinic SL has the highest number of shear planes or sliding modes. It is an entropically preferred phase. Only the parallel variant of the simple hexagonal SL does not have an extremal property. This explains why it is never observed outside of isolated occurrences such as Figure 4.7(h).

Cubes readily order over a wide packing density range, but tend to exhibit more positional disorder than the other shapes due to delocalized vacancies[59]. A high amount of shearing and distortion of the cubic lattice is apparent in both simulation, Figure 4.7(l), and SEM micrograph, Figure 4.7(m), and is also easily visible in the FFT (insets) as linear streaking of the Bragg peaks. This disorder is caused by the inability of cubes to rigidly lock together in the simple cubic lattice, allowing for columns and planes of cubes to collectively fluctuate and shear. The presence of localized disorder explains why the correlation length in the cube SL measured by the peak width in the SAXS data in Figure 4.4(p) and (u) is shorter than that of the other polyhedral NCs.

4.5 Concluding Remarks

We reported gold nanocrystal superlattices with coherent order over macroscopic scales as evidenced by the images of clear diffraction spots in SAXS patterns. Although both nucleation and growth depends strongly on nanocrystal shape, they are not the rate-limiting

step controlling the final quality of the assembly product. Spheres, the most widely studied nanocrystal shape, assembled the lowest quality superlattices. Octahedra superlattices order robustly but are affected by competing polymorphic equilibrium structures each stabilized by different factors, including entropy, packing, and surface attraction. The quality of cube superlattices is diminished by a high vacancy content, which cannot be overcome even by the extremely rapid assembly propensity of cubes. Finally, both experiment and simulation agree that rhombic dodecahedra are overall the best assemblers of the four shapes and is an excellent candidate for producing superlattices with the highest quality and largest single crystalline domain size. Our study reveals that nanocrystals with different shapes undergo various ordering pathways while multiple shape-related factors strongly influence the final domain size. This work not only gives new insight into the conventional crystal growth theory, but also offers unprecedented opportunity to construct high quality nanocrystal superlattices.

CHAPTER 5

Nucleation Comparison of Rhombic Dodecahedra and Spheres

In chapter 3 we discussed the equilibrium self-assembly of bipyramidally-shaped nanoparticles and mapped out their phase diagrams and in chapter 4 we discussed a combination of homogeneous and heterogeneous nucleation, as well as nucleation rates in order to study the self-assembly of different polyhedra into different structures. In this chapter, we extend the study of hard particle assembly into the nucleation of colloidal crystals of anisotropic particles and discuss how particle local environments affect the assembly process. We present a comprehensive study comparing how the same entropically stabilized crystal structure forms in two systems of monodisperse hard particle systems: spheres and rhombic dodecahedra. We investigate these systems by reporting cluster size distributions and crystallization probabilities across the range of pressures where nucleation is observed in Monte Carlo simulations and free energy barriers for nucleation. In addition, we quantify the local arrangements around the particles in both fluid and solid phases and discuss the effects on nucleation. As a model to investigate the nucleation behavior of anisotropic particles, we chose the rhombic dodecahedron as it is experimentally synthesizable from metal nanocrystals[52, 15] and also corresponds to the Voronoi cell of the face-centered cubic crystal. In a study of 145 different polyhedra, 51 different shapes were found to self-assemble this structure[19]. Among these shapes, the least spherical shape, as ranked by the isoperimetric quotient, defined as the ratio of the volume of the shape to the volume of a sphere, at constant surface area, was the rhombic dodecahedron with $IQ = 0.74$. The sphere is by definition the most spherical ($IQ = 1$).

These hard-particle systems crystallize *via* the nucleation-and-growth-type process[27, 28, 64, 31] that we have discussed previously: particles in disordered fluids need to overcome an energetic barrier to crystallize, which arises from a balance of driving forces in the pathway from fluid to solid: a favorable chemical potential $\Delta\mu$ for forming the crystal is opposed by a surface energy γ. Here we investigate in detail the conditions under which

the formation of crystal nuclei is favored in fluids of spheres *vs.* rhombic dodecahedra, highlighting the contribution of particle anisotropy to the process of nucleus formation.

The contents of this chapter are taken from our publication, "Nucleation of Hard Rhombic Dodecahedra *vs.* Spheres". Samanthule Nola, Richmond S. Newman, Julia Dshemuchadse and Sharon C. Glotzer. *Preprint*[65]. The simulations were performed in collaboration with coauthor Samanthule Nola, who directly sampled measurements of the crystallization rates and likelihood of finding small nuclei in the metastable fluid. I provided potentials of mean force and torque, chemical potential calculations, and free energy barriers to nucleation. All authors contributed to the discussion of the results and the writing of the manuscript.

5.1 Simulation Details

Hard particle Monte Carlo (MC) simulations were performed with the HPMC plugin[33] to the HOOMD-blue package[38, 66]. Pressures are given in units of k_bT/V_p, with the particle volume V_p chosen to be unity.

Systems for fluid sampling contained $N = 4096$ identical particles, sufficient to exclude box size effects in similar systems[67]. Independent NPT fluid simulations were initialized as dilute cubic lattices and thermalized by running for a minimum of $80\,000$ MC sweeps, or until the system had equilibrated to a stable density, *i.e.*, a stable box volume. The metastable fluids were then sampled for up to 40 million MC sweeps. Particles in solid-like clusters were identified by applying ten Wolde's clustering method[43].

The cluster size distribution in the equilibrated fluid – this time including all clusters – was measured in $2\,000$–$20\,000$ independent snapshots of the metastable fluid at each pressure. Nucleation probabilities were determined by counting how many times the system crystallized out of a metastable fluid. Measurements of cluster size distributions in the fluid, equations of state, and direct nucleation probabilities were done by Samanthule Nola.

Free energy barriers to nucleation were computed from the probability distribution of observing clusters of a given size using Umbrella Sampling. We used interfacial pinning[50, 49] to determine coexistence pressures that were in turn used to calculate the chemical potential *via* thermodynamic integration[31]. We calculated the potential of mean force and torque (PMFT) to visualize and understand local particle ordering. Detailed descriptions of these methods appear in chapter 2.

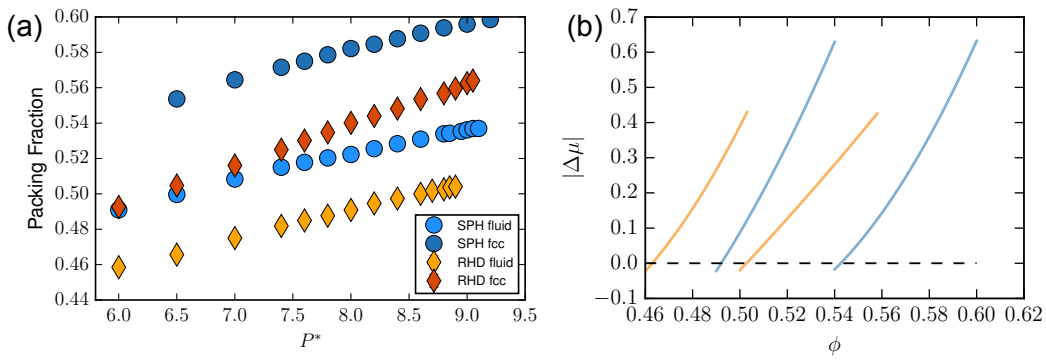

Figure 5.1: *Equations of state.* (a) Fluid and solid equations of state and (b), the chemical potential plotted over pressure. Phase coexistence occurs where the curves intersect the dotted black line. The intersection of the dashed horizontal line at $|\Delta\mu| = 0$ with the data for each shape illustrates the coexistence pressures of fluid and solid phases. The truncation point of the curves at the high-pressure end corresponds approximately to the point at which crystallization can occur spontaneously. From our publication[65].

5.2 Results

The equations of state for both rhombic dodecahedra and spheres are presented in Figure 5.1(a). The fluid of rhombic dodecahedra has a significantly lower packing fraction than the fluid of spheres at any given pressure. This difference arises from shape anisotropy, as rhombic dodecahedra have a greater circumradius than spheres of equal volume, allowing for collisions at greater interparticle distances, which leads to increased pressure of the system at similar densities. The face-centered cubic crystal of rhombic dodecahedra also has a lower packing fraction than the face-centered cubic crystal of spheres over this pressure range, despite the fact that rhombic dodecahedra are space-tessellating in the limit of infinite pressure, while the spheres have a maximum packing fraction of approximately 0.74 in this structure[68, 69]. For both shapes the packing fraction difference between the fluid and crystal increases with pressure. The slope of the equation of state is slightly steeper for rhombic dodecahedra at high pressures, *i.e.*, rhombic dodecahedra have a higher compressibility. This means that rhombic dodecahedra require a smaller increase in pressure for the same increase in packing fraction than spheres do at the same pressure.

In Figure 5.1(b) the chemical potential difference of the fluid and solid states is plotted *vs.* the pressure for systems of spheres and rhombic dodecahedra. They mainly differ in their coexistence pressures $P(\Delta\mu = 0)$. The chemical potential difference ($\Delta\mu$) between the fluid and solid is calculated by integrating the volume per particle between those phases. The curves for each shape appear similar because the difference in density between the fluid

and solid phases are similar. The density jump upon crystallizing does increase for rhombic dodecahedra at higher pressures, see Figure 5.1(a).

The behavior of solid-like clusters in the fluid and during nucleation of the crystalline phase in both systems is illustrated in Figure 5.2, where we plot the probability to find clusters of different sizes at pressures where nucleation is still rare, as well as the crystallization probability, the free energy barriers *vs.* cluster sizes, and the free energy maxima *vs.* both the chemical potential and the pressure.

Probabilities $P_i(X)$ for a particle i to be in a cluster of size X are shown in Figure 5.2(a) for both spheres and rhombic dodecahedra. At low $|\Delta\mu|$, small clusters are more common in fluids of spheres than in fluids of rhombic dodecahedra, but trends change with increasing $|\Delta\mu|$. The apparent lack of small clusters in the fluid of rhombic dodecahedra is likely a consequence of the aforementioned lower packing fraction at small values of $|\Delta\mu|$. There is a crossover point where larger clusters become more prevalent for rhombic dodecahedra than for spheres, when $|\Delta\mu| > 0.25$. A sharp increase in the formation of larger clusters occurs for the fluid of rhombic dodecahedra near $|\Delta\mu| > 0.4$, and slightly further from coexistence rhombic dodecahedra start crystallizing at a measurable rate as seen in Figure 5.2(e). This leads us to consider these larger clusters as pre-critical nuclei, which in turn raises the question of what stabilizes them preferentially in the fluid of rhombic dodecahedra.

Figure 5.2(e) shows a comparison of the crystallization probability in systems of spheres and rhombic dodecahedra. Both shapes begin to crystallize at a measurable rate only after large clusters are seen to form in the fluid. This happens at a significantly higher driving force for spheres than for rhombic dodecahedra. The larger cluster sizes correspond to a density where the emergent directional entropic bonding aligns particles more strongly into local arrangements congruent with the face-centered cubic crystal, which is demonstrated in Figure 5.3. This shows that the formation of larger clusters consistently precedes nucleation.

The free energy barriers for the formation of nuclei of spheres and rhombic dodecahedra are plotted in Figure 5.2(b) and 5.2(c). The difficulty to nucleate can be characterized by the free energy required to form the critical nucleus from a fluid, *i.e.*, the location at which $\beta\Delta G$ is maximal. For comparison, these maxima are shown in Figure 5.2(d) at different driving forces–chemical potential $\Delta\mu$–for both particle shapes. These calculations demonstrate that at given values of the driving force that rhombic dodecahedra nucleate far more easily than spheres. The here-reported nucleation barriers differ from those found in a previous study of polyhedra[31], which were reported to be as low as $\beta G \simeq 5$. At heights this low we should suspect crystallization to almost immediately occur in simulations. In

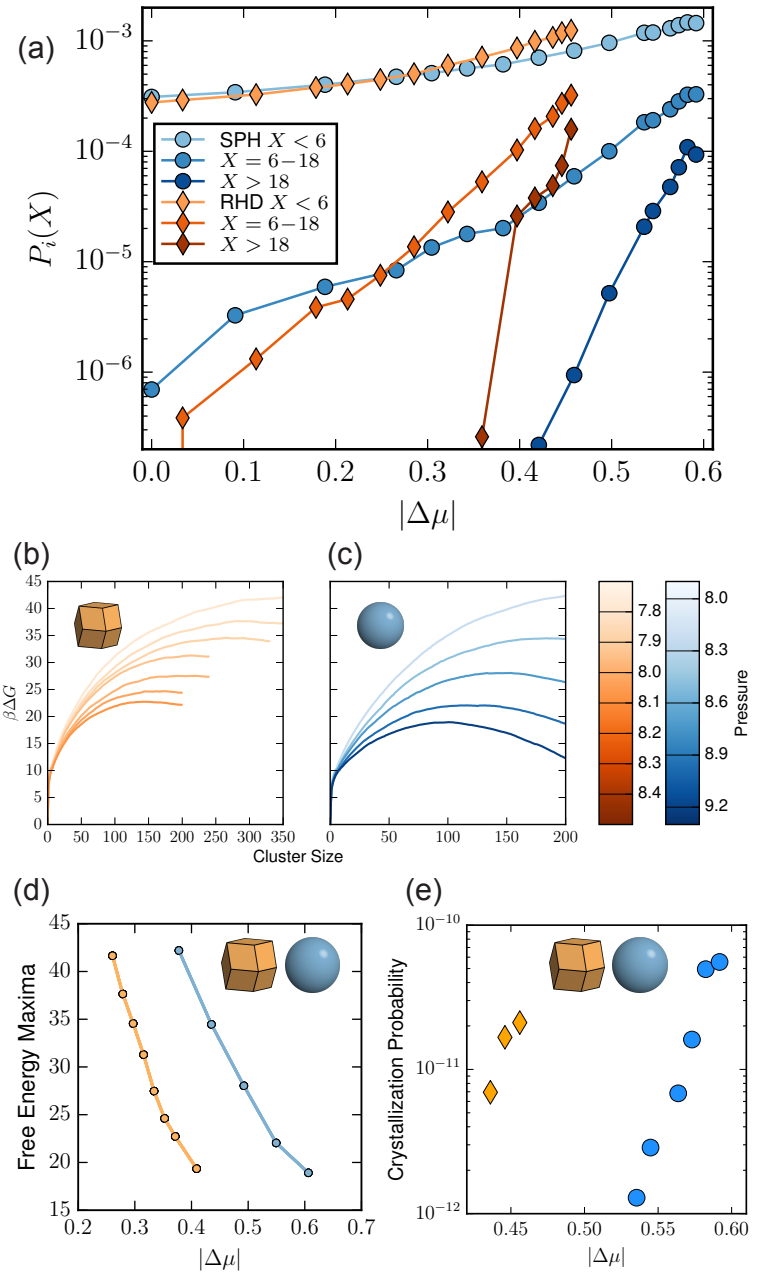

Figure 5.2: *Cluster statistics and free energies.* (a) Cluster size distributions, (b and c) free energy barriers from umbrella sampling, and (d) free energy maxima plotted against the chemical potential from interfacial pinning of hard rhombic dodecahedra and spheres, (e) directly measured nucleation rates. For plots of the free energy barriers, graphs of different colors represent free energy curves at different pressures (exact values are given by horizontal lines and tick labels on the color bars). Adapted from our manuscript[65].

their work[31] the barrier heights were significantly understated, possibly due to tracking only the largest cluster size in the system when small clusters are common. Using the largest cluster is only valid when large clusters are rare[27, 28] and doing so when clusters are frequent leads to a false free energy minimum at the mean small-cluster size in the fluid, and misses the initial steep rise in the free energy barriers. In the small-clusters regime the full cluster probability distribution should be tracked instead.

To better understand why rhombic dodecahedra, when compared to spheres, self-assemble with a significantly lower driving force (*i.e.*, at a lower chemical potential), as well as having larger local cluster size distributions in the fluid, we calculate the potential of mean force and torque (PMFT) of particle-neighbor bonds. The PMFTs of the system of spheres, as shown in Figure 5.3(a) and 5.3(b), are expectedly isotropic and correspond to the well-known radial distribution functions for hard spheres. To illustrate the PMFT of the system of rhombic dodecahedra, cross-sections are performed through the center of the particle perpendicular to the 4-fold and the 3-fold symmetry axes (see Figure 5.3(c) and 5.3(d)). The crystal PMFTs for both shapes exhibit regions of high free energy (shown in red in Figure 5.3) corresponding to interstitial positions in the face-centered cubic structure. In the fluid, the boundaries between the first and second coordination shell are poorly defined, whereas in the crystal the interstitial positions are effectively 'forbidden'.

The anisotropic shape of the rhombic dodecahedron causes face-centered cubic-like pairwise local arrangements in the first coordination shell with respect to particle orientation, even in the disordered fluid phase. In both the fluid and solid, we observe that rotations of a rhombic dodecahedron around a 3-fold axis are more entropically favorable than rotations about the 4-fold. This corresponds to the previously reported fact that the 4-fold vertices of rhombic dodecahedra are more restrictive to rotational motion than the 3-fold ones and thus their truncation leads to an greater improvement of the assembly-behavior into the face-centered cubic crystal structure[70].

In Figure 5.3(g) and 5.3(h), we show a three-dimensional representation of the PMFTs in the fluid and crystalline systems of rhombic dodecahedra. The lower hemisphere in each image illustrates the anisotropic PMFT around the polyhedron; additionally, isosurfaces at a value of $\beta F = 0.5$ are superimposed. While the first coordination shells have a similar appearance in both the fluid and the solid and therefore have similar local order, the most entropically favorable positions are much more diffuse, *i.e.*, the low energy basins of the PMFT are broader for the fluid and narrower for the crystal of rhombic dodecahedra.

Directional entropic forces favoring face-to-face alignment of the rhombic dodecahedra cause the local structure of the fluid to resemble that of the crystal. This makes fluid and solid more similar and increases the likelihood of particles in the fluid to have locally

face-centered-cubic motifs. This shape-anisotropy-driven ordering is what we believe stabilizes clusters of rhombic dodecahedra, which more easily form from the fluid at lower supersaturations, and which lead to lower nucleation barriers as compared to spheres.

5.3 Concluding Remarks

With increasing pressures the probability of finding rhombic dodecahedra in small clusters increases more sharply than for spheres and eventually the two probabilities cross. This is a direct consequence of entropic bonding – the preference of faceted particles to arrange themselves with face-to-face contacts to maximize the free volume in the system[23].

Calculation of the potentials of mean force and torque showed that the local particle environments in the dense fluids of rhombic dodecahedra are commensurate with the local bond-orientational order of the face-centered cubic crystal, arising from the directional entropic forces tending to position facets in a face-to-face alignment. We believe that this pre-existing local order is what increasingly stabilizes the crystal nuclei of rhombic dodecahedra as compared to spheres. These emergent local entropic interactions are stabilize the pathway from a supersaturated fluid to an ordered crystal. By increasingly positioning neighboring particles in motifs commensurate with the crystal structure, the need for rearrangement decreases, leading to the much lower free-energy pathways to crystallization at given supersaturations shown in Figure 5.2(b) – 5.2(d) and the larger fluid-phase cluster fluctuations given in Figure 5.2(a).

Previously, it had been shown that self-assembling fluids and crystals of polyhedra exhibit almost identical coordination numbers[19]. The same study showed that measures of shape anisotropy – in particular the isoperimetric quotient – and dense fluid coordination numbers could be used to predict the expected equilibrium crystal phases. Here we demonstrated that anisotropic particles nucleate with lower driving forces than do isotropic spheres. This local ordering was suggested by Thapar[31], but shown directly here in the PMFTs. We agree that the polyhedral facets for this shape is integral to easing the nucleation pathways as they lead particle coordination shells in the fluid to adopt motifs similar to the crystal. This may also be the case for the truncated octahedra and cubes that Thapar studied.

Further work will analyze the quantitative influence of specific facets by successively altering polyhedral shapes to investigate the trend in nucleation behavior[71] which is the subject of chapter 6. In order to explore another aspect of this phenomenon, further studies will compare different symmetries and kinds of faceting, and therefore investigate the differing tendencies of polyhedra to nucleate in the same face-centered cubic crystal

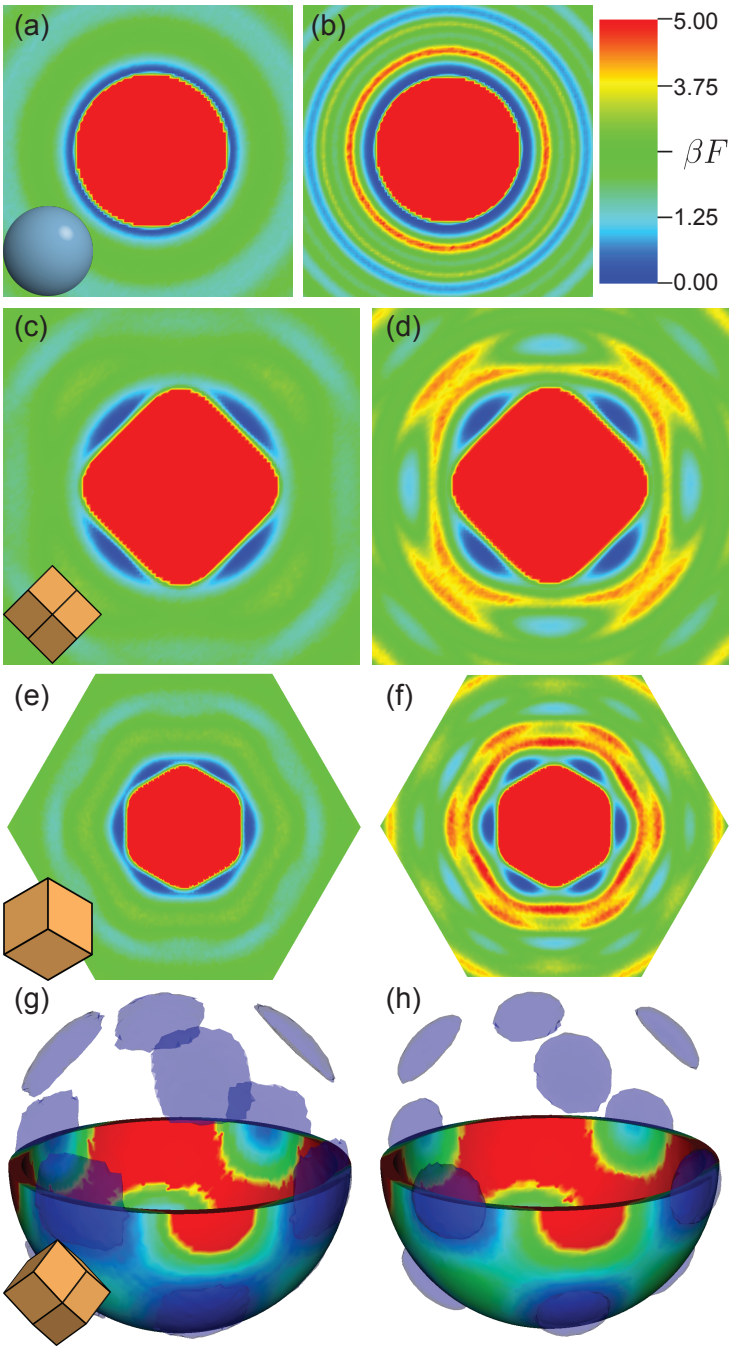

Figure 5.3: *Potentials of mean force and torque.* For (a) – (b) spheres and (c) – (h) rhombic dodecahedra, for fluid ((a), (c), (e), and (g)) and crystalline systems ((b), (d), (f), and (h)). All maps use the same coloring scheme; energies are shifted so that the deepest minimum corresponds to $\beta F = 0$. The top and middle figures represent cuts through the particle centers (in the case of the rhombic dodecahedron: perpendicular to the 4-fold and 3-fold symmetry axes, respectively). The bottom figures show the PMFTs for a fluid and crystal of rhombic dodecahedra, intersecting with a thin hemisphere corresponding to the first neighbor shell. Additionally, transparent isosurfaces are shown at an energy of $\beta F = 0.5$. The insets depicting the particle illustrate the orientation of the respective set of PMFTs. From our publication[65].

structure[72]. We expect that building blocks chosen such that the entropic forces that will be present in the fluid possess structural motifs similar to the solid will stabilize the pathway to crystallization.

CHAPTER 6

Investigating the Role of Polyhedral Faceting on the Nucleation of Face-centered Cubic Crystals from Fluids of Hard Polyhedra

Continuing the investigations in the prior chapter, we now turn to understand the role of polyhedral faceting on a continuous family of polyhedra. Rather than disparate shapes, this allows us to see how perturbations to a given shape alter the nucleation behavior. In this study, adapted from our publication "Nucleation Free Energies of FCC-assembling Polyhedra", Richmond S. Newman, Julia Dshemuchadse, and Sharon C. Glotzer, *Preprint*[71], we compare several shapes that form rotator face-centered cubic crystals. Simulations and calculations were performed by Richmond Newman, under the supervision of the other authors.

Dense systems of hard polyhedra have previously been studied *in silico* and shown to self-assemble into a wide variety of equilibrium structures[19, 59]. Moreover these simulations have demonstrated that hard particle models can often accurately predict equilibrium self-assembled structures from a diverse sets colloidal nanopolyhedra[14]. Recent work on the nucleation of hard polyhedra[31] suggested localized orientational order allowed polyhedra to self-assemble more easily into rotator crystals than hard spheres. The authors studied rhombic dodecahedra, truncated octahedra, and cuboctahedra and suggested that the local ordering provided by faceting was beneficial to nucleation. As these shapes are unrelated it is difficult to isolate the effects of the polyhedral faceting. In contrast, here we perform a detailed study on a family of polyhedra (Figure 6.1) ranging continuously between a rhombic dodecahedron to a rhombicuboctahedron. This family of polyhedra is chosen because all members assemble into the cubic close packing, and the changes to the faceting preserve cubic symmetry. The rhombic dodecahedron is also the Voronoi polyhedron for the cubic close packing, that is, it fills space in this arrangement. This particular family of shapes is also experimentally realizable as syntheses exist for crystalline

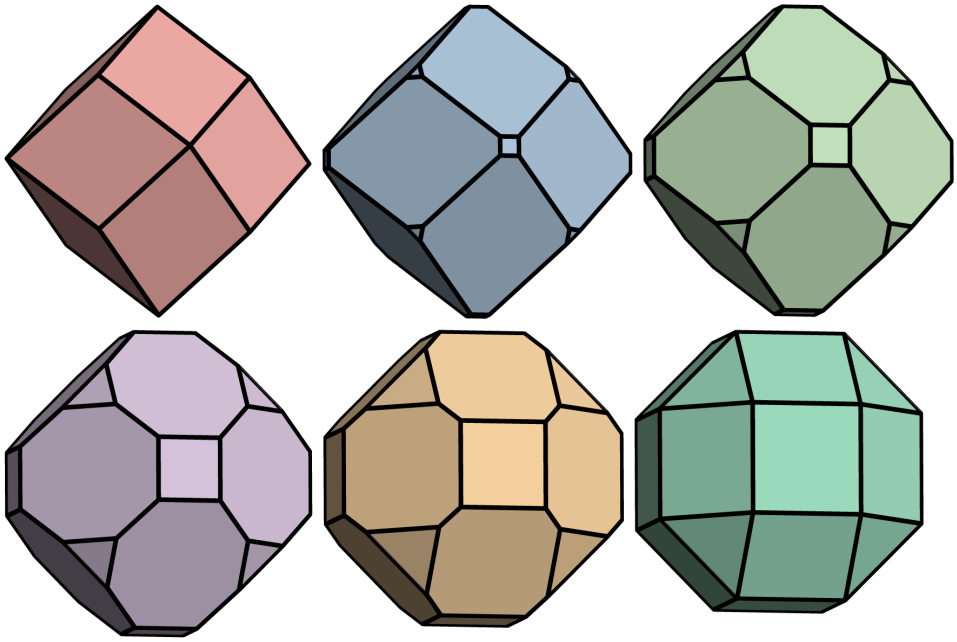

Figure 6.1: *Studied Polyhedra.* Rhombic dodecahedron to rhombicuboctahedron shape family. From our publication[71].

gold rhombic dodecahedra exposing twelve (110) facets, and these building blocks can be additionally etched to form rhombicuboctahedra[15]. In particular, we are interested in observing how changing the polyhedra faceting and undermining the tendencies toward face-to-face alignment affects the crystallization process.

To compare different face-centered cubic-forming shapes, we define a continuous truncation parameter t that converts from a rhombic dodecahedra (at $t = 0$) to a rhombicuboctahedron (at $t = 1$). These polyhedra are shown in Figure 6.1. This truncation pathway preserves the cubic symmetry of the polyhedra, but as the truncation increases, additional facets incompatible with the the face-centered cubic crystal appear, and the particle loses its space-filling characteristics. All of these shapes self-assemble into rotator face-centered cubic crystals. These particles can also be viewed as a subset of the 432-family of shapes whose densest packings were described by Chen *et al.*[73]. In their notation, our truncation between the rhombic dodecahedron and rhombicuboctahedron follows the parameters $a = 2 - (2 - \sqrt{2})t$, $b = 2$, $c = 3 - (\sqrt{2} - 1)t$. These parameters describe the distance of sets of planes with different symmetry, with decreasing a corresponding to a set of planes perpendicular to the 4-fold axes moving inwards (truncating the 4-fold vertices of the rhombic dodecahedra), and decreasing c corresponds to planes perpendicular to the 3-fold axes moving inwards, (truncating the 3-fold vertices).

6.1 Simulation Details

Simulations were performed with hard particle Monte Carlo using HOOMD-blue with the HPMC (High Performance Monte Carlo) package[38, 33]. System sizes of $N = 3375$ ($= 15^3$) particles were used for the NPT umbrella sampling simulations, whereas $N = 2744$ were used for NPT interfacial pinning simulations to determine coexistence pressures. Measurements of the equation of state were performed in the NPT ensemble using 3375 particles and integrated to obtain chemical potentials.

6.2 Results

We study how the crystallization behavior of polyhedra is affected by their faceting using the polyhedra family shown in Figure 6.1. We wish to compare the free energy barriers to nucleation as a function of supersaturation (driving force, $|\Delta\mu|$), which first requires us to compute the equations of state for each shape which we show in Figure 6.2. At given values of pressure we see a tendency for the more spherical shapes to have higher density, but none of the polyhedra in this family are sufficiently spherical to reach the higher densities observed for spheres. It can also be seen that the crystal of rhombic dodecahedra is slightly more compressible than the other shapes at higher pressures or packing fractions; this is because this particular shape is able to fill space on a face-centered cubic crystal.

As discussed in equation 1.1, the thermodynamic driving force for nucleation in these systems is the chemical potential difference between the solid and fluid. Chemical potentials for a given shape and pressure can be calculated by integrating the equations of state for the fluid and solid from the coexistence pressures,

$$\Delta\mu = \int_{P_{coex}}^{P} \frac{V_{cry}}{N} - \frac{V_{flu}}{N} dP'. \tag{6.1}$$

The coexistence pressures P_{coex} are obtained using the interfacial pinning method described in section 2.7. The results of these integrations are shown in Figure 6.3, where we can see that at any given pressure, the more spherical shapes have notably larger driving forces. The majority of the difference in driving force corresponds to a drift towards lower coexistence pressures for larger truncations (less anisotropic polyhedra). Curiously, hard spheres have an intermediate coexistence pressure as compared to the family of polyhedra. The chemical potential curves for all particles have similar shapes, and indeed are mostly 'linear' because the integrated density difference between the fluid and solid in equation 6.1 remains fairly constant and similar for each shape over the modest pressure range where the

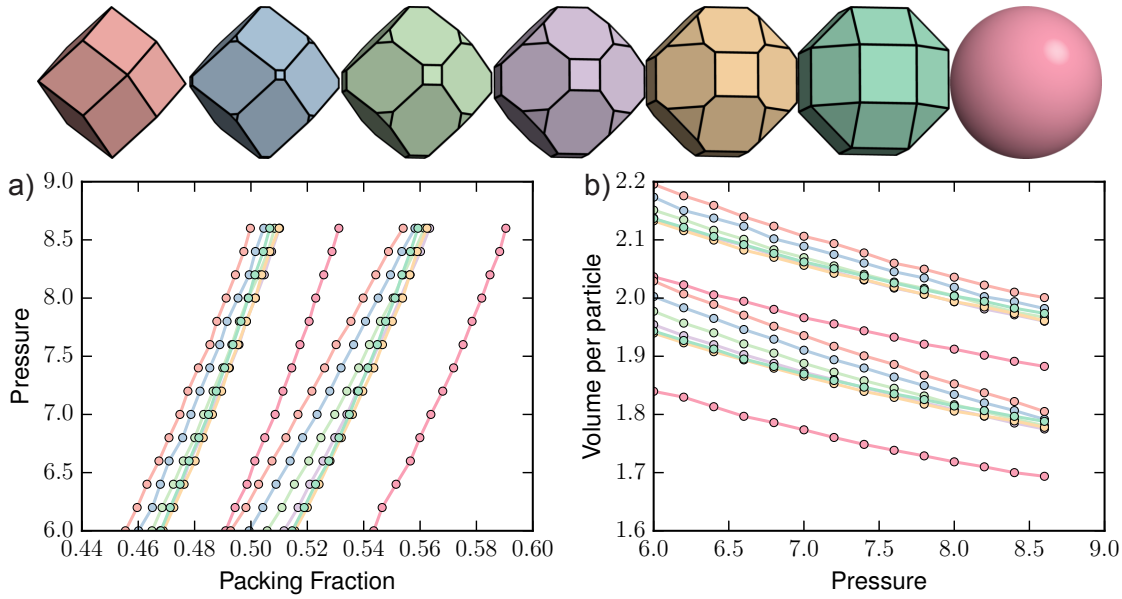

Figure 6.2: *Shape family equations of state*. (a) Equations of state for the six polyhedra and spheres. Particles and curves are colored correspondingly. The left set of curves correspond to the less dense metastable fluids, and the right set of curves to the face-centered cubic crystals. (b) Equations of state expressed as volume per particle available to the system. From our publication[71].

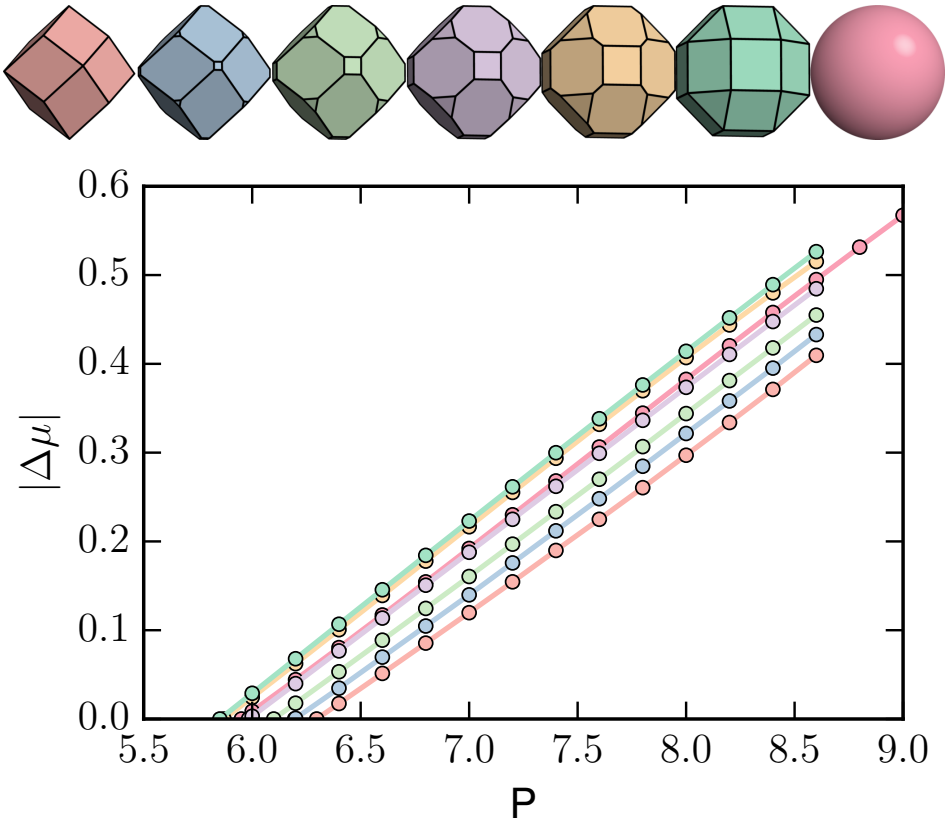

Figure 6.3: *Chemical potentials*. Computed chemical potentials $\Delta\mu$ *vs*. pressure P resulting from integrating the equations of state for each polyhedra. Figure reproduced from publication[71].

fluid is metastable and measurable. The differences integrated are shown in Figure 6.2(b).

Using umbrella sampling (discussed in section 2.5), we are able to compute free energy barriers for this family of vertex-truncated rhombic dodecahedra. These barriers are shown in Figure 6.4. These results are computed from NPT simulations and barriers are shown for various pressures. Each curve represents the average of ten replicate runs. At a given pressure it would seem rhombic dodecahedra have the highest barriers, but this is because the various shapes need to be compared at the same magnitude of driving force $\Delta\mu$. With the chemical potentials from thermodynamic integration we can show the barrier heights as a function of driving force (Figure 6.5) to compare the different building blocks at constant quench depths. In doing so, it is here that we see the effect of the particle shape on the difficulty of the nucleation process: truncations of the rhombic dodecahedra produce large increases of the barrier heights at a given driving force. As the likelihood of nucleation is proportional to the exponential of this free energy, this suggests that the building block

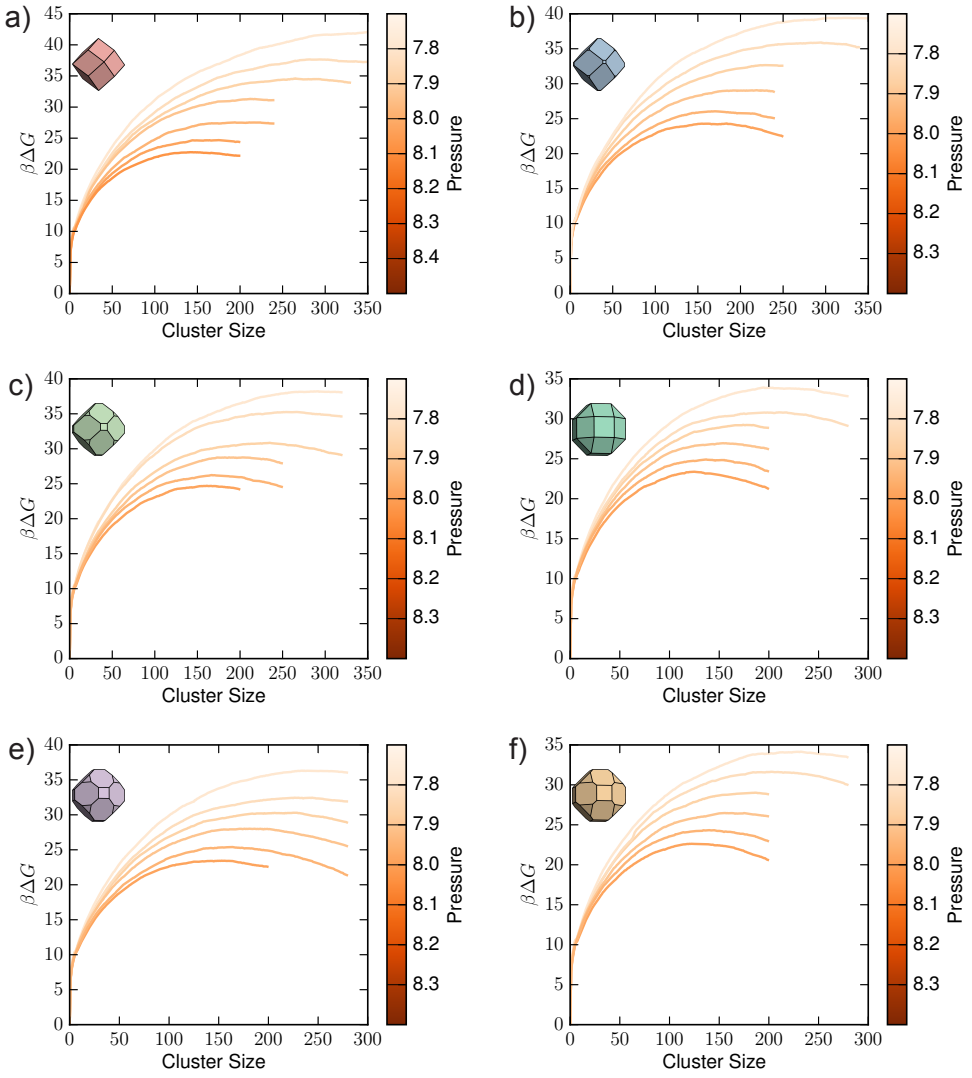

Figure 6.4: *Free energy barriers*. Umbrella-sampled free energy barriers to nucleation for the polyhedra family. From our publication[71].

geometry is critical for homogeneous nucleation.

We also make estimates of the critical nucleus sizes for each shape, or the cluster size which maximizes βG. While the measurements of cluster sizes are noisy because the sampled free energy barriers are broad near the peak, the trends are still visible. These values of N should be considered estimates: the exact cluster sizes are sensitive to the given cutoff parameters to the order parameter distinguishing solid crystal from fluid; however, the height of the barrier was shown to be robust, as the tendency for a given nucleus to grow or shrink in simulation is not dependent precisely on the size identifed by our choice of order parameter[44]. All systems presented here were analyzed using the same cutoff parameters for the order parameter. We can see in Figure 6.6(b) that the rhombic dodecahedra have slightly smaller critical nuclei at the same driving force, and that the polyhedra seem to have more similar free energy maxima as a function of critical nucleus size.

In addition to studying the process of nucleation, we also characterized the local orientational ordering in the fluid and solid phases. We computed the potentials of mean force and torque between a given particle and neighboring particles[22, 23]. This procedure quantifies the entropic forces between pairs of particles leading them to align more preferentially in a face-to-face manner in both the disordered fluid, and particularly so in the solid phases. In doing so we can see in Figure 6.7 how the truncation of the rhombic dodecahedron to the rhombicuboctahedron takes away from the preferred arrangement. In the 4-fold cross sections of the PMFT in the fluid phase we initially see isolated energy wells for the rhombic dodecahedra, which become significantly more isotropic as we truncate toward the rhombicuboctahedra. This suggests that the local environment becomes more free to rotate around this axis, corresponding to less and less coupling of a particle with its first coordination shell. The effects of truncation are also visible in the in the three-dimensional isosurface plots, where the local symmetry in the fluid is initially commensurate with the face-centered cubic structure due to the rhombic dodecahedra facets, but these minima are undermined with increasing truncation as the original facets shrink and new entropic minima are introduced for the additional facets that were formerly the three-fold and four-fold vertices. These new entropic minima become quite prevalent at the highest truncations ($t = 0.8, t = 1.0$). The PMFTs of the crystal phase show that there are significant geometrically forbidden interstitial regions around the particles as the first and second crystal neighbor shells exclude particles. The orientational penalities enforced by local crystalline order diminish with increasing truncations. The PMFTs are much more isotropic for the rhombicuboctahedra, which are almost free to rotate despite being a crystalline phase.

The penalties for particles being in the interstitial regions suggest the positional order corresponding to a crystal, but the lack of deep minima in the first coordination shell sug-

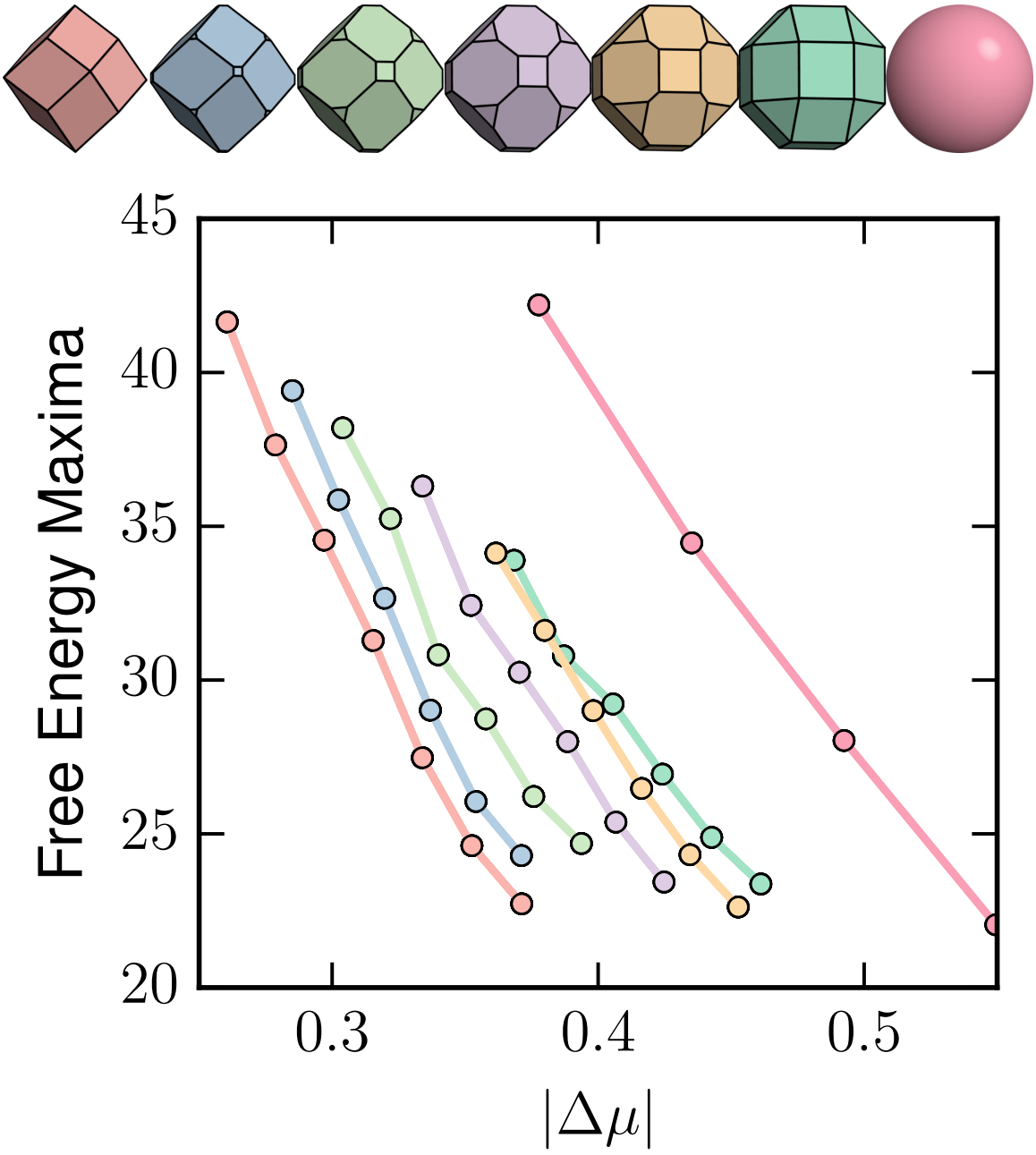

Figure 6.5: *Free Energy Penalties to Nucleation.* Free energy barrier maxima from the umbrella-sampled NPT simulations plotted against the driving force (chemical potential) for different polyhedra. From our publication[71].

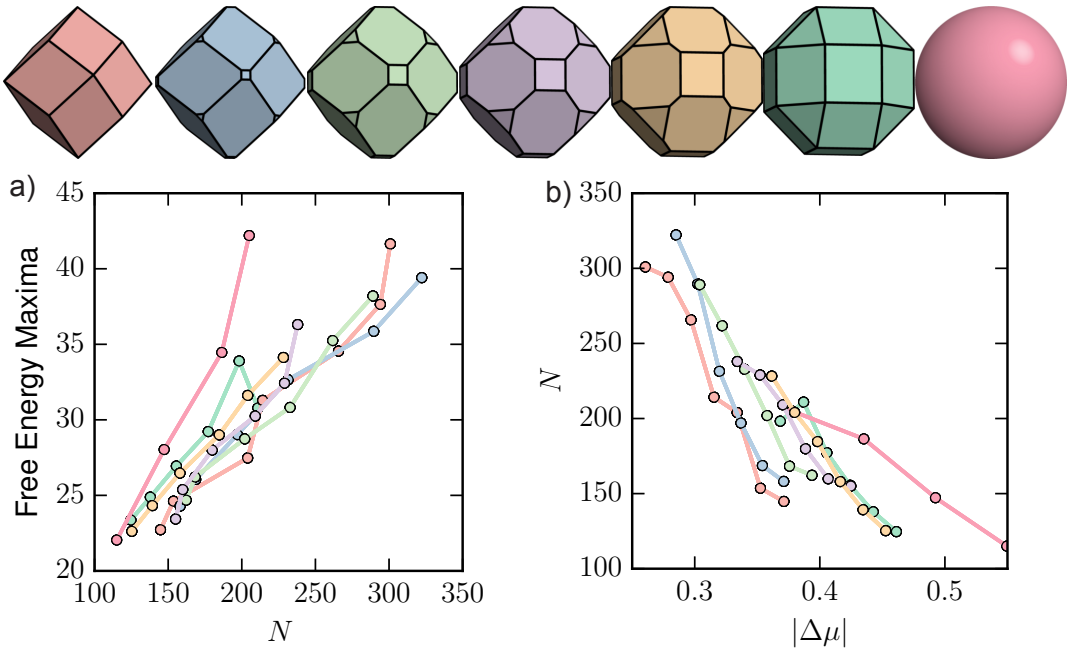

Figure 6.6: *Critical nuclei*. (a) Free energy maxima plotted against critical nucleus size. (b) Critical nucleus size *vs.* crystallization driving force. From our publication[71].

gests that the orientation of the reference particle and its coordination shell are very weakly bound: misorientations of rhombicuboctahedra and the face-centered cubic coordination shell carry energetic penalties less than $\beta F = 0.4$ as seen by the broader isosurfaces in Figure 6.7(e). Although the untruncated shape, the rhombic dodecahedron, already forms a crystal with orientational disorder, the level of orientational disorder rises measurably with increased truncation. The visible increase of the orientational entropy should further stabilize crystal phase in the heavily truncated shapes; however, this is not sufficient to ease the crystallization pathway from the fluid.

6.3 Concluding Remarks

We have conducted the first study of the nucleation barriers of a family of hard polyhedra to directly show how shape affects the crystallization pathway. This builds upon the work in the prior publication on rhombic dodecahedra and spheres[65], and on the early work on hard polyhedra by Thapar[31]. In these studies, unrelated shapes were compared, but here, by controlling for particle shape and symmetry we have shown directly how shape influences nucleation: that *via* truncations of rhombic dodecahedra, the face-centered cubic

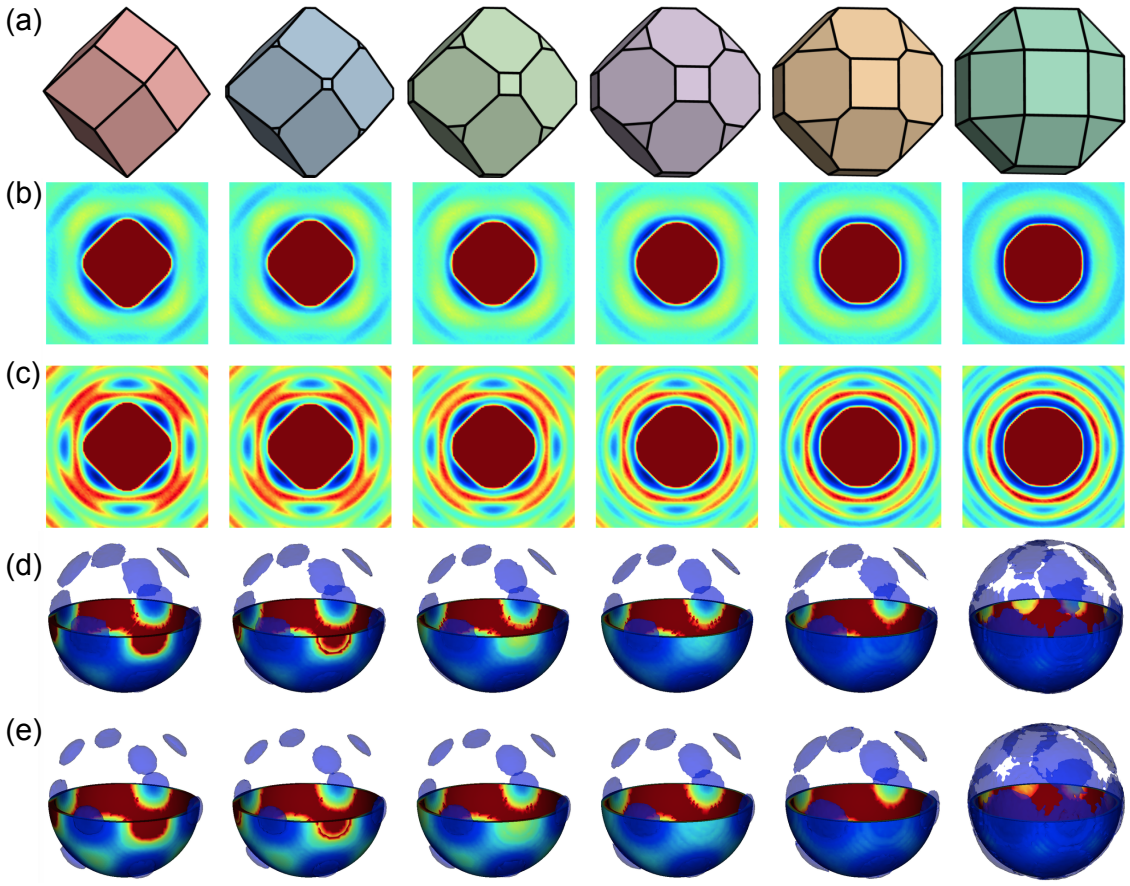

Figure 6.7: *Potentials of mean force and torque*. (a) Family of polyhedra. (b,c) Cross sections through the four-fold axis are shown for the (b) fluid and (c) solid phases. (d,e) Three-dimensional views of the PMFT intersecting a thin hemisphere in the first coordination shell, with isocontours drawn at $\beta F = 0.4$ from the deepest minima for the (d) fluid and (e) solid phases. From our publication[71].

Voronoi particle, increase the free energy barriers to crystallization at equivalent driving forces. This confirms the ideas in prior work[31, 65] that crystallization in polyhedra are stabilized by the directional entropic forces between particles that encourage face-to-face alignment in the fluid. Here we have characterized these locally aligned motifs using potentials of mean force and torque, and for the family of shapes studied that the least truncated shapes arrange into local motifs in the fluid phase that are more likely commensurate with the final crystal structure. The additional facets formed as we truncate towards the rhombicuboctahedron add a level of competition that hinder nucleation until higher degrees of supersaturation overcomes the lack of local ordering. Ideal building blocks for crystallization like the rhombic dodecahedron stabilize the transition state to nucleation by having fluid local structures similar to those of the crystal.

CHAPTER 7

Conclusions and Future Outlook

7.1 Summary

In this work we studied the crystallization of systems of polyhedra. These studies demonstrated the ability of simulation to help understand experimental systems as well as the crucial role of building block geometry.

In chapter 3 we demonstrated the use of simulations in understanding the self-assembly of lithium yttrium fluoride nanobipyramids. There we studied several aspect ratios of bipyramids, as well as a model of different truncations and surface interactions. We were able to predict three experimental bipyramid motifs using a model of truncation, and showed that interacting particles form an interesting antiparallel striped motif.

In the second described study, in chapter 4, we studied the shape-dependent assembly of rhombic dodecahedra, octahedra, cubes, and spheres. Computer simulations were used to try to better understand how the experiments assembled, and enabled the investigation of the behavior unique to each shape. Rhombic dodecahedra possess rotational disorder visible in both simulations and experiments. Cubes possess positional disorder due to the presence of shear planes. Octahedra have many potential candidate dense packings, each with different maximal properties: densest packing, entropic shearing modes, or contact area. Spheres suffer from many stacking faults, which may limit domain size annealing, and difficulties arise from the challenge in synthesizing ideal hard spheres.

For the third study, described in chapter 5, we looked at the crystallization of rhombic dodecahedra and spheres in detail. Measurements of cluster size fluctuations in the fluid, crystallization probabilities, and free energy barriers demonstrated that rhombic dodecahedra crystallize at much lower driving forces than those required to crystallize spheres. Potentials of mean force and torque were used to understand how local ordering present in the fluid makes these nucleation events more probable due to similar local ordering in the fluid and solid arising from directional entropic forces.

Finally, in chapter 6 we examined the nucleation free energy barriers and thermodynamics in a system of face-centered-cubic forming polyhedra from a continuous family of shapes from a rhombic dodecahedron to a rhombicuboctahedron. As predicted, the reduction of directional entropic forces favoring the face-centered cubic crystal as one truncates the rhombic dodecahedra led to increased free energy barriers as a function of supersaturation $|\Delta\mu|$, illustrating how shape can influence crystallization of hard polyhedra.

7.2 Future Outlook

Future studies will be able to carry out larger and larger simulations, not only due to the continuing rise in the performance of computers, but also increasingly due to shared software development. As the level of complexity of simulations continues to rise, the reuse and sharing of code will lead to more detailed studies to be undertaken. Many of the techniques, methods, and code used in this work will be open-sourced in the near future[42], making the methods readily available to scientists in the near future. Many months of time were invested in reimplementing these methods so this work could be carried out. Having implementations of these analysis methods and tools widely available should enable much faster setup and analysis of simulations, and I hope will reduce the difficulty of studying nucleation events in simulations by future researchers.

In the later chapters we took first steps towards understanding how polyhedral faceting was instrumental for stabilizing free energy pathways to nucleation. In this we selected a family of polyhedra that all formed face-centered cubic crystals, and all possessed cubic symmetry. This allowed us to isolate the effects of the faceting and show that the commensurate local structures templated by the polyhedral geometry in the fluid eased the difficulty of nucleating the crystal. However, in general, there are many polyhedra[19] that nucleate and form face-centered cubic crystals, and many of these polyhedra do not have the same symmetry. Entropic forces in the fluid tend to align polyhedra in a face-to-face manner, which suggests that many of these polyhedra will have local ordering with different symmetries, such as being locally icosahedral or hexagonally closed packed. Nucleation in these systems must overcome their local fluid structure and particles have to rearrange significantly to crystallize, which can be studied using the same tools described here.

The methods used in this dissertation may also be used to investigate the free energy barriers of polyhedra to crystallize into different crystal structures. Future studies should be able to use the techniques described here to study the formation of much more complicated crystal structures in both hard polyhedra, and in molecular dynamics simulations. For example, in Figure 2.1 the solid-liquid order parameter was able to identify the formation

of crystalline order in a potential-based dodecagonal quasicrystal. The ability to track the formation of these complex phases will allow for more in-depth study and characterization of these systems, and answer questions about how particles are able to locally rearrange and attach to much more complex crystal structures than the face-centered cubic crystals studied here.

Advances in simulation methods also now make it possible to simulate 'soft' polyhedra using molecular dynamics[74]. The discrete element method (DEM) allows for simulating polyhedra with a repulsive Weeks-Chander-Anderson pair potential that is summed over the faces, edges, and vertices. Studying nucleation with this model loses some of the benefits of being hard, namely, having exact density, faceting, and edges. These behaviors are lost in DEM, however, it gains a distinct advantage in that molecular dynamics simulations innately have timescales arising from integrating Newton's equations of motion. The use of this method will allow future studies to study nucleation rates and growth rates directly, instead of the thermodynamic approach taken here of quantifying the hard shape free energy barrier heights.

APPENDIX A

Mapping Monte Carlo Cycles onto Experimental Time

The relationship between the simulation and experimental time scales was estimated by comparing the mean square displacement measured from simulations in the fluid phase to the Brownian diffusion constants of the nanocrystals in water. This comparison is not exact, but sufficient to provide an order-of-magnitude estimation. From simulations we could measure the mean squared displacement by calculating

$$\langle \left(\delta r(t)^2\right) \rangle = \frac{1}{N} \sum_{i=1}^{N} \left(r(t) - r(0)\right)^2 . \tag{A.1}$$

The mean square displacement was used to estimate the diffusion coefficient from simulations as

$$D = \frac{\langle (\delta r(t)^2) \rangle}{6t}. \tag{A.2}$$

In addition, the diffusion coefficient for a nanoparticle was estimated using Stokes law:

$$D = \frac{k_b T}{6\pi\eta\sigma}. \tag{A.3}$$

Using the viscosity of water $\eta = 8.92 \cdot 10^{-4}$ Pa·s at temperature $T = 298$K, we could calculate that a spherical particle with diameter $\sigma = 40$ nm had a free diffusion constant of $D \simeq 4 \cdot 10^{-14}$m^2/s , or expressed in terms of particle size, $D \simeq 25\sigma^2$/s. Dense solutions have considerable caging effects, which reduced NC diffusion by a factor of 100 compared to the value predicted by Stokes law at densities near $\phi = 0.535$[75]. We can measure the diffusion rate of hard spheres in simulations at $\phi = 0.54$ and get a diffusion coefficient of $D_{sim} \simeq 2.6 \cdot 10^{-5}\sigma^2/t$, where t denotes a Monte Carlo cycle. Using the factor of 100 correction for the diffusion of a dense system[75] as compared to the bulk, we can estimate that one second of real time corresponds to approximately 10^4 Monte Carlo cycles. The equilibrium density simulations in chapter 4 ran for $5 \cdot 10^7$ Monte Carlo cycles, which

corresponds to about 90 minutes of experimental time. The simulations of heterogeneous nucleation in that study involved about 3 million Monte Carlo cycles, which correspond closer to five minutes, although order near the wall appeared sufficiently early on in the simulations to correspond to a point in time well within the first minute. We expect that the effect of anisotropy on this mapping is likely not going to alter by several orders of magnitude, such that the early ordering near the wall should occur quickly once the particles sediment to sufficient density, so that the local increase in density is in quasistatic equilibrium.

BIBLIOGRAPHY

[1] Kabashin, A. V., Evans, P., Pastkovsky, S., Hendren, W., Wurtz, G. A., Atkinson, R., Pollard, R., Podolskiy, V. A., and Zayats, A. V., "Plasmonic nanorod metamaterials for biosensing," *Nature Materials*, Vol. 8, No. 11, Oct 2009, pp. 867–871.

[2] Yang, S., Ni, X., Yin, X., Kante, B., Zhang, P., Zhu, J., Wang, Y., and Zhang, X., "Feedback-driven self-assembly of symmetry-breaking optical metamaterials in solution," *Nature Nanotech*, Vol. 9, No. 12, Nov 2014, pp. 1002–1006.

[3] Ross, M. B., Ku, J. C., Vaccarezza, V. M., Schatz, G. C., and Mirkin, C. A., "Nanoscale form dictates mesoscale function in plasmonic DNA–nanoparticle superlattices," *Nature Nanotech*, Vol. 10, No. 5, Apr 2015, pp. 453–458.

[4] Alvarez-Puebla, R. A., Agarwal, A., Manna, P., Khanal, B. P., Aldeanueva-Potel, P., Carbo-Argibay, E., Pazos-Perez, N., Vigderman, L., Zubarev, E. R., Kotov, N. A., and Liz-Marzan, L. M., "Gold nanorods 3D-supercrystals as surface enhanced Raman scattering spectroscopy substrates for the rapid detection of scrambled prions," *Proceedings of the National Academy of Sciences*, Vol. 108, No. 20, May 2011, pp. 8157–8161.

[5] Tao, A. R., Ceperley, D. P., Sinsermsuksakul, P., Neureuther, A. R., and Yang, P., "Self-Organized Silver Nanoparticles for Three-Dimensional Plasmonic Crystals," *Nano Letters*, Vol. 8, No. 11, Nov 2008, pp. 4033–4038.

[6] Tao, A., Sinsermsuksakul, P., and Yang, P., "Tunable plasmonic lattices of silver nanocrystals," *Nature Nanotech*, Vol. 2, No. 7, Jul 2007, pp. 435–440.

[7] Nie, Z., Petukhova, A., and Kumacheva, E., "Properties and emerging applications of self-assembled structures made from inorganic nanoparticles," *Nature Nanotech*, Vol. 5, No. 1, Dec 2009, pp. 15–25.

[8] Yamada, Y., Tsung, C.-K., Huang, W., Huo, Z., Habas, S. E., Soejima, T., Aliaga, C. E., Somorjai, G. A., and Yang, P., "Nanocrystal bilayer for tandem catalysis," *Nature Chemistry*, Vol. 3, No. 5, Apr 2011, pp. 372–376.

[9] Zhu, Z., Meng, H., Liu, W., Liu, X., Gong, J., Qiu, X., Jiang, L., Wang, D., and Tang, Z., "Superstructures and SERS Properties of Gold Nanocrystals with Different Shapes," *Angewandte Chemie*, Vol. 123, No. 7, Jan 2011, pp. 1631–1634.

[10] Kuzyk, A., Schreiber, R., Fan, Z., Pardatscher, G., Roller, E.-M., Högele, A., Simmel, F. C., Govorov, A. O., and Liedl, T., "DNA-based self-assembly of chiral plasmonic nanostructures with tailored optical response," *Nature*, Vol. 483, No. 7389, Mar 2012, pp. 311–314.

[11] Kalsin, A. M., Fialkowski, M., Paszewski, M., Smoukov, S. K., Bishop, K. J., and Grzybowski, B. A., "Electrostatic self-assembly of binary nanoparticle crystals with a diamond-like lattice," *Science*, Vol. 312, No. 5772, 2006, pp. 420–424.

[12] Talapin, D. V., Shevchenko, E. V., Bodnarchuk, M. I., Ye, X., Chen, J., and Murray, C. B., "Quasicrystalline order in self-assembled binary nanoparticle superlattices," *Nature*, Vol. 461, No. 7266, Oct 2009, pp. 964–967.

[13] Wang, T., Zhuang, J., Lynch, J., Chen, O., Wang, Z., Wang, X., LaMontagne, D., Wu, H., Wang, Z., and Cao, Y. C., "Self-Assembled Colloidal Superparticles from Nanorods," *Science*, Vol. 338, No. 6105, Oct 2012, pp. 358–363.

[14] Henzie, J., Grnwald, M., Widmer-Cooper, A., Geissler, P. L., and Yang, P., "Self-assembly of uniform polyhedral silver nanocrystals into densest packings and exotic superlattices," *Nature Materials*, Vol. 11, No. 2, Nov 2011, pp. 131–137.

[15] Kim, D. Y., Im, S. H., Park, O. O., and Lim, Y. T., "Evolution of gold nanoparticles through Catalan, Archimedean, and Platonic solids," *Crystal Engineering Communications*, Vol. 12, No. 1, 2010, pp. 116.

[16] Metropolis, N., Rosenbluth, A. W., Rosenbluth, M. N., Teller, A. H., and Teller, E., "Equation of State Calculations by Fast Computing Machines," *The Journal of Chemical Physics*, Vol. 21, No. 6, 1953, pp. 1087–1092.

[17] Alder, B. J. and Wainwright, T. E., "Phase Transition for a Hard Sphere System," *The Journal of Chemical Physics*, Vol. 27, No. 5, 1957, pp. 1208.

[18] Wood, W. W. and Jacobson, J. D., "Preliminary Results from a Recalculation of the Monte Carlo Equation of State of Hard Spheres," *The Journal of Chemical Physics*, Vol. 27, No. 5, 1957, pp. 1207.

[19] Damasceno, P. F., Engel, M., and Glotzer, S. C., "Predictive Self-Assembly of Polyhedra into Complex Structures," *Science*, Vol. 337, No. 6093, Jul 2012, pp. 453–457.

[20] Haji-Akbari, A., Engel, M., Keys, A. S., Zheng, X., Petschek, R. G., Palffy-Muhoray, P., and Glotzer, S. C., "Disordered, quasicrystalline and crystalline phases of densely packed tetrahedra," *Nature*, Vol. 462, No. 7274, Dec 2009, pp. 773–777.

[21] Haji-Akbari, A., Engel, M., and Glotzer, S. C., "Phase diagram of hard tetrahedra," *The Journal of Chemical Physics*, Vol. 135, No. 19, 2011, pp. 194101.

[22] van Anders, G., Ahmed, N. K., Smith, R., Engel, M., and Glotzer, S. C., "Entropically Patchy Particles: Engineering Valence through Shape Entropy," *ACS Nano*, Vol. 8, No. 1, jan 2014, pp. 931–940.

[23] van Anders, G., Klotsa, D., Ahmed, N. K., Engel, M., and Glotzer, S. C., "Understanding shape entropy through local dense packing," *Proceedings of the National Academy of Sciences*, Vol. 111, No. 45, nov 2014, pp. E4812–E4821.

[24] Agarwal, U. and Escobedo, F. A., "Mesophase behaviour of polyhedral particles," *Nature Materials*, Vol. 10, No. 3, Feb 2011, pp. 230–235.

[25] Zhang, J., Luo, Z., Martens, B., Quan, Z., Kumbhar, A., Porter, N., Wang, Y., Smilgies, D.-M., and Fang, J., "Reversible Kirkwood–Alder Transition Observed in Pt 3 Cu 2 Nanoctahedron Assemblies under Controlled Solvent Annealing/Drying Conditions," *Journal of the American Chemical Society*, Vol. 134, No. 34, Aug 2012, pp. 14043–14049.

[26] Auer, S. and Frenkel, D., "Prediction of absolute crystal-nucleation rate in hard-sphere colloids," *Nature*, Vol. 409, No. 6823, Feb 2001, pp. 1020–1023.

[27] Auer, S. and Frenkel, D., "Numerical prediction of absolute crystallization rates in hard-sphere colloids," *The Journal of Chemical Physics*, Vol. 120, No. 6, 2004, pp. 3015.

[28] Auer, S. and Frenkel, D., "Numerical Simulation of Crystal Nucleation in Colloids," *Advanced Computer Simulation*, Springer Science Business Media, Jan 2005, pp. 149–208.

[29] Royall, C. P., Poon, W. C. K., and Weeks, E. R., "In search of colloidal hard spheres," *Soft Matter*, Vol. 9, No. 1, 2013, pp. 17–27.

[30] Agarwal, U. and Escobedo, F. A., "Effect of quenched size polydispersity on the ordering transitions of hard polyhedral particles," *The Journal of Chemical Physics*, Vol. 137, No. 2, 2012, pp. 024905.

[31] Thapar, V. and Escobedo, F. A., "Localized Orientational Order Chaperones the Nucleation of Rotator Phases in Hard Polyhedral Particles," *Physical Review Letters*, Vol. 112, No. 4, Jan 2014.

[32] Gilbert, E. G., Johnson, D. W., and Keerthi, S. S., "A fast procedure for computing the distance between complex objects in three-dimensional space," *IEEE Journal of Robotics and Automation*, Vol. 4, No. 2, 1988, pp. 193–203.

[33] Anderson, J. A., Irrgang, M. E., and Glotzer, S. C., "Scalable Metropolis Monte Carlo for simulation of hard shapes," *accepted for publication in Computer Physics Communications*, 2016.

[34] Frenkel, D. and Smit, B., *Monte Carlo Simulations in Various Ensembles*, Elsevier BV, 2002.

[35] Sethna, J., *Statistical Mechanics: Entropy, Order Parameters, and Complexity*, Vol. 14, Oxford University Press, 2006.

[36] Khadilkar, M. R. and Escobedo, F. A., "Self-assembly of binary space-tessellating compounds," *The Journal of Chemical Physics*, Vol. 137, No. 19, 2012, pp. 194907.

[37] Manousiouthakis, V. I. and Deem, M. W., "Strict detailed balance is unnecessary in Monte Carlo simulation," *The Journal of Chemical Physics*, Vol. 110, No. 6, 1999, pp. 2753.

[38] Anderson, J. A., Lorenz, C. D., and Travesset, A., "General purpose molecular dynamics simulations fully implemented on graphics processing units," *Journal of Computational Physics*, Vol. 227, 2008, pp. 5342–5359.

[39] Mickel, W., Kapfer, S. C., Schroder-Turk, G. E., and Mecke, K., "Shortcomings of the bond orientational order parameters for the analysis of disordered particulate matter," *The Journal of Chemical Physics*, Vol. 138, No. 4, 2013, pp. 044501.

[40] Engel, M., Anderson, J. A., Glotzer, S. C., Isobe, M., Bernard, E. P., and Krauth, W., "Hard-disk equation of state: First-order liquid-hexatic transition in two dimensions with three simulation methods," *Physical Review E*, Vol. 87, No. 4, Apr 2013.

[41] Steinhardt, P. J., Nelson, D. R., and Ronchetti, M., "Bond-orientational order in liquids and glasses," *Physical Review B*, Vol. 28, No. 2, 1983, pp. 784.

[42] Harper, E. S., Anderson, J. A., Spellings, M., Irrgang, M. E., Newman, R., Du, X., and Glotzer, S. C., "Freud: Simulation Analysis Software Suite," *in preparation*, 2016.

[43] ten Wolde, P.-R., Ruiz-Montero, M. J., and Frenkel, D., "Simulation of homogeneous crystal nucleation close to coexistence," *Faraday Discussions*, Vol. 104, 1996, pp. 93.

[44] Filion, L., Hermes, M., Ni, R., and Dijkstra, M., "Crystal nucleation of hard spheres using molecular dynamics, umbrella sampling, and forward flux sampling: A comparison of simulation techniques," *The Journal of Chemical Physics*, Vol. 133, No. 24, 2010, pp. 244115.

[45] Ni, R., Smallenburg, F., Filion, L., and Dijkstra, M., "Crystal nucleation in binary hard-sphere mixtures: the effect of order parameter on the cluster composition," *Molecular Physics*, Vol. 109, No. 7-10, apr 2011, pp. 1213–1227.

[46] Engel, M., Damasceno, P. F., Phillips, C. L., and Glotzer, S. C., "Computational self-assembly of a one-component icosahedral quasicrystal," *Nature Materials*, Vol. 14, No. 1, Dec 2014, pp. 109–116.

[47] Torrie, G. and Valleau, J., "Nonphysical sampling distributions in Monte Carlo free-energy estimation: Umbrella sampling," *Journal of Computational Physics*, Vol. 23, No. 2, Feb 1977, pp. 187–199.

[48] Grossfield, A., "WHAM: the weighted histogram analysis method," version 2.0.9, http://membrane.urmc.rochester.edu/content/wham, 2013.

[49] Thapar, V. and Escobedo, F. A., "Extensions of the interfacial pinning method and application to hard core systems," *The Journal of Chemical Physics*, Vol. 141, No. 12, Sep 2014, pp. 124117.

[50] Pedersen, U. R., Hummel, F., Kresse, G., Kahl, G., and Dellago, C., "Computing Gibbs free energy differences by interface pinning," *Physical Review B*, Vol. 88, No. 9, Sep 2013.

[51] Ye, X., Collins, J. E., Newman, R. S., Engel, M., Chen, J., Xing, G., Kagon, C. R., Glotzer, S. C., and Murray, C. B., "Size and Shape-Controlled Synthesis of Doped $LiYF_4$ Upconversion Nanophosphors and their Shape Directed Self-Assembly," *In preparation*, 2016.

[52] Gong, J., Newman, R. S., Engel, M., Glotzer, S. C., and Tang, Z., "Shape-Dependent Ordering of Gold Nanocrystals into Large-Scale Superlattices," *submitted Nature Communications*, 2016.

[53] Niu, W., Zheng, S., Wang, D., Liu, X., Li, H., Han, S., Chen, J., Tang, Z., and Xu, G., "Selective Synthesis of Single-Crystalline Rhombic Dodecahedral, Octahedral, and Cubic Gold Nanocrystals," *Journal of the American Chemical Society*, Vol. 131, No. 2, Jan 2009, pp. 697–703.

[54] Li, R., Bian, K., Wang, Y., Xu, H., Hollingsworth, J. A., Hanrath, T., Fang, J., and Wang, Z., "An Obtuse Rhombohedral Superlattice Assembled by Pt Nanocubes," *Nano Letters*, Vol. 15, No. 9, Sep 2015, pp. 6254–6260.

[55] Young, K. L., Personick, M. L., Engel, M., Damasceno, P. F., Barnaby, S. N., Bleher, R., Li, T., Glotzer, S. C., Lee, B., and Mirkin, C. A., "A Directional Entropic Force Approach to Assemble Anisotropic Nanoparticles into Superlattices," *Angewandte Chemie International Edition*, Vol. 52, No. 52, Nov 2013, pp. 13980–13984.

[56] Smilgies, D.-M., "Scherrer grain-size analysis adapted to grazing-incidence scattering with area detectors," *Journal of Applied Crystallography*, Vol. 42, No. 6, Oct 2009, pp. 1030–1034.

[57] Torquato, S. and Jiao, Y., "Dense packings of the Platonic and Archimedean solids," *Nature*, Vol. 460, No. 7257, Aug 2009, pp. 876–879.

[58] Gantapara, A. P., de Graaf, J., van Roij, R., and Dijkstra, M., "Phase Diagram and Structural Diversity of a Family of Truncated Cubes: Degenerate Close-Packed Structures and Vacancy-Rich States," *Physical Review Letters*, Vol. 111, No. 1, Jul 2013.

[59] Smallenburg, F., Filion, L., Marechal, M., and Dijkstra, M., "Vacancy-stabilized crystalline order in hard cubes," *Proceedings of the National Academy of Sciences*, Vol. 109, No. 44, Sep 2012, pp. 17886–17890.

[60] Bishop, K. J. M., Wilmer, C. E., Soh, S., and Grzybowski, B. A., "Nanoscale Forces and Their Uses in Self-Assembly," *Small*, Vol. 5, No. 14, Jul 2009, pp. 1600–1630.

[61] Damasceno, P. F., Engel, M., and Glotzer, S. C., "Crystalline Assemblies and Densest Packings of a Family of Truncated Tetrahedra and the Role of Directional Entropic Forces," *ACS Nano*, Vol. 6, No. 1, Jan 2012, pp. 609–614.

[62] Marechal, M. and Löwen, H., "Density Functional Theory for Hard Polyhedra," *Physical Review Letters*, Vol. 110, No. 13, Mar 2013.

[63] Frenkel, D. and Ladd, A. J. C., "New Monte Carlo method to compute the free energy of arbitrary solids. Application to the fcc and hcp phases of hard spheres," *The Journal of Chemical Physics*, Vol. 81, No. 7, 1984, pp. 3188.

[64] Ni, R., Gantapara, A. P., de Graaf, J., van Roij, R., and Dijkstra, M., "Phase diagram of colloidal hard superballs: from cubes via spheres to octahedra," *Soft Matter*, Vol. 8, No. 34, 2012, pp. 8826.

[65] Nola, S., Newman, R. S., Dshemuchadse, J., and Glotzer, S. C., "Nucleation of Hard Rhombic Dodecahedra *vs.* Spheres," *in preparation*, 2016.

[66] Anderson, J. A., Jankowski, E., Grubb, T. L., Engel, M., and Glotzer, S. C., "Massively parallel Monte Carlo for many-particle simulations on GPUs," *Journal of Computational Physics*, Vol. 254, dec 2013, pp. 27–38.

[67] Kawasaki, T. and Tanaka, H., "Formation of a crystal nucleus from liquid," *Proceedings of the National Academy of Sciences*, Vol. 107, No. 32, 2010, pp. 14036–14041.

[68] Hales, T. C., "A proof of the Kepler conjecture," *Annals of Mathematics*, Vol. 162, 2005, pp. 1065–1185.

[69] Hales, T. C. and Ferguson, S. P., *The Kepler Conjecture: The Hales-Ferguson Proof*, Springer-Verlag New York, 2011.

[70] van Anders, G., Klotsa, D., Karas, A. S., Dodd, P. M., and Glotzer, S. C., "Digital Alchemy for Materials Design: Colloids and Beyond," *ACS Nano*, Vol. 9, No. 10, 2015, pp. 9542–9553.

[71] Newman, R. S., Dshemuchadse, J., and Glotzer, S. C., "Nucleation Free Energies of FCC-assembling Polyhedra," *in preparation*, 2016.

[72] Nola, S., Dshemuchadse, J., and Glotzer, S. C., "Metastable fluids of sphere-like hard polyhedra," *in preparation*, 2016.

[73] Chen, E. R., Klotsa, D., Engel, M., Damasceno, P. F., and Glotzer, S. C., "Complexity in Surfaces of Densest Packings for Families of Polyhedra," *Physical Review X*, Vol. 011024, 2014, pp. 1–23.

[74] Spellings, M., Marson, R., Anderson, J. A., and Glotzer, S. C., "GPU accelerated Discrete Element Method (DEM) Molecular Dynamics," *In preparation*, 2016.

[75] Sigurgeirsson, H. and Heyes, D. M., "Transport coefficients of hard sphere fluids," *Molecular Physics*, Vol. 101, No. 3, Feb 2003, pp. 469–482.